

**Numerische Simulation von Strömung und  
Massentransport in (elektro-)  
chromatographischen Systemen**

**DISSERTATION**

zur Erlangung des akademischen Grades

**Doktoringenieur**

**(Dr.-Ing.)**

von Dipl.- Phys. Dzmitry Hlushkou

geb. am 14. Dezember 1969 in Minsk, Weißrussland

genehmigt durch die Fakultät für Verfahrens- und Systemtechnik  
der Otto-von-Guericke-Universität Magdeburg

Gutachter: Jun.-Prof. Dr. U. Tallarek  
Prof. Dr. V. Apanasovich  
Prof. Dr. D. Thévenin

Promotionkolloquium am 23. April 2004

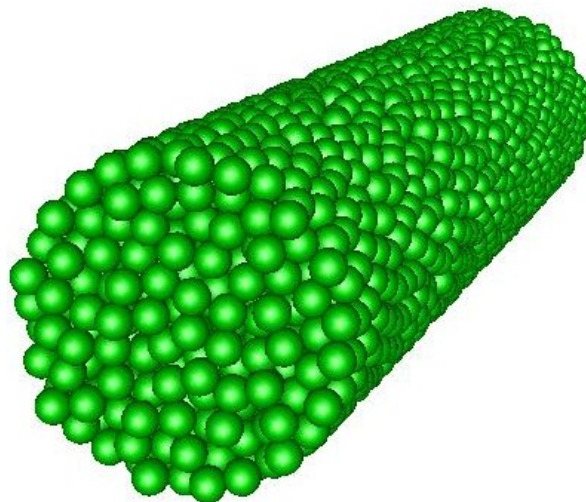




Belarusian State University

Ph.D. Thesis

# Numerical simulation of fluid flow and mass transport in (electro) chromatographic systems



Dzmitry Hlushkou

Magdeburg, 2004



# Acknowledgements

First of all, I would like to thank the Max-Planck-Society for the given opportunity and support to work for and prepare this thesis.

I gratefully thank my supervisor, Ulrich Tallarek, for his suggestions, proof reading and support during my time in The Netherlands and Germany. Not often in life it is possible to meet a person with such an harmonious combination of scientific capability and human qualities.

I would also like to thank my co-supervisors Andreas Seidel-Morgenstern, who was always very kind and open for help to me, and Vladimir Apanasovich for numerous useful discussions, support and assistance; Drona Kandhai for his help and for allowing me to reproduce some of his results; and Ivan Mihov and Nadezhda Sotskova for their help and encouragement.



*Моим родителям, моей жене Марине и моей дочери Юлии...*

*To my parents, my wife Maryna, and my daughter Julia...*





# TABLE OF CONTENTS

<b>Notation</b> .....	i
<b>1. Introduction</b> .....	1
<b>2. Theoretical Backgrounds of Mass Transport Phenomena in Polar Liquid Systems</b> .....	9
2.1. Fluid dynamics .....	9
2.2. Mass transfer .....	13
2.3. Electric double layer.....	15
2.4. Electroosmosis and mass transport.....	19
2.5. References .....	22
<b>3. Numerical Methods</b> .....	23
3.1. General simulation approach.....	23
3.2. Lattice-Boltzmann hydrodynamics .....	25
3.3. References .....	37
<b>4. Numerical Simulation of Mass Transport in Microfluidic Systems</b> .....	39
4.1. Coupled lattice Boltzmann and finite difference simulation of electroosmosis in microfluidic channels .....	40
4.2. Numerical simulation of electroosmotic flow in heterogeneous slit microchannels with non-equilibrium electrical double layer .....	69
4.3. Numerical simulation of electrokinetic microfluidics in colloidal systems .....	93
4.4. Numerical simulation of mass transport in porous media .....	105
4.5. References .....	141

<b>5. Summary and conclusion</b> .....	147
<b>6. Resume</b> .....	151
<b>7. Zusammenfassung</b> .....	153
<b>8. Lebenslauf</b> .....	157

# Notation

## Latin symbols

$A$	(free) cross-sectional area of channel (column)
$A_{\text{intra}}$	amount of stagnant fluid molecules in intraparticle pore space
$\mathbf{a}$	acceleration of a substance/body/particle
$B_{\text{intra}}$	mass transfer rate constant
$C$	constant
$C_L$	longitudinal velocity autocovariance
$c$	molar concentration
$c$	speed of light
$c_s$	speed of sound
$c_\infty$	molar concentration in electroneutral solution
$D$	diameter of particle in lattice units
$D$	diffusion coefficient
$D_{\text{intra}}$	intraparticle diffusion coefficient
$D_L$	longitudinal dispersion
$D_L^*$	asymptotic longitudinal dispersion
$D_m$	free molecular diffusion coefficient
$d_c$	capillary/column diameter
$d_p$	particle diameter
$d_{\text{pore}}$	pore diameter
$\mathbf{E}$	local electric field
$E$	complex signal in PFG-NMR experiment
$\mathbf{E}_{\text{ext}}$	external applied electric field
$\mathbf{e}_\alpha$	normalized discrete particle velocity
$F$	Faraday's constant
$\mathbf{F}$	acting force
$F_\alpha$	discrete acting force

<b>f</b>	volume density of acting force (body force)
$\mathcal{F}$	particle distribution function
$\mathcal{F}_\alpha$	discrete particle distribution function
$\mathcal{F}^{\text{eq}}$	equilibrium (Maxwell-Boltzmann) particle distribution function
$\mathcal{F}^{\text{neq}}$	non-equilibrium particle distribution function
<b>G</b>	free (or potential) energy
<b>g</b>	acceleration of gravity
<b>g</b>	amplitude of pulsed magnetic field
<i>g</i>	pair-correlation function
$I_0$	zero-order modified Bessel function
$I_1$	first-order modified Bessel function
<b>i<sub>el</sub></b>	electric current density
$[\text{H}^+]_0$	surface activity of protons
<b>H</b>	height of packing
<i>h</i>	size of computational cubic cell
<b>j</b>	flux density
<b>j<sub>C</sub></b>	convective flux density
<b>j<sub>D</sub></b>	diffusive flux density
<b>j<sub>M</sub></b>	migration flux density
<b>K</b>	hydraulic permeability
<i>k</i>	dimensionless hydraulic permeability
$K_w$	dissociation constant of water
$k_B$	Boltzmann constant
$M_m$	molecular mass
<i>m</i>	mass of a substance/body/particle
<b>N</b>	total number of ions/particles
$N_{\text{inter}}$	number of particles in interparticle space
$N_{\text{intra}}$	number of particles in intraparticle space
$N_{\text{pl}}$	number of theoretical plates
<i>n</i>	number concentration
$\hat{n}$	updated number concentration at current iteration

$\tilde{n}$	number concentration from previous iteration
$n_{\text{inter}}$	number concentration of particles in interparticle space
$n_{\text{intra}}$	number concentration of particles in intraparticle space
$n_{\infty}$	number concentration in electroneutral solution
$P_{\text{av}}$	average propagator
$\mathbf{p}$	momentum per unit volume
$p$	hydrostatic pressure
$Pe$	Peclet number
$\text{pK}$	logarithmic dissociation constant
$p_{\text{enter}}$	entrance probability
$p_{\text{exit}}$	exit probability
$Q$	volumetric flow rate
$\mathbf{q}$	wavevector
$q_e$	elementary charge
$\mathbf{R}$	dynamic (net) displacement
$R$	gas constant
$\mathbf{r}$	position vector
$r_c$	capillary radius
$r_s$	sphere diameter
$Re$	Reynolds number
$S$	area of plate
$S$	echo amplitude in PFG-NMR experiment
$T$	absolute temperature
$t$	time
$t_b$	characteristic time for boundary-layer dispersion
$t_h$	characteristic time for intraparticle holdup
$t_r$	retention time
$\mathbf{u}$	particle velocity
$\mathbf{u}_{\alpha}$	discrete particle velocity
$V$	volume
$V_{\text{sph}}$	volume occupied by spheres
$V_v$	void volume

$\langle  v_x  \rangle$	root-mean-square axial velocity
$\langle  v_y  \rangle$	root-mean-square transversal velocity
$\langle  v  \rangle$	root-mean-square absolute velocity
$\mathbf{v}$	fluid velocity
$\mathbf{v}^*$	modified equilibrium velocity
$\mathbf{v}'$	modified equilibrium velocity
$W_\alpha$	weight coefficient
$w_\alpha$	normalized weight coefficient
$z$	distance between plates
$z$	valency

## Greek symbols

$\alpha$	aspect ratio
$\beta$	computational grid resolution
$\Gamma_{\text{SiOH}}$	surface density of silanol groups
$\Gamma_{\text{SiO}^-}$	surface density of dissociated silanol groups
$\Gamma_{\text{tot}}$	surface density of chargeable silanol groups
$\gamma$	global relative error/difference
$\gamma_{\text{PNP}}$	convergence rate of numerical solution for coupled Poisson and Nernst-Planck equations
$\gamma_{\text{NS}}$	convergence rate of numerical solution for Navier-Stokes equation
$\Delta$	time interval
$\delta$	relative difference field
$\delta_{ij}$	Kronecker delta
$\delta \mathbf{r}^D$	displacement due to molecular diffusion
$\delta_t$	time step
$\delta_x$	lattice constant
$\varepsilon$	porosity
$\varepsilon_{\text{inter}}$	porosity of interparticle pore space
$\varepsilon_0$	permittivity of the vacuum

$\varepsilon_r$	relative permittivity
$\varepsilon_T$	total porosity
$\zeta$	zeta-potential
$\tilde{\zeta}_m$	Fourier transform of zeta-potential
$\eta$	dynamic viscosity
$\Theta$	physical quantity
$\Theta_b$	boundary layer mass transfer
$\Theta_h$	intraparticle holdup
$\Theta_m$	mechanical dispersion
$\theta$	azimuthal coordinate
$\kappa$	bulk viscosity
$\kappa$	reciprocal of electrical double layer thickness
$\lambda_D$	Debye screening length
$\mu_{eo}$	electroosmotic mobility
$\bar{\nu}$	outer normal
$\nu$	kinematic viscosity
$\Xi(\mathbf{u})$	polinom of $\mathbf{u}$
$\xi$	unit vector
$\xi$	effective potential
$\rho$	radial coordinate
$\rho$	mass density
$\rho_f$	fluid density
$\rho_q$	electrical charge density
$\sigma^*$	conductivity of packed column saturated by electrolyte
$\sigma^\infty$	conductivity of equilibrium electrolyte beyond EDL
$\sigma$	differential cross section of binary collision
$\sigma$	electrical surface charge density
$\sigma$	width at half-height of chromatographic peak
$\sigma$	variance
$\tau$	stress tensor

$\tau$	relaxation time
$\tau$	dimensionless relaxation time
$\tau_{ij}$	stress tensor
$\mathbf{v}$	modified fluid velocity
$\Upsilon$	tortuosity
$\Phi$	local electrical potential
$\hat{\Phi}$	updated local electrical potential at current iteration
$\check{\Phi}$	local electrical potential from previous iteration
$\phi$	electrical potential due to applied electric field
$\psi$	electrical potential due to surface charge
$\psi_d$	column-to-particle diameter (aspect) ratio
$\psi_{\text{OHP}}$	electrical potential at outer Helmholtz plane due to surface charge
$\psi_S$	electrical potential at Stern plane due to surface charge
$\chi$	perturbation parameter
$\Omega$	surface of the solid-liquid interface
$\Omega_c$	scattering direction of binary collision
$\Omega_c$	collision operator
$\omega$	relaxation parameter of SOR scheme



## Chapter 1

# Introduction

In his “Science of Logic” (“Wissenschaft der Logik”) Georg Wilhelm Friedrich Hegel (1770-1831) remarked: “It is said that there are no sudden changes in nature, and it is the common view that when we speak of a growth or a destruction, we always imagine a gradual growth or disappearance. Yet we have seen cases in which the alteration of existence involves not only a transition from one proportion to another, but also a transition, by a sudden leap, into a qualitatively different thing; an interruption of a gradual process, differing qualitatively from the preceding, the former state.” Nature allows to observe this “transition from quantitative changes to qualitative changes” at any moment and in any place. For example, the temperature of water has at first no effect on its liquid state; but as the temperature of liquid water rises or falls, a moment arrives when this state of cohesion changes and the water is converted in one case into steam and in the other into ice. Take oxygen: if the molecule contains three atoms instead of the customary two, we get ozone, a body definitely distinct in odour and reaction from ordinary oxygen. A similar picture is observed in science and engineering. For instance, the gradual growth of speed in aviation resulted in the appearance of a jet aircraft, while miniaturization in electronics provoked the transition from vacuum tubes to semi-conductor devices and microchips.

One of the branches of analytical chemistry, chromatography, also did not avoid such “evolutional sudden changes”. Striving for further increase of the analysis efficiency scientists, engineers, and technicians are stimulated to develop methodology, employ new materials, equipment as well as new techniques. A miniaturization in high performance liquid chromatography (HPLC) concerning the column inner diameter (i.d.) and associated volumetric flow rates has been initiated more than 25 years ago, and it is an ongoing development mainly because of the need for handling small amount of complex sample. While the typical dimensions in analytical and narrow-bore HPLC include a 2.1-4.6 mm column i.d., bed lengths of less than 200 mm and random sphere packings of 5-15  $\mu\text{m}$  average diameter particles, the further miniaturization towards nano-LC can offer distinct advantages [1-6] including the

- reduced consumption of stationary phase, solvent and chemicals, facilitating a use of expensive stationary phase, exotic mobile phases and minute samples in the environmental and biomedical sciences,
- increased mass sensitivity due to a reduced chromatographic dilution,
- use of smaller, but still porous particles ( $d_p = 3-5 \mu\text{m}$ ) leading to higher column efficiencies by a significantly reduced contribution of the intraparticle stagnant zone to hydrodynamic dispersion,
- compatibility with flow rate requirements of a nano-ESI interface in view of an on-line coupling to mass spectrometry, and
- application of high electrical fields for the additional (or exclusive) transport of bulk liquid and solute molecules through a porous medium by electroosmosis and/or electrophoresis.

Related to the last aspect, in general, mass transport in porous media induced by an externally applied electrical field nowadays plays a central role in a number of analytical, technological and environmental processes, including the dewatering of waste sludge and soil remediation, capillary electrophoresis or electrochromatographic separations in capillaries and microfluidic devices [7-23]. Still however, there exists a lack of mechanistic understanding concerning an interrelation between external control variables like the electrical field strength or current and parameters controlling macroscopic electrokinetic transport like the dispersion coefficient or effective mobility. It is intimately related to the physico-chemical nature of the surface and its dynamic behaviour, pore space morphology, and properties of the liquid. The characterization of these parameters is of a fundamental relevance as it critically guides the performance and compelling advantages, as well as design strategies of a particular electrokinetic process with respect to any alternative diffusive-convective transport schemes.

In the present work we are mainly concerned with the dynamics of electroosmotic flow (EOF) and solute transport in capillary electrochromatography (CEC). While the column efficiencies in HPLC may be increased by a reduction of the particle size this option is limited via the maximum operating pressure with conventional instrumentation. A significantly improved performance in view of the dispersion and permeability can be achieved in CEC by utilizing EOF for transport of bulk mobile phase. In this introduction we give a brief survey of some of the most important features of the EOF in porous media (like random sphere packings) because it may be a relatively unfamiliar topic to many readers.

CEC is a separation technique carried out most commonly in a capillary column packed with conventional HPLC adsorbent material by utilizing an electroosmotically driven mobile phase at high electrical field strength (50-100 kV/m) in an apparatus similar to that used in capillary zone electrophoresis (CZE). Consequently, CEC combines the variety of retention mechanisms and stationary phase selectivities popular in HPLC with miniaturization potential of CZE. Electrochromatography can be described as an electrophoretic analysis where sorptive interactions with the stationary (retentive) phase of the support material are a major contribution, i.e., the separation is achieved by differential partitioning and migration.

In general, the history of electrokinetic effects could be traced back almost 200 years when Reuss in 1809 described in the *Proceedings of the Imperial Society of Naturalists of Moscow* his experiments concerning water migration through porous clay under the influence of an applied electric field. One of the most influential contributions to the theoretical description of electrokinetic transport was the development of the electric double layer (EDL) theory by Helmholtz in 1879. An electrical double layer exists at most solid-polar liquid interfaces. When solid is in contact with a liquid medium, a solid surface may be charged due to various mechanisms and surrounded by the ions of opposite sign (counterions) from the liquid phase. The region reached by counterions is referred to as the EDL. Its thickness depends on the temperature, electrolyte concentration, and valence number of ions, but normally it is of the order 10 nm. Upon application of an axial external electric field the uncompensated charges in the EDL give rise to volume forces, and due to a viscous drag the resulting EOF is spread beyond of the solid-liquid interface. Although the origin of CEC traces back to 1974 when Pretorius et al. [24] have reported the successful electrokinetic transport of eluent through a (comparatively large) chromatographic column, it has been Jorgenson and Lukacs [25] who demonstrated the feasibility of CEC for a separation of neutral compounds by applying a potential gradient across a packed column of capillary dimension, before Knox and Grant [26-28] examined more fundamental aspects and the advantages of CEC.

CEC is commonly performed in a 50-150  $\mu\text{m}$  i.d. (fused-silica) capillary column setup which is usually composed of a packed bed and open tubular segment, as well as a detection window immediately behind the outlet frit of the fixed bed. Compared to pressure-driven flow a superior performance of EOF through a single, straight and open capillary originates from the fact that in the limit of a thin electrical double layer (EDL) the velocity apparently slips at the inner wall of the capillary and, thus, the fluid moves as in plug-flow (assuming isothermal conditions) [29-32]. Further, for fixed pressure and potential gradients, the ratio of volumetric

EOF to hydraulic flow rates is inversely proportional to the square of the capillary radius [33]. The flat "pore-level" velocity profile of EOF observed for a single-pore geometry (as in CZE) [34, 35] and permeability criterion also have important implications for the fluid dynamics (an improved dispersion behaviour, in particular) in CEC where many pores are connected, as in a random particulate fixed bed, including:

- a use of micron- and submicron-sized particles as packing material [36, 37] for reduction of band spreading toward the diffusion-limited regime,
- the operation of relatively long packed columns (if needed) or, vice versa, use of very short chromatographic beds [38],
- further reduction of the column diameter toward chip format [39-43],
- the generation of a substantial EOF within the porous particles (electroosmotic perfusion) which reduces intraparticle mass transfer resistance and associated holdup dispersion [44-49],
- a higher separation efficiency based on the superior hydrodynamic dispersion characteristics in the interstitial pore space of a sphere packing over a wide range of experimental conditions [50], and
- the enhancement of intraparticle transport of charged species by migration and surface (electro)diffusion [51, 52].

Thus, CEC offers the potential for an implementation into miniaturized systems allowing high sample throughput and resolution, speed and sensitivity. Compared to liquid chromatography CEC offers a better permeability and efficiency, as well as selectivity (in the case of charged analytes), and concerning CZE it operates in systems with far higher surface-to-volume ratio in view of sample capacity and dynamic changes in surface properties. As in capillary HPLC the actual flow rates are inherently compatible with direct mass spectrometric detection.

However, the development of a new technique assumes not only application of new hardware and materials. Frequently, its theoretical description requires also new methods for the solution of applied problems. As mentioned above the EOF arises due to the electrostatic interaction of charges in the EDL with an applied electric field. Whence, volume electrostatic forces determining the flow velocity field depend on the distribution of the electrical charge in a liquid. This distribution is affected, in turn, by convective transport of ions with the fluid flow as well as by diffusion related to the gradient in ion densities. In addition, charge carriers

can be driven by the gradient in the local electrical potential, which is defined, in turn, both by the external electric field and the actual charge distribution in the liquid. Additional various effects can arise due to Joule heating, temperature gradients, modifications of physico-chemical properties of the solid-liquid interface during the separation process, strong electric fields, etc. Finally, one should take into account that all aforementioned phenomena occur in porous media with extremely complicated morphology (e.g., monoliths, membranes, sphere packings), which defines boundary conditions in the corresponding mathematical description. It is obvious that this problem cannot be generally resolved by *analytical* methods.

The objective of this Ph.D. thesis is to study how the electric fields couple with the hydrodynamics and mass transport using *numerical* methods. Through recent developments in computer hardware it is possible to carry out high-performance numerical simulations of hydraulic flows. In this thesis we focus on the expansion of traditional computational fluid dynamics (CFD) to mass transport in microfluidic electrokinetic systems and its application to computer simulations of the various problems, which can originate in electrochromatographic separations.

## References

1. Cs. Horváth, B. A. Preiss, and S. R. Lipsky, *Anal. Chem.* **39**, 1422 (1967).
2. Cs. Horváth and S. R. Lipsky, *Anal. Chem.* **41**, 1227 (1969).
3. R. P. W. Scott and P. Kucera, *J. Chromatogr.* **125**, 251 (1976).
4. D. Ishii, K. Asai, K. Hibi, T. Jonokuchi, and M. Nagaya, *J. Chromatogr.* **144**, 157 (1977).
5. D. Ishii (Ed.), *Introduction to Microscale High-Performance Liquid Chromatography*, VCH, Weinheim, 1988.
6. J. P. C. Vissers, H. A. Claessens, and C. A. Cramers, *J. Chromatogr. A* **779**, 1 (1997).
7. J. P. C. Vissers, *J. Chromatogr. A* **856**, 117 (1999).
8. J. Abian, A. J. Oosterkamp, and E. Gelpi, *J. Mass Spectrom.* **34**, 244 (1999).
9. G. P. Rozing, M. Serwe, H.-G. Weissgerber, and B. Glatz, *Am. Lab.* **33**, 26 (2001).
10. M. Szumski and B. Buszewski, *Crit. Rev. Anal. Chem.* **32**, 1 (2002).
11. E. Rapp and U. Tallarek, *J. Sep. Sci.* **26**, 453 (2003).
12. R. F. Probstein and R. E. Hicks, *Science* **260**, 498 (1993).
13. J. E. Sauer and E. J. Davis, *Environ. Sci. Technol.* **28**, 737 (1994).
14. M. M. Dittmann, K. Wienand, F. Bek, and G. P. Rozing, *LCoGC* **13**, 800 (1995).
15. S. V. Ho, P. W. Sheridan, C. J. Athmer, M. A. Heitkamp, J. M. Brackin, D. Weber, and P. H. Brodsky, *Environ. Sci. Technol.* **29**, 2528 (1995).
16. T. Tsuda (Ed.), *Electric Field Applications in Chromatography, Industrial and Chemical Processes*. Wiley-VCH, Weinheim, 1995.
17. Y. B. Acar, E. E. Ozsu, A. N. Alshawabkeh, M. F. Rabbi, and R. J. Gale, *CHEMTECH* **26**, 40 (1996).
18. A. L. Crego, A. González, and M. L. Marina, *Crit. Rev. Anal. Chem.* **26**, 261 (1996).
19. T. F. Coletta, C. J. Brunell, D. K. Ryan, and H. I. Inyang, *J. Environ. Eng.* **123**, 1227 (1997).
20. C. Fujimoto, *Trends Anal. Chem.* **18**, 291 (1999).
21. L. A. Colón, G. Burgos, T. D. Maloney, J. M. Cintrón, and R. L. Rodríguez, *Electrophoresis* **21**, 3965 (2000).
22. U. Pyell, *J. Chromatogr. A* **892**, 257 (2000).
23. Q. L. Tang and M. L. Lee, *Trends Anal. Chem.* **19**, 648 (2000).
24. V. Pretorius, B.J. Hopkins, and J.D. Schieke, *J. Chromatogr.* **99**, 23 (1974).
25. J. W. Jorgenson and K. D. Lukacs, *J. Chromatogr.* **218**, 209 (1981).
26. J. H. Knox and I. H. Grant, *Chromatographia* **24**, 135 (1987).
27. J. H. Knox, *Chromatographia* **26**, 329 (1988).
28. J. H. Knox and I. H. Grant, *Chromatographia* **32**, 317 (1991).
29. C. L. Rice, R. Whitehead, *J. Phys. Chem.* **69**, 4017 (1965).
30. R. J. Gross, J. F. Osterle, *J. Chem. Phys.* **48**, 228 (1968).
31. K.-L. K. Liu, K. L. Davis, and M. D. Morris, *Anal. Chem.* **66**, 3744 (1994).
32. S. Arulanandam and D. Q. Li, *Colloids Surf. A* **161**, 89 (2000).
33. R. F. Probstein, *Physicochemical Hydrodynamics*, John Wiley & Sons, New York, 1994.
34. P. H. Paul, M. G. Garguilo, and D. J. Rakestraw, *Anal. Chem.* **70**, 2459 (1998).
35. U. Tallarek, E. Rapp, T. Scheenen, E. Bayer, and H. Van As, *Anal. Chem.* **72**, 2292 (2000).

36. K. K. Unger, S. Lüdtke, and M. Grün, *LC-GC Int.* **12**, 870 (1999).
37. K. K. Unger, D. Kumar, M. Grün, D. Büchel, S. Lüdtke, Th. Adam, K. Schumacher, and S. Renker, *J. Chromatogr. A* **892**, 47 (2000).
38. T. Sakaki, S. Kitagawa, and T. Tsuda, *Electrophoresis* **21**, 3088 (2000).
39. J. P. Kutter, S. C. Jacobson, N. Matsubara, and J. M. Ramsey, *Anal. Chem.* **70**, 3291 (1998).
40. C. Ericson, J. Holm, T. Ericson, S. Hjerten, *Anal. Chem.* **72**, 81 (2000).
41. R. D. Oleschuk, L. L. Schultz-Lockyear, Y. B. Ning, and D. J. Harrison, *Anal. Chem.* **72**, 585 (2000).
42. B. E. Slentz, N. A. Penner, E. Lugowska, and F. E. Regnier, *Electrophoresis* **22**, 3763 (2001).
43. D. J. Throckmorton, T. J. Shepodd, and A. K. Singh, *Anal. Chem.* **74**, 784 (2002).
44. R. Stol, W. Th. Kok, and H. Poppe, *J. Chromatogr. A* **853**, 45 (1999).
45. E. Wen, R. Asiaie, and Cs. Horváth, *J. Chromatogr. A* **855**, 349 (1999).
46. P. T. Vallano and V. T. Remcho, *Anal. Chem.* **72**, 4255 (2000).
47. U. Tallarek, E. Rapp, H. Van As, and E. Bayer, *Angew. Chem. Int. Ed.* **40**, 1684 (2001).
48. R. Stol, H. Poppe, and W. Th. Kok, *Anal. Chem.* **73**, 3332 (2001).
49. U. Tallarek, E. Rapp, A. Seidel-Morgenstern, and H. Van As, *J. Phys. Chem. B* **106**, 12709 (2002).
50. J. H. Knox and I. H. Grant, *Chromatographia* **32**, 317(1991).
51. R. Xiang and Cs. Horváth, *Anal. Chem.* **74**, 762 (2002).
52. S. R. Dziennik, E. B. Belcher, G. A. Barker, M. J. DeBergalis, S. E. Fernandez, and A. M. Lenhoff, *Proc. Natl. Acad. Sci. U.S.A.* **100**, 420 (2003).





## Chapter 2

# Theoretical Background of Mass Transport Phenomena in Polar Liquid Systems

In this chapter a brief theoretical account on mass transport in polar fluids is given. In general, classical fluid mass transport phenomena are concerned with two related topics: *fluid dynamics* and *mass transfer*. Fluid dynamics involves the transport of momentum, whilst mass transfer deals with transport of various species. These two types of transport phenomena are usually grouped together due to their similar mathematical framework. In contrast to electrically neutral liquids, polar liquids, in particular electrolyte solutions, can demonstrate a substantially different behaviour when an external electric field is applied. This difference arises from electrostatic interactions between the electric field and charges in the liquid.

### 2.1. Fluid dynamics

#### 2.1.1. Newton's law of viscosity

We begin our consideration with a simple system consisting of two very long parallel plates, each one with area  $S$ , separated by a small distance  $z$  (Fig. 2.1). The space between plates is saturated by a fluid. One plate is set in motion relative to the other in the positive  $x$  direction at constant velocity  $V$ . The force  $F$  needed to pull one plate past the other depends on the size of the plates  $S$ , the distance  $z$ , and their relative velocity  $v$ . This relation can be written as

$$\frac{F}{S} = \eta \frac{v}{z} \quad (2.1)$$

or in a differential form

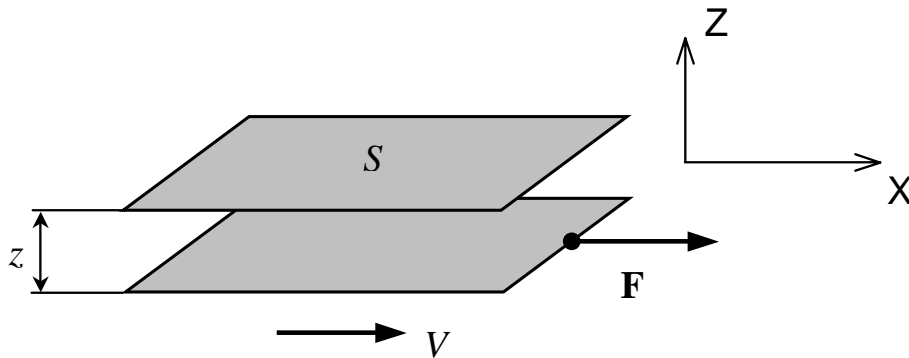


**Figure 2.1.** Shear flow built up between two moving parallel plates.

$$\tau_{zx} = -\eta \frac{dv_x}{dz}, \quad (2.2)$$

where  $\eta$  is the dynamic viscosity of the fluid and  $\tau_{zx}$  is the force in the  $x$  direction per unit area perpendicular to the  $z$  direction (or stress).  $\tau_{zx}$  may be also interpreted as the flux (flow per unit area) of  $x$ -momentum in the positive  $z$  direction. The minus sign in Eq. 2.2 indicates that the momentum flows from higher velocity to the lower velocity. This equation is often called Newton's law of viscosity. The proportionality constant  $\eta$  is defined to be the viscosity and is a fluid property. For many fluids the viscosity is constant, i.e. it is independent of the shear stress and the velocity gradient. Such fluids are referred to as *Newtonian*. Often, another quantity

$$\nu = \frac{\eta}{\rho_f}, \quad (2.3)$$

called kinematic viscosity is used, where  $\rho_f$  is the fluid density.

The general, 3D-form of Newton's law of viscosity is much more complicated. It includes nine relations

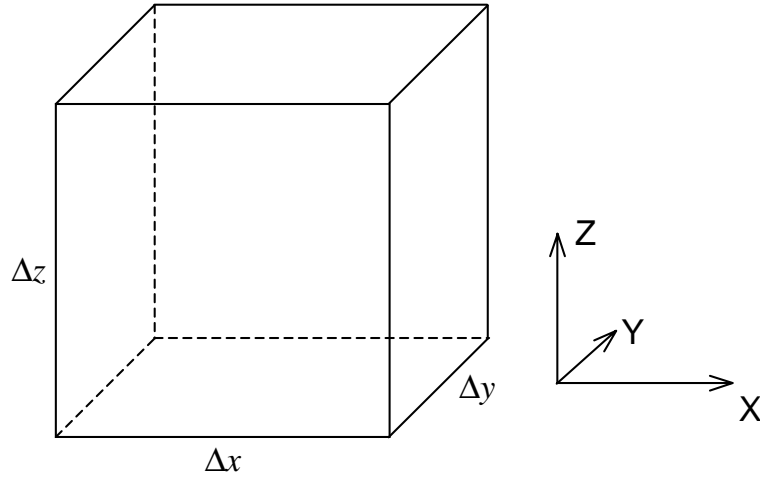


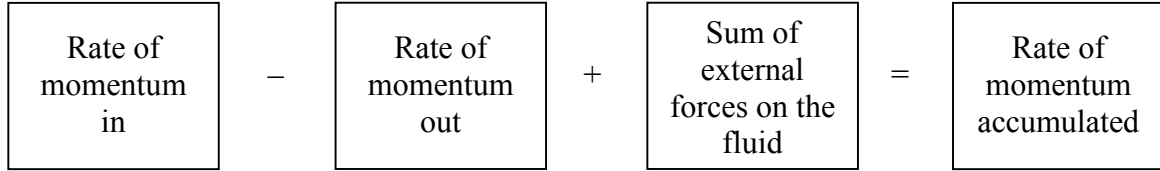
**Figure 2.2.** Elementary volume element  $\Delta x \Delta y \Delta z$ .

$$\tau_{ij} = -\eta \left( \frac{\partial v_j}{\partial x_i} + \frac{\partial v_i}{\partial x_j} \right) + \left( \frac{2}{3} \eta - \kappa \right) \left( \frac{\partial v_x}{\partial x} + \frac{\partial v_y}{\partial y} + \frac{\partial v_z}{\partial z} \right) \delta_{ij}, \quad (2.4)$$

where  $i, j$  may be 1, 2, 3;  $x_1, x_2, x_3$  and  $v_1, v_2, v_3$  denote  $x, y, z$  and  $v_x, v_y, v_z$  respectively,  $\kappa$  is called “bulk” or “dilatational” viscosity, and  $\delta_{ij}$  is the Kronecker delta. The bulk viscosity is a phenomenological coefficient and it is important in the pure expansion or contraction of a fluid and arises in explosions and supersonic vibrational and rotational contributions to the molecule’s overall energy and momentum [1]. Since these contributions are generally much smaller than translational contributions at room temperature and standard pressure, the coefficient of bulk viscosity can be neglected.

### 2.1.2. Equation of motion

To derive the equation of motion we consider the volume element  $\Delta x \Delta y \Delta z$  (Fig. 2.2) and write the momentum balance that is a statement of Newton’s law of motion  $\mathbf{F} = m\mathbf{a}$  and has the form



Note that the equation of motion is a vector equation with three components in each of the coordinate directions. We consider only the  $x$ -component of that equation in detail. Momentum may enter and leave a volume element by convection, i.e. by bulk fluid flow, by molecular transport, i.e. by velocity gradients, and by external forces acting on the fluid such as gravity, pressure, electromagnetic forces, etc. The momentum transport via convection can be written as

$$\begin{aligned}
 & [(\rho_f v_x) v_x(x) - (\rho_f v_x) v_x(x + \Delta x)] \Delta y \Delta z + \\
 & [(\rho_f v_x) v_y(y) - (\rho_f v_x) v_y(y + \Delta y)] \Delta x \Delta z + \\
 & [(\rho_f v_x) v_z(z) - (\rho_f v_x) v_z(z + \Delta z)] \Delta x \Delta y
 \end{aligned} \tag{2.5}$$

Velocity gradients and pressure result in differences in shear and normal stresses across the volume element with the flow of momentum from the higher to the lower stress.

$$\begin{aligned}
 & [\tau_{xx}(x) - \tau_{xx}(x + \Delta x)] \Delta y \Delta z + \\
 & [\tau_{yx}(y) - \tau_{yx}(y + \Delta y)] \Delta x \Delta z + \\
 & [\tau_{zx}(z) - \tau_{zx}(z + \Delta z)] \Delta x \Delta y
 \end{aligned} \tag{2.6}$$

Pressure gradients, gravity, and other external forces give the following contributions, respectively

$$[p_x(x) - p_x(x + \Delta x)] \Delta y \Delta z + \rho_f g_x \Delta x \Delta y \Delta z + F_x . \tag{2.7}$$

The accumulation of momentum within the volume element is a time dependent quantity

$$\Delta x \Delta y \Delta z \frac{\partial}{\partial t} (\rho_f v_x) . \tag{2.8}$$

If we combine Eqs. 2.5-2.8, divide by  $\Delta x \Delta y \Delta z$ , and take the limit as  $\Delta x \Delta y \Delta z$  goes to zero, we obtain the following expression for  $x$ -component of the momentum balance equation:

$$\frac{\partial}{\partial t}(\rho_f v_x) = - \left\{ \frac{\partial}{\partial x} [(\rho_f v_x) v_x] + \frac{\partial}{\partial y} [(\rho_f v_x) v_y] + \frac{\partial}{\partial z} [(\rho_f v_x) v_z] \right\} - \left[ \frac{\partial \tau_{xx}}{\partial x} + \frac{\partial \tau_{yx}}{\partial y} + \frac{\partial \tau_{zx}}{\partial z} \right] - \frac{\partial p}{\partial x} + \rho_f g_x + \frac{F_x}{\Delta x \Delta y \Delta z} \quad (2.9)$$

Similar equations can be developed for  $y$ - and  $z$ -components of momentum balance. Finally, Eq. 2.9 can be written in vector form as:

$$\frac{\partial}{\partial t}(\rho_f \mathbf{v}) = -[\nabla \cdot (\rho_f \mathbf{v}) \mathbf{v}] - \nabla \cdot \boldsymbol{\tau} - \nabla p + \rho_f \mathbf{g} + \frac{\mathbf{F}}{\Delta x \Delta y \Delta z}. \quad (2.10)$$

This form of equation is an exact analogue of Newton's law of motion. The term on the left-hand side is the mass per unit volume multiplied by the acceleration, whilst each term on the right-hand side has the units of (force)/(unit volume). Equation 2.10 and the equation of continuity

$$\frac{\partial \rho_f}{\partial t} + \nabla \cdot (\rho_f \mathbf{v}) = 0 \quad (2.11)$$

are often called *Navier-Stokes* equations.

## 2.2. Mass transfer

From the microscopic point of view any solid, fluid, or gas consists of atoms and molecules being in a constant state of motion. This fluctuating state is driven with kinetic energy and motion results in about no change in mean composition in a homogeneous system. By contrast, in heterogeneous media with a concentration gradient for a chemical species, this motion can give rise to a net movement of a particular species. This net molecular motion is called *diffusion* and it presents one mass transfer mechanism. Another mechanism of mass transfer can be provided by macroscopic motion or flow in fluids or gases and is often referred to as *convection*. Mass transfer can occur due to a number of other mechanisms as well, for example, due to *migration* of ions or charged solid particles in an electric field.

The governing equation for mass transport is the continuity equation. It can be written under steady-state conditions and in the absence of reactions in vector form as:

$$\nabla \cdot \mathbf{j} = 0, \quad (2.12)$$

where  $\mathbf{j}$  includes all flux density components concerning different mass transport mechanisms. The molecular mass transport is governed with Fick's first law

$$\mathbf{j}_D = -D\nabla n, \quad (2.13)$$

where  $\mathbf{j}_D$  is diffusive flux density of some species,  $D$  and  $n$  are its diffusion coefficient and concentration, respectively. Hence, the diffusive flux is proportional to the concentration gradient and will stop if the concentration of the species is identical everywhere. The convective flux density can be determined as

$$\mathbf{j}_C = n\mathbf{v}. \quad (2.14)$$

If the species possesses an electrical charge then it can be driven with an applied electric field. The accompanying migration flux is defined by the local electric field

$$\mathbf{j}_M = -D \frac{zq_e n}{k_B T} \nabla \Phi, \quad (2.15)$$

where  $z$ ,  $q_e$ ,  $\Phi$  are the species' valence, the elementary charge, and local electric potential, respectively, with  $k_B$  and  $T$  being the Boltzmann constant and absolute temperature. Thus, assuming that mass transport is due to the three mechanisms mentioned above Eq. 2.12 can be written as

$$\nabla^2 n - \nabla \cdot \left( \frac{\mathbf{v}}{D} n \right) + \nabla \cdot \left( \frac{zq_e n}{k_B T} \nabla \Phi \right) = 0. \quad (2.16)$$

This equation is called the steady-state *Nernst-Planck* equation. Thus, the concentration of electrically charged species is determined, apart from the velocity field, also by the electric potential distribution. This distribution can be obtained from solution of the *Poisson* equation

$$\nabla^2 \Phi = -\frac{\rho_q}{\epsilon_0 \epsilon_r}, \quad (2.17)$$

where  $\rho_q$  is the electric charge density that, in general, can consist of  $N$  species with different number concentration  $n_i$  and valence  $z_i$

$$\rho_q = \sum_{i=1}^N z_i q_e n_i, \quad (2.18)$$

and  $\epsilon_0 \epsilon_r$  is the dielectric permittivity of the solution. It should be noted that transport of each individual species in a multi-component solution can be described, as before, with Eq. 2.16. However, the electric charge distribution is affected as well by “external” factors. For instance, the presence of a surface electric charge at the solid-liquid interface can dramatically change the picture of electric charge distribution in a liquid.

### 2.3. Electric double layer

A solid-liquid interface can appear as the source of a number of phenomena that define properties of a whole system. One of these phenomena is the formation of the electric double layer in a liquid region adjacent to a charged solid wall. Most solids gain an electrical surface charge when they are immersed in a polar solvent, e.g. an electrolyte solution. This charge can be the result of diverse processes [2]: preferential adsorption of ions in solution; adsorption-desorption of lattice ions; direct dissociation or ionisation of surface groups; charge defective lattice, etc. The excess surface electric charge results in the rearrangement of electrolyte ions in close vicinity to the interface and the surface charge is compensated by counterions maintaining the electroneutrality of the system. Both the surface charge and its balancing countercharge in the liquid form the electrical double layer or EDL (Fig. 2.3). Immediately next to the solid-liquid interface, there are ions that undergo very strong electrostatic attraction to the interface and are considered immobile. They form the Stern layer (or inner part of the double layer) which is normally a few Ångstroms thick. Still further from the surface ions are affected less by the electrostatic interaction, are mobile, and can be displaced by thermal Brownian motion. These ions form the diffusive layer (or outer part of the double layer), which is separated from the inner part by the so-called Stern plane. Because the ions in the Stern layer are immobile, the hypothetical dividing plane between a moving solution and

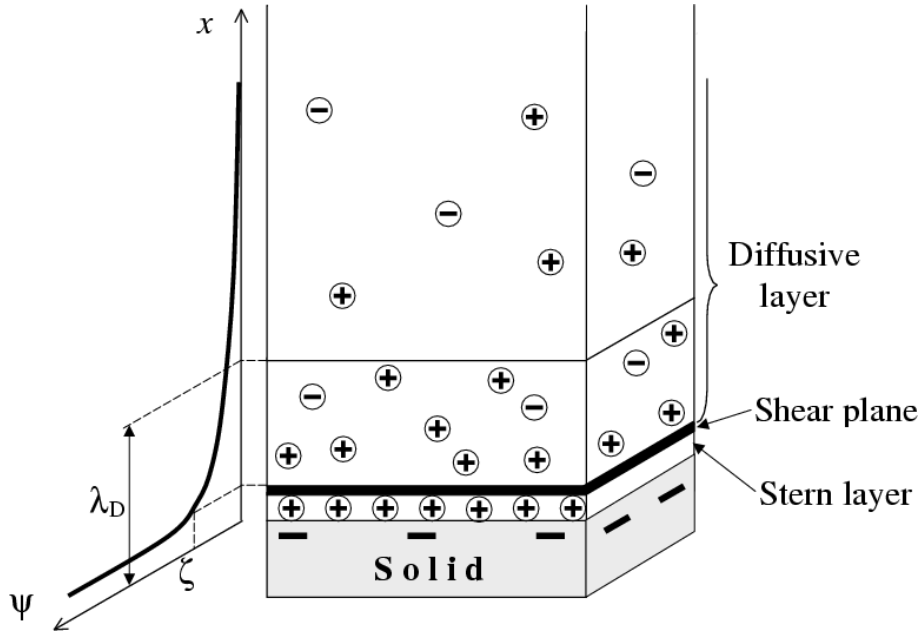


**Figure 2.3.** Schematic presentation for the distribution of ions near a solid-liquid interface and for the variation of electrostatic potential from the solid surface to the liquid ( $x$ -direction).

“fixed” ions can be referred to as the shear plane. The exact location of the shear plane, that is actually a very thin region in which viscosity effects change quite rapidly, is difficult to determine and is the matter of ongoing investigations. However, the shear plane location is usually assumed to be just outside the Stern layer, which implies that the potential at that plane,  $\zeta$  or zeta-potential, will be slightly less than the potential at the Stern plane,  $\psi_s$ . Moreover,  $\psi_s$  and  $\zeta$  (or the Stern and shear plane locations) can be considered identical, since any introduced error will be small under ordinary circumstances [3]. The spatial distribution of ions in the diffusive layer can be described with the coupled Boltzmann distribution

$$n_i = n_i^0 \exp\left(-\frac{\Delta G_i}{k_B T}\right) \quad \text{or} \quad n_i = n_i^0 \exp\left(-\frac{q_i z_i \Psi}{k_B T}\right) \quad (2.19)$$

and Coulomb law

$$\nabla^2 \Psi = -\frac{\rho_q}{\epsilon_0 \epsilon_r} \quad (2.20)$$



The former relates the average number concentration  $n$  with a free (or potential) energy  $\Delta G$  determined to a specified reference state (with a zero free/potential energy and corresponding average number concentration  $n^0$ ). Equation 2.20 describes the relationship between the local electrical potential  $\psi$  and net charge density  $\rho_q$ , which can be defined for a multi-component electrolyte as

$$\rho_q = \sum_i q_e z_i n_i^0 \exp\left(-\frac{q_e z_i \psi}{k_B T}\right). \quad (2.21)$$

The combination of Eqs. 2.19, 2.20, and 2.21 results in the *Poisson-Boltzmann* equation

$$\nabla^2 \psi = -\frac{1}{\epsilon_0 \epsilon_r} \sum_i q_e z_i n_i^0 \exp\left(-\frac{q_e z_i \psi}{k_B T}\right), \quad (2.22)$$

where  $n_i^0$  is the number concentration in an electroneutral region.

It should be noted that, though there is no general analytical solution to this equation, in certain particular cases an approximated solution can be obtained. For example, for a flat solid-liquid interface with a low electric potential a solution for Eq. 2.22 can be realized with the *Debye-Hückel* approximation, assuming

$$\exp\left(-\frac{q_e z_i \psi}{k_B T}\right) \approx 1 - \frac{q_e z_i \psi}{k_B T}. \quad (2.23)$$

This allows to rewrite Eq. 2.22 in the following form

$$\nabla^2 \psi = \kappa^2 \psi, \quad (2.24)$$

with  $\kappa$  being

$$\kappa = \left( \frac{\epsilon_0 \epsilon_r k_B T}{q_e^2 \sum_i z_i n_i^0} \right)^{-1/2}. \quad (2.25)$$

The parameter  $\lambda_D = \kappa^{-1}$ , commonly referred as the “Debye screening length”, is identified as the thickness of the electrical double layer near a flat interface. Using the above mentioned approximation, the solution for Eq. 2.24 can be written as

$$\psi = \zeta \exp(-x/\lambda_D), \quad (2.26)$$

where  $x$  is the distance from the solid surface. It should be pointed out that the analytical solution to Eq. 2.22 for a flat interface can be obtained, as well for arbitrary potential, in the case of a symmetrical electrolyte ( $z_1 = -z_2 = z$ )

$$\psi = \frac{2k_B T}{q_e z} \ln \left[ \frac{1 + \exp\left(-x/\lambda_D\right) \tanh\left(q_e z \zeta / 4k_B T\right)}{1 - \exp\left(-x/\lambda_D\right) \tanh\left(q_e z \zeta / 4k_B T\right)} \right]. \quad (2.27)$$

In Fig. 2.4 the difference between the potential distributions calculated by Eq. 2.26 (the Debye-Hückel approximation) and Eq. 2.27 is shown.

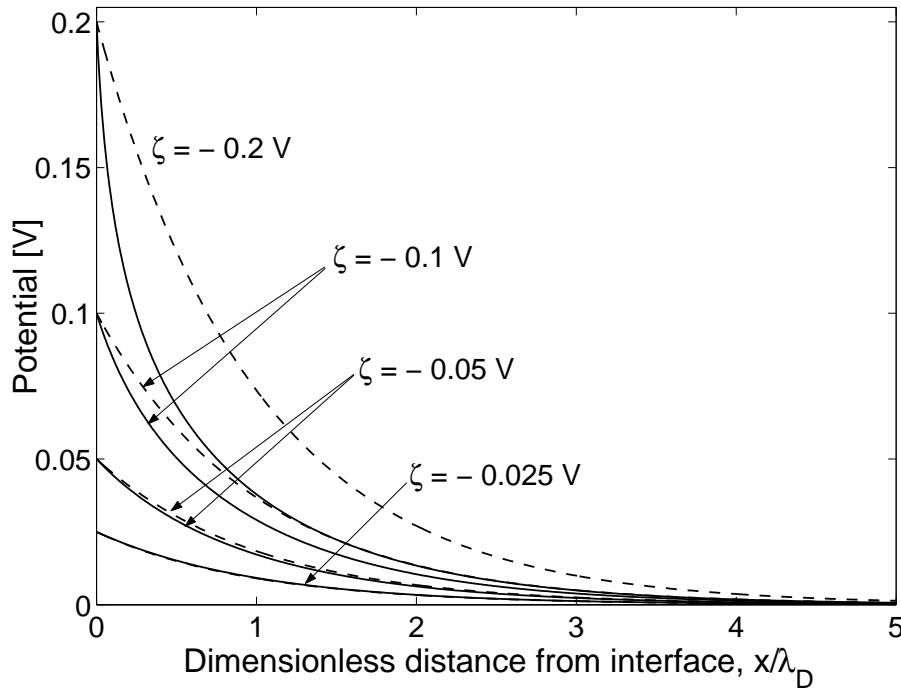


**Figure 2.4.** Electrostatic potential distribution near a flat solid-liquid interface (symmetric monovalent electrolyte) calculated by using the Debye-Hückel approximation (dashed lines, Eq. 2.26) and full calculation (solid lines, Eq. 2.27) for different values of  $\zeta$ .

## 2.4. Electroosmosis and mass transport

The existence of the electrical charge imbalance in vicinity of a solid-liquid interface can result in a number of phenomena under the influence of an applied electric field. Those phenomena are collectively defined as electrokinetic phenomena and include, in particular, electromigration, electroosmosis, electrophoresis, sedimentation potential, streaming potential and streaming current, electrolysis, electrorotation, etc. Hereafter, the attention will be focused on the first two effects as main sources of mass transport in an electrolyte solution. They can be distinguished from one another as follow:

- *Electromigration* — migration of individual ions induced by an applied electric field.
- *Electroosmosis* — flow of bulk fluid phase induced by electromigration in an applied electric field.

Evidently, the former phenomenon is the origin for the latter and, consequently, a theoretical model of electroosmosis inherently has to treat electromigration.

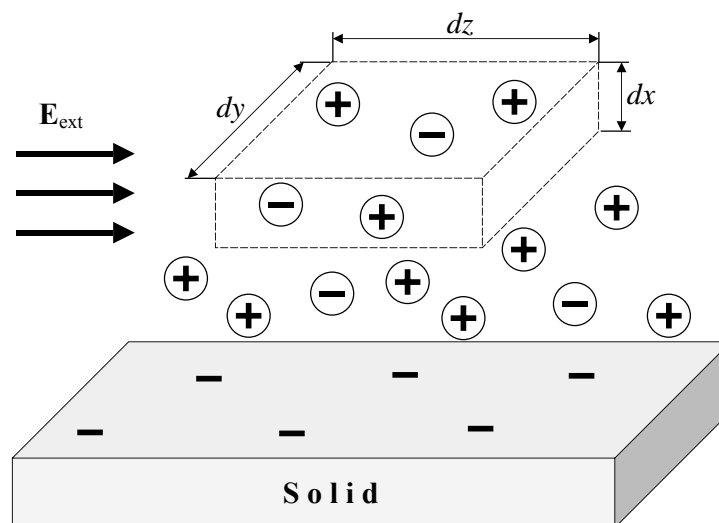


**Figure 2.5.** Electroosmotic flow generated by motion of ions due to an applied electric field.

The theory of electroosmotic flow was developed by Von Smoluchowski [4]. He considered the movement of a liquid adjacent to a flat, uniformly charged surface under the influence of an external electric field  $E_{\text{ext}}$  applied parallel to the interface (Fig. 2.5). According to that model, the velocity of the liquid  $v_z$  in the direction parallel to the wall increases from zero in the inner Helmholtz plane to a maximum value  $v_{\text{osm}}$  at some distance (ca.  $5\lambda_D$ ) from the solid-liquid interface. Consider an unit volume of the liquid  $dx dy dz$ . In steady state the net force generated by the friction of liquid and the applied electrical field should be zero

$$\rho_q(x)E_{\text{ext}} + \eta \frac{d^2 v_z}{dx^2} = 0 \quad (2.28)$$

or, using Eq. 2.20,

$$\varepsilon_0 \varepsilon_r \frac{d^2 \psi(x)}{dx^2} E_{\text{ext}} = \eta \frac{d^2 v_z}{dx^2}. \quad (2.29)$$

This equation can be integrated from a point far from the solid-liquid interface ( $x \rightarrow \infty$ ) up to the shear plane ( $x = 0$ ) with the conditions

$$\begin{aligned} \psi|_{x=0} &= \zeta & v_z|_{x=0} &= 0 \\ \psi|_{x \rightarrow \infty} &= 0 & v_z|_{x \rightarrow \infty} &= v_\infty \end{aligned}$$

$$\begin{aligned} \left. \frac{d\psi}{dx} \right|_{x \rightarrow \infty} &= 0 \\ \left. \frac{dv_z}{dx} \right|_{x \rightarrow \infty} &= 0 \end{aligned},$$

where  $v_\infty$  is defined by the Helmholtz-Smoluchowski equation:

$$v_\infty = -E_{\text{ext}} \frac{\varepsilon_0 \varepsilon_r \zeta}{\eta}.$$

The result of the integraton is:

$$v_z(x) = -E_{\text{ext}} \frac{\varepsilon_0 \varepsilon_r [\zeta - \psi(x)]}{\eta}. \quad (2.30)$$

Since the right-hand side of Eq. 2.30 includes the electrical potential, an explicit expression for the electroosmotic velocity distribution requires to solve the Poisson-Boltzmann problem. Therefore, the analytical solution for the electroosmotic velocity field is possible only for very simple geometries (e.g., a flat homogeneous interface) or can be obtained under certain assumptions (e.g., low zeta-potential, large capillary diameter compared to the double-layer thickness, etc.). Thus, as well as for the Poisson-Boltzmann problem, the solution for the electroosmotic velocity field can be obtained basically only by numerical methods.

## **References**

1. J. L. Plawsky. *Transport Phenomena Fundamentals*. Marcel Dekker, New York, 2001.
2. A.V. Delgado and F.J. Arroyo. Electrokinetic Phenomena and Their Experimental Determination, an Overview. In *Interfacial Electrokinetics and Electrophoresis*; A.V. Delgado (ed.), Marcel Dekker, New York, 2002.
3. D. Myers. *Surfaces, Interfaces, and Colloids*. Wiley-VCH, Weinheim, 1999.
4. M.Von Smoluchowski. *Handbuch der Elektrizität und des Magnetismus*. Barth, Leipzig, 1921.

## Chapter 3

# Computational Methods

### 3.1. General simulation approach

As it was mentioned in the Introduction, a comprehensive simulation of electrokinetic phenomena and their constitutive part, electroosmotic flow, should include an extensive set of different physical and chemical processes. As long as the solution to such simulation problem is impracticable at least nowadays, it should be formulated with certain assumptions and approximations. It is obvious that the choice of assumptions affects the simulation results and some correction should be performed during their translation to an actual system. On the other hand, the contribution of the neglected phenomena to the total picture can be very small and the behavior of the real system practically will not differ, in such case, from the simulated one. Hence, the choice of applied assumptions and the necessity of the correction of simulated results during their translating to the description of an actual system depend on the concrete situation and, vice versa, the concrete mathematical (or numerical) description of electrokinetic phenomena can represent the actual system only under these assumptions.

The theoretical backgrounds of electrokinetic phenomena presented in Chapter 2 have the following general assumptions:

- the system is isothermal (in particular, there are no Joule heating effects);
- it is a steady-state system (no transient effects);
- the mean-field approximation is applied for energy calculations (the mean field means substituting the interaction among the fields at different locations by the interaction of the field at each site with the mean field value at different locations);
- the liquid phase is Newtonian (constant viscosity);
- dielectric constants do not depend on the local electric field (no polarization effects);
- dielectric constants do not depend on the liquid density (no electrostriction effects);

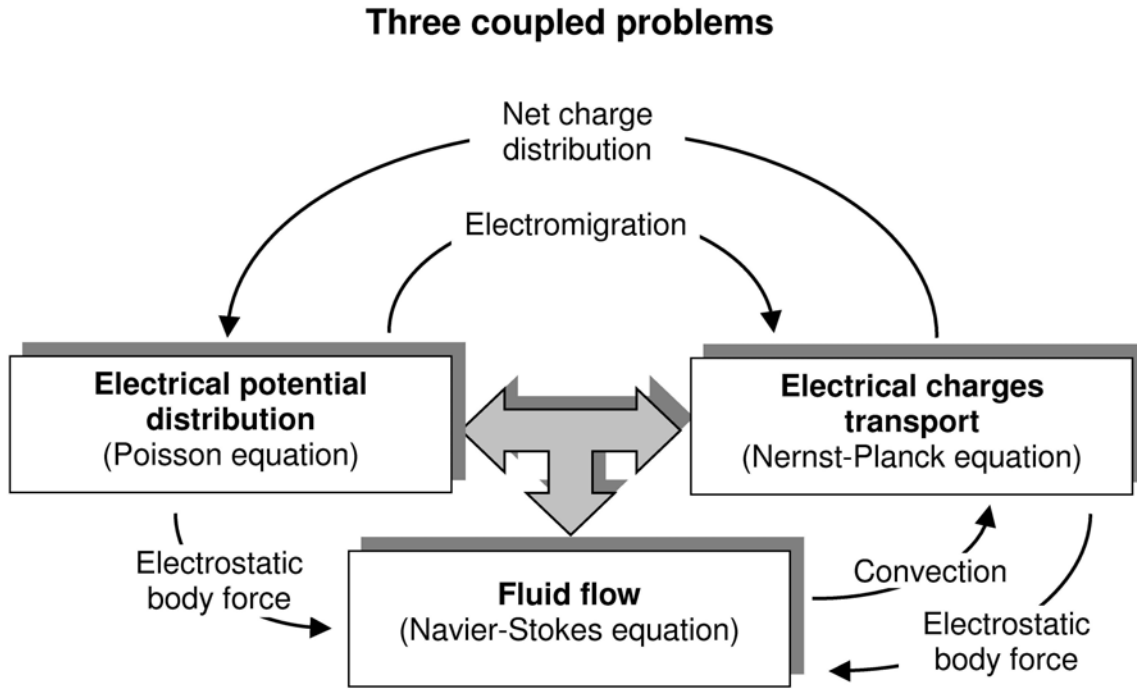


**Figure 3.1.** General simulation approach to electroosmotic phenomena.

Accepting the aforementioned set of assumptions the simulation of electroosmotic flow can be reduced to coupled modeling of the electrical potential distribution, species transport and fluid flow (Fig. 3.1). Solutions to these three problems for a Newtonian  $N$ -component electrolyte can be obtained by resolving of the Poisson, steady-state Nernst-Planck, and Navier-Stokes equations (see chapter 2), respectively:

$$\nabla^2 \psi = -q_e \sum_{i=1}^N z_i n_i / \epsilon_0 \epsilon_r,$$

$$\nabla^2 n_i - \nabla \left( \frac{\mathbf{v}}{D_i} n_i \right) + \nabla \left( \frac{z_i q_e n_i}{k_B T} \nabla \psi \right) = 0,$$

$$\frac{\partial}{\partial t} (\rho \mathbf{v}) = -[\nabla \cdot (\rho \mathbf{v}) \mathbf{v}] - \nabla \cdot \boldsymbol{\tau} - \nabla p + \rho \mathbf{g} + \frac{\mathbf{F}}{\Delta x \Delta y \Delta z}.$$



It should be pointed out that the presented mathematical description includes hydraulic flow problems as a particular case, in the absence of the externally applied electric field.

The resulting electrical potential, species concentration and flow velocity distributions are coupled by a number of phenomena which are indicated in Fig. 3.1 by arrows. In order to solve the above set of equations, an iterative numerical procedure based on finite-difference (for solution of the Poisson and Nernst-Planck equations) and lattice-Boltzmann (for solution of the Navier-Stokes equation) techniques was developed. While the finite-difference methodology is quite traditional for numerical solution of differential equation problems, the lattice-Boltzmann approach is a relatively novel method in computational hydrodynamics. Therefore, this approach will be regarded in more detail below. The details of the numerical implementations of the whole procedure, in particular the solution of the Poisson and Nernst-Planck equations, are presented in Section 4.1. of this thesis.

### **3.2. Lattice-Boltzmann hydrodynamics**

#### *3.2.1 Methods in Computational Fluid Dynamics*

In the previous chapter of this thesis it has been shown that fluid motion is governed by the Navier-Stokes equations which allow analytical solution in only a small number of special cases. With the advent of computer technology attempts have been made at simulating fluid flow on computers, i.e. Computational Fluid Dynamics (CFD). There are two CFD methods that are used to simulate fluid flow: i) the direct numerical solution of Navier-Stokes equations, which treats the fluid as continuous matter at the macroscopic level, and ii) the particle methods, which retain the physical idea that the fluid is composed of a collection of molecules at the microscopic level.

The numerical solution of Navier-Stokes equations assumes finding a mathematical solution for the differential continuum equation after its discretization by means of finite-difference, finite-element, or other standard numerical techniques. However, the difficulties with grid generation for complex boundaries, high computational requirements for memory capacity and computational speed, and the problem with numerical stability often restrict the use of this approach.

One of the most known particle methods is the molecular dynamics. Theoretically, molecular dynamics simulations are able to provide solutions for any flow problem. However, because huge numbers of molecules have to be used to present the fluid being modeled, they require large amounts of computer memory and CPU time. Even high performance computers

can operate only a very small amount of molecules when compared with the number of those found in real fluid-dynamical systems.

Over the last 15 years, a new alternative particle method for the computer simulation of fluids has been developed. This method is based on a discrete approximation of the Boltzmann kinetic equation (the lattice Boltzmann equation) and referred to in the literature as the lattice Boltzmann equation method(s) or LBE method. Since then, the LBE method has been intensively pursued and has found application in different areas of CFD, including fluid flow simulations in porous media. It has recently been shown [1,2] that this discrete-velocity model corresponds to the truncation of the Boltzmann equation in an Hermite velocity spectrum space or, in other words, that it can be viewed as a special finite-difference approximation of the Boltzmann equation.

### 3.2.2 The Boltzmann and lattice Boltzmann equations

Consider a system of  $N$  identical classical (in a physical sense) particles. The state of this system is described by  $6N$  position coordinates and velocity components. Let us refer to the corresponding  $6N$ -dimensional phase space as  $\Gamma$ -space; any point in this space describes a state of the system. Further, introduce a six-dimensional space corresponding to the position and velocity of an individual particle and call this space  $\gamma$ -space. Each of  $N$  particles is represented by a single point in  $\gamma$ -space. Hence, the state of the system represented by one point in  $\Gamma$ -space gets mapped to a configuration of  $N$  points in  $\gamma$ -space and the time evolution of the system giving rise to a trajectory in  $\Gamma$ -space gets mapped to  $N$  trajectories of  $N$  points in  $\gamma$ -space.

Such statistical system can be described with the distribution function  $\mathcal{F}(\mathbf{r}, \mathbf{u}, t)$  introduced in the  $\gamma$ -space that defines  $dN(\mathbf{r}, \mathbf{u}, t) = \mathcal{F}(\mathbf{r}, \mathbf{u}, t) d\mathbf{r} d\mathbf{u}$  as the number of molecules at time  $t$  being positioned at  $[\mathbf{r}, \mathbf{r}+d\mathbf{r}]$  and having velocities in the range  $[\mathbf{u}, \mathbf{u}+d\mathbf{u}]$ . The difference between  $dN(\mathbf{r}, \mathbf{u}, t)$  and  $dN(\mathbf{r}+\mathbf{u}\Delta t, \mathbf{u}+\mathbf{a}\Delta t, t+\Delta t)$ , where  $\Delta t$  is a short time and  $\mathbf{a}$  is the acceleration due to external forces, can result from collisions and it can be written as

$$[\mathcal{F}(\mathbf{r} + \mathbf{u}\Delta t, \mathbf{u} + \mathbf{a}\Delta t, t + \Delta t) - \mathcal{F}(\mathbf{r}, \mathbf{u}, t)] d\mathbf{r} d\mathbf{u} = \left( \frac{\partial \mathcal{F}}{\partial t} \right)_c d\mathbf{r} d\mathbf{u} \Delta t, \quad (3.1)$$

where  $(\partial\mathcal{F}/\partial t)_c$  is the time rate of change of  $\mathcal{F}$  due to collisions. After expanding the first term on the left hand side of Eq. 3.1 as a Taylor series about  $\mathcal{F}(\mathbf{r},\mathbf{u},t)$  and letting  $\Delta t \rightarrow 0$  this equation can be rewritten:

$$\frac{\partial\mathcal{F}}{\partial t} + (\mathbf{u} \cdot \nabla_{\mathbf{r}})\mathcal{F} + (\mathbf{a} \cdot \nabla_{\mathbf{u}})\mathcal{F} = \left( \frac{\partial\mathcal{F}}{\partial t} \right)_c, \quad (3.2)$$

with  $\nabla_{\mathbf{r}} = \frac{\partial}{\partial \mathbf{r}}$  and  $\nabla_{\mathbf{u}} = \frac{\partial}{\partial \mathbf{u}}$ . Equation 3.2 is known as the *Boltzmann equation* and it describes the dynamics of the particle distribution function  $\mathcal{F}(\mathbf{r},\mathbf{u},t)$ . It should be noted that the complete form of Eq. 3.2 assumes the collision term on the right hand side has to be explicitly specified. In general case, the form of the collision term can be very complex and depends on the system. Consider several assumptions [3]:

- Only binary collisions are taken into account (the dilute gas).
- The velocity of a particle is uncorrelated with its position (the molecular chaos assumption).
- Wall effects are ignored (the unconfined system).
- The effect of external forces on the collision cross section is neglected.

Under these assumptions the collision term can be expressed as:

$$\left( \frac{\partial\mathcal{F}}{\partial t} \right)_c = \int d\mathbf{u} d\Omega_c (\mathcal{F}'_1 \mathcal{F}'_2 - \mathcal{F}_1 \mathcal{F}_2) |\mathbf{u}_1 - \mathbf{u}_2| \sigma(|\mathbf{u}_1 - \mathbf{u}_2|, \Omega_c), \quad (3.3)$$

where  $\Omega_c$  is the scattering direction of the binary collision  $\mathbf{u}_1 + \mathbf{u}_2 \rightarrow \mathbf{u}'_1 + \mathbf{u}'_2$  and  $\sigma$  is the differential cross section of that collision. This collision term can be significantly simplified for states *close to thermal equilibrium*. Since the classical ideal gas relaxes to the Maxwell-Boltzmann distribution (Maxwellian)

$$\mathcal{F}^{\text{eq}}(\mathbf{r}, \mathbf{u}, t) = \rho(\mathbf{r}, \mathbf{u}, t) \sqrt{\frac{m}{(2\pi k_B T)^3}} \exp\left[-\frac{m(\mathbf{u} - \mathbf{v})^2}{2k_B T}\right], \quad (3.4)$$

where  $\rho$  and  $\mathbf{v}$  are the density and macroscopic (or average) velocity, respectively, this function should emerge as an equilibrium solution of the Boltzmann equation for a system at temperature  $T$ , consisting of particles of mass  $m$ , and it can be shown that Maxwellian

describes a fraction of the particles in a given small volume undergoing collisions. Hence, the collision term can be defined as

$$\left(\frac{\partial \mathcal{F}}{\partial t}\right)_c = -\frac{\mathcal{F} - \mathcal{F}^{\text{eq}}}{\tau}, \quad (3.5)$$

in the form known as the ‘‘BGK collision operator’’ [4], where  $\tau$  is a relaxation time. Thus, under the assumption of a local proximity to thermal equilibrium it can be expected that the arbitrary distribution function evolves according to the Boltzmann equation and eventually relaxes to the equilibrium Maxwellian. The Boltzmann equation with BGK collision operator has the following form:

$$\frac{\partial \mathcal{F}}{\partial t} + (\mathbf{u} \cdot \nabla_{\mathbf{r}}) \mathcal{F} + (\mathbf{a} \cdot \nabla_{\mathbf{u}}) \mathcal{F} = -\frac{\mathcal{F} - \mathcal{F}^{\text{eq}}}{\tau}. \quad (3.6)$$

Macroscopic quantities of the system such as the density  $\rho$ , velocity  $\mathbf{v}$ , and temperature  $T$  (or average internal energy), can all be determined from the given distribution function  $\mathcal{F}(\mathbf{r}, \mathbf{u}, t)$  by calculating its velocity moments:

$$\rho(\mathbf{r}, t) = \int m \mathcal{F}(\mathbf{r}, \mathbf{u}, t) d\mathbf{u}, \quad (3.7)$$

$$\mathbf{v}(\mathbf{r}, t) = \frac{1}{\rho(\mathbf{r}, t)} \int m \mathbf{u} \mathcal{F}(\mathbf{r}, \mathbf{u}, t) d\mathbf{u}, \quad (3.8)$$

$$T(\mathbf{r}, t) = \frac{m^2}{3k_B \rho(\mathbf{r}, t)} \int (\mathbf{u} - \mathbf{v})^2 \mathcal{F}(\mathbf{r}, \mathbf{u}, t) d\mathbf{u}. \quad (3.9)$$

Taking Maxwellian velocity distribution function into the moment equations leads to the Euler equations for the velocity  $\mathbf{v}$ , i.e. Navier-Stokes equations without viscosity.

Generally, the approximate solutions to the Boltzmann equation can be obtained by means of a perturbation technique [5], applying the Chapman-Enskog expansion, which is essentially a formal multi-scale expansion and commonly used in statistical physics. This method of successive approximations can, in principle, be extended to systems in which gradients of thermodynamic quantities are quite large. In the zeroth approximation, the distribution function is locally Maxwellian, and we obtain the Euler equations of change. The

first-order perturbation leads to the Navier-Stokes equations. It should be realized that the Navier-Stokes equations apply to systems in which the gradients in the physical properties are small, i.e. in which the physical properties do not change appreciable within a distance of the mean free path length. The second-order perturbation gives the Burnett equations. From the higher approximations more complicated equations result in which the flux vectors depend progressively on higher derivatives of the thermodynamic quantities and higher powers of the lower derivatives.

The series solution to the Boltzmann equation is obtained by introducing a perturbation parameter  $\chi$  into the equation in such way that the frequency of collisions can be varied in an arbitrary manner without affecting the relative number of collisions of a particular kind. Hence, we can consider a hypothetical problem in which the Boltzmann equation with BGK collision operator is

$$\frac{\partial \mathcal{F}}{\partial t} + (\mathbf{u} \cdot \nabla_{\mathbf{r}}) \mathcal{F} + (\mathbf{a} \cdot \nabla_{\mathbf{u}}) \mathcal{F} = -\frac{\mathcal{F} - \mathcal{F}^{\text{eq}}}{\tau \chi} \quad (3.10)$$

and  $1/\chi$  measures the frequency of collisions. If  $\chi$  was small, collisions would be very frequent and the system behave like a continuum in which local equilibrium is everywhere maintained. The distribution function, too, is expanded in series in  $\chi$

$$\mathcal{F} = \mathcal{F}^{\text{eq}} + \mathcal{F}^{\text{neq}} = \mathcal{F}^{[0]} + \chi \mathcal{F}^{[1]} + \chi^2 \mathcal{F}^{[2]} + \dots = \mathcal{F}^{[0]} + \sum_{n=1}^{\infty} \chi^n \mathcal{F}^{[n]}, \quad (3.11)$$

Introducing this series into Eq. 3.10 and equating the coefficients of equal powers of  $\chi$ , one can obtain the set of the balance equations for the functions  $\mathcal{F}^{[0]}$ ,  $\mathcal{F}^{[1]}$ ,  $\mathcal{F}^{[2]}$ , ... . In order to find consistent and unique solutions for functions  $\mathcal{F}^{[n]}$ , the following constraints must be satisfied:

$$\int m \mathcal{F}^{[0]} \begin{bmatrix} 1 \\ \mathbf{u} \\ (\mathbf{u} - \mathbf{v})^2 \end{bmatrix} d\mathbf{u} = \rho \begin{bmatrix} 1 \\ \mathbf{v} \\ \frac{3k_B T}{m} \end{bmatrix} \quad \text{and} \quad \int m \mathcal{F}^{[n]} \begin{bmatrix} 1 \\ \mathbf{u} \\ (\mathbf{u} - \mathbf{v})^2 \end{bmatrix} d\mathbf{u} = 0, \quad n > 0.$$

The general solution to the ( $\chi^{-1}$ ) order equation is trivial and yields the Maxwellian equilibrium distribution function,  $\mathcal{F}^{[0]} = \mathcal{F}^{\text{eq}}$  (Eq. 3.4). The solution for the first-order perturbation function  $\mathcal{F}^{[1]}$  is

$$\mathcal{F}^{[1]} = -\tau \left( \frac{\partial \mathcal{F}^{[0]}}{\partial t} + (\mathbf{u} \cdot \nabla) \mathcal{F}^{[0]} \right). \quad (3.12)$$

The hydrodynamic equations can be obtained by evaluating the moments of the Boltzmann equation:

$$\int \left( \frac{\partial \mathcal{F}}{\partial t} + (\mathbf{u} \cdot \nabla) \mathcal{F} \right) \begin{bmatrix} 1 \\ \mathbf{v} \\ (\mathbf{u} - \mathbf{v})^2 \end{bmatrix} = 0. \quad (3.13)$$

The substitutions  $\mathcal{F} = \mathcal{F}^{[0]}$  and  $\mathcal{F} = \mathcal{F}^{[0]} + \mathcal{F}^{[1]}$  in the above expression lead to the Euler and Navier-Stokes equations, respectively.

From the point of view of computational methodology these obtained results indicate that distributions of thermodynamic quantities can be obtained besides an immediate numerical solution of the Navier-Stokes equations, as well by molecular dynamics simulations. However, as it was mentioned in the beginning of this chapter, even high performance computer simulations are not able to provide a satisfactory representation of real fluid-dynamics systems by modeling of molecular dynamics. Dynamic simulation of many-body systems in continuous phase space requires a large amount of computational resources which exponentially grow with increasing system population. Since the passage from a continuous representation to a discrete one is conventional for computational mathematics, it was quite logically when the continuous molecular dynamic problem had translated to that in discrete phase space and the continuous Boltzmann equation had been transformed to the lattice-Boltzmann equation. Although historically the lattice-Boltzmann equation was developed empirically, with basic ideas borrowed from the cellular automata fluids [6], in 1997 it was shown that the lattice-Boltzmann equation can be obtained as a special finite-difference form of the Boltzmann equation for discrete velocities by a small Mach number expansion [1,2].

The starting point in those derivations is the Boltzmann BGK equation (Eq. 3.6) formally rewritten in the form of an ordinary differential equation:

$$\frac{\partial \mathcal{F}}{\partial t} = -\frac{\mathcal{F} - \mathcal{F}^{\text{eq}}}{\tau} - (\mathbf{u} \cdot \nabla_{\mathbf{r}}) \mathcal{F} - (\mathbf{a} \cdot \nabla_{\mathbf{u}}) \mathcal{F}. \quad (3.14)$$

The derivative  $\nabla_{\mathbf{u}} \mathcal{F}$  cannot be evaluated directly because the dependence of the distribution function on the microscopic velocity is unknown. In order to simplify the forcing term of the Boltzmann BGK equation, the following assumption can be made [6] (the assumption of small deviation from the local equilibrium):

$$\nabla_{\mathbf{u}} \mathcal{F} \approx \nabla_{\mathbf{u}} \mathcal{F}^{\text{eq}},$$

that allows to approximate the forcing term:

$$(\mathbf{a} \cdot \nabla_{\mathbf{u}}) \mathcal{F} \approx -\frac{m\mathbf{a} \cdot (\mathbf{u} - \mathbf{v})}{k_{\text{B}}T} \mathcal{F}^{\text{eq}}.$$

Hence, formal integration of Eq 3.14 along characteristic line  $\mathbf{u}$  over a time step  $\delta_t$  results in:

$$\mathcal{F}(\mathbf{r} + \mathbf{u}\delta_t, \mathbf{u}, t + \delta_t) - \mathcal{F}(\mathbf{r}, \mathbf{u}, t) = -\int_t^{t+\delta_t} \frac{\mathcal{F} - \mathcal{F}^{\text{eq}}}{\tau} dt + \int_t^{t+\delta_t} \frac{m\mathbf{a} \cdot (\mathbf{u} - \mathbf{v})}{k_{\text{B}}T} \mathcal{F}^{\text{eq}} dt.$$

The first integral is treated explicitly, assuming that the integrand is constant over one time step  $\delta_t$ , while the second one can be treated using the trapezoidal implicit scheme [7]. With these assumptions and approximations, the above equation becomes

$$\begin{aligned} \mathcal{F}(\mathbf{r} + \mathbf{u}\delta_t, \mathbf{u}, t + \delta_t) - \mathcal{F}(\mathbf{r}, \mathbf{u}, t) = & -\frac{1}{\tau} \left[ (\mathcal{F}(\mathbf{r}, \mathbf{u}, t) - \mathcal{F}^{\text{eq}}(\mathbf{r}, \mathbf{u}, t)) \right] + \\ & \frac{\delta_t}{2} \left[ \frac{m\mathbf{a} \cdot (\mathbf{u} - \mathbf{v})}{k_{\text{B}}T} \mathcal{F}^{\text{eq}} \Big|_{t+\delta_t} + \frac{m\mathbf{a} \cdot (\mathbf{u} - \mathbf{v})}{k_{\text{B}}T} \mathcal{F}^{\text{eq}} \Big|_t \right], \end{aligned} \quad (3.15)$$

where  $\tau = \tau / \delta_t$  is the dimensionless relaxation time. In order to numerically evaluate the velocity moments of the distribution function, Eqs. 3.7-3.9, the integration in momentum space has to be approximated by the Gaussian-type quadrature, that is

$$\int \Xi(\mathbf{u}) \mathcal{F}(\mathbf{r}, \mathbf{u}, t) d\mathbf{u} \approx \sum_{\alpha} W_{\alpha} \Xi(\mathbf{u}_{\alpha}) \mathcal{F}(\mathbf{r}, \mathbf{u}_{\alpha}, t), \quad (3.16)$$

where  $\Xi(\mathbf{u}) = [1; u_i; (u_i u_j); (u_i u_j u_k); \dots]$  are polynomials of  $\mathbf{u}$ ,  $W_\alpha$  are the weight coefficients of the quadrature, and  $\mathbf{u}_\alpha$  are the discrete velocity set or the abscissas of the quadrature. Accordingly, Eqs. 3.16 can be considered as approximated analogues of Eqs. 3.7-3.9 and serve to calculate the thermodynamic quantities

$$\rho(\mathbf{r}, t) = \sum_{\alpha} \mathcal{F}_{\alpha}(\mathbf{r}, t), \quad (3.17)$$

$$\mathbf{v}(\mathbf{r}, t) = \frac{1}{\rho(\mathbf{r}, t)} \sum_{\alpha} \mathbf{u}_{\alpha} \mathcal{F}_{\alpha}(\mathbf{r}, t), \quad (3.18)$$

$$T(\mathbf{r}, t) = \frac{m^2}{3k_B \rho(\mathbf{r}, t)} \sum_{\alpha} (\mathbf{u}_{\alpha} - \mathbf{v})^2 \mathcal{F}_{\alpha}(\mathbf{r}, t), \quad (3.19)$$

where

$$\mathcal{F}_{\alpha} \equiv \mathcal{F}_{\alpha}(\mathbf{r}, t) \equiv W_{\alpha} \mathcal{F}(\mathbf{r}, \mathbf{u}_{\alpha}, t).$$

Then, assuming constant temperature and low Mach number (the ratio of fluid velocity  $\mathbf{v}$  to the speed of sound), the equilibrium distribution function can be expanded up to  $O(v^2)$ :

$$\mathcal{F}^{\text{eq}} = \rho \sqrt{\frac{m}{(2\pi k_B T)^3}} \exp\left(-\frac{m\mathbf{u}^2}{2k_B T}\right) \left[1 + \frac{m(\mathbf{u} \cdot \mathbf{v})}{k_B T} + \frac{m^2(\mathbf{u} \cdot \mathbf{v})^2}{2(k_B T)^2} - \frac{m(\mathbf{v} \cdot \mathbf{v})}{2(k_B T)}\right],$$

or for the discrete velocity set:

$$\mathcal{F}_{\alpha}^{\text{eq}} = W_{\alpha} \rho \sqrt{\frac{m}{(2\pi k_B T)^3}} \exp\left(-\frac{m\mathbf{u}_{\alpha}^2}{2k_B T}\right) \left[1 + \frac{m(\mathbf{u}_{\alpha} \cdot \mathbf{v})}{k_B T} + \frac{m^2(\mathbf{u}_{\alpha} \cdot \mathbf{v})^2}{2(k_B T)^2} - \frac{m(\mathbf{v} \cdot \mathbf{v})}{2(k_B T)}\right]. \quad (3.20)$$

Finally, the discrete velocity set or, in other words, the lattice geometry should be properly specified. The choice of a lattice geometry  $\{\mathbf{u}_{\alpha}\}$  must satisfy an exact preservation of the conservation laws, i.e. the used quadrature must be able to compute the thermodynamic moments *exactly*. Hence, Eq. 3.15 after the time and phase space discretizations can be rewritten as



$$\mathcal{F}_\alpha(\mathbf{r} + \mathbf{e}_\alpha, t + 1) = \mathcal{F}_\alpha(\mathbf{r}, t) - \frac{1}{\tau} \left( \mathcal{F}_\alpha(\mathbf{r}, t) - \mathcal{F}_\alpha^{\text{eq}}(\mathbf{r}, t) \right), \quad (3.21)$$

where  $\mathbf{e}_\alpha = \mathbf{u}_\alpha c = \mathbf{u}_\alpha (3k_B T / m)^{1/2}$ . The constant  $c$  is identified as “the speed of light” in the system [1],

$$c = \frac{\delta_x}{\delta_t},$$

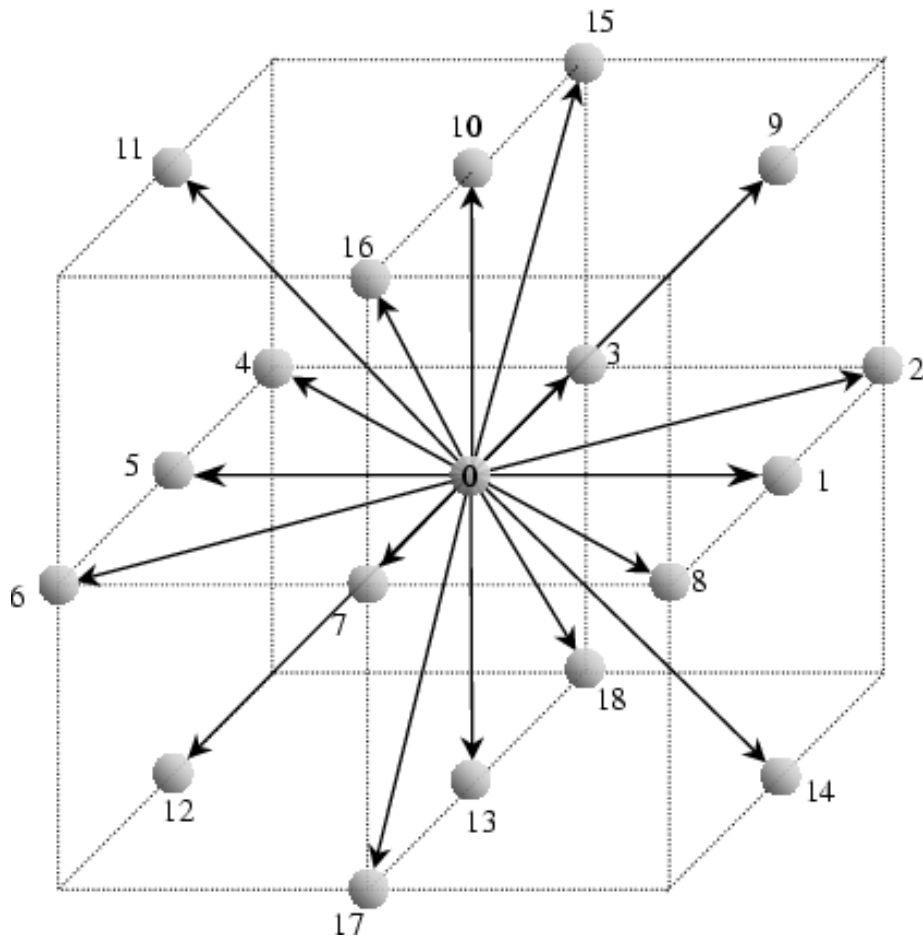


**Figure 3.2.** Lattice structure (discrete velocity set) of  $D_3Q_{19}$  lattice-BGK model.

which is usually set to be unity by the coherent discretization of space and time, and where  $\delta_x$  is the lattice constant. It should be pointed out that values of the weight coefficients  $W_\alpha$  will as well be determined by the choice of the lattice geometry.

The most regularly used lattice-Boltzmann models are  $D_2Q_7$ ,  $D_2Q_9$ ,  $D_3Q_{15}$ , and  $D_3Q_{19}$ , where  $D$  and  $Q$  denote the dimensionality of the lattice and the number of links per lattice point, respectively. In this thesis the  $D_3Q_{19}$  model (Fig. 3.2) is used for fluid flow simulations. The  $D_3Q_{19}$  model has the following set of discrete velocities

$$\mathbf{e}_\alpha = \begin{cases} (0, 0, 0), & \alpha = 0; \\ (\pm 1, 0, 0)c, (0, \pm 1, 0)c, (0, 0, \pm 1)c, & \alpha = 1, 2, \dots, 6; \\ (\pm 1, \pm 1, 0)c, (\pm 1, 0, \pm 1)c, (0, \pm 1, \pm 1)c, & \alpha = 7, 8, \dots, 18. \end{cases}$$

and weight coefficients

$$w_\alpha = W_\alpha \sqrt{\frac{m}{(2\pi k_B T)^3}} \exp\left(-\frac{m\mathbf{u}_\alpha^2}{2k_B T}\right) = \begin{cases} \frac{1}{3}, & \alpha = 0; \\ \frac{1}{18}, & \alpha = 1, 2, \dots, 6; \\ \frac{1}{36}, & \alpha = 7, 8, \dots, 18. \end{cases}$$

Hence, the equilibrium distribution function  $\mathcal{F}_\alpha^{\text{eq}}$  can be expressed as

$$\mathcal{F}_\alpha^{\text{eq}} = w_\alpha \rho \left[ 1 + \frac{3(\mathbf{e}_\alpha \cdot \mathbf{v})}{c^2} + \frac{9(\mathbf{e}_\alpha \cdot \mathbf{v})^2}{2c^4} - \frac{3\mathbf{v}^2}{2c^2} \right]. \quad (3.22)$$

### 3.2.3 Lattice-Boltzmann models with body force

In general, there are two methods available in order to incorporate a body force in the lattice-Boltzmann models:

- calculating the equilibrium distribution function with an altered velocity and
- adding an additional term to the Boltzmann equation.

The first method [8] introduces a body force by considering the produced momentum change. If a body force  $\mathbf{f}$  acts (i.e.  $\mathbf{f} = \rho\mathbf{a}$ ), then at every time-step  $\delta_t$  there exists a change of

momentum (per a unir volume)  $\delta\mathbf{p} = \mathbf{f}$ . Concerning the definition of the equilibrium distribution function (Eq. 3.22) this results in the use of a modified “equilibrium velocity”

$$\mathbf{v}^* = \mathbf{v} + \delta_t \frac{\mathbf{f}}{\rho}, \quad (3.23)$$

where  $\mathbf{v}$  is defined, as before, by Eq. 3.18.

The second way [9] assumes the modification of the lattice-Boltzmann-BGK equation (Eq. 3.21) by introducing an additional term:

$$\mathcal{F}_\alpha(\mathbf{r} + \mathbf{e}_\alpha, t + 1) = \mathcal{F}_\alpha(\mathbf{r}, t) - \frac{1}{\tau} \left( \mathcal{F}_\alpha(\mathbf{r}, t) - \mathcal{F}_\alpha^{\text{eq}}(\mathbf{r}, t) \right) + \delta_t F_\alpha, \quad (3.24)$$

and reformulating  $\mathcal{F}_\alpha^{\text{eq}}$  (Eq. 3.22) through a modified “equilibrium velocity”  $\mathbf{v}'$

$$\mathbf{v}' = \mathbf{v} + \delta_t \frac{\mathbf{f}}{2\rho},$$

where  $\mathbf{v}$  is defined by Eq. 3.18. It can be shown [9] that, in order to match the correct Navier-Stokes hydrodynamics, the body force components in Eq. 3.24 must be defined by

$$f_\alpha = w_\alpha \left( \frac{2\tau - 1}{2\tau} \right) \left[ 1 + \frac{(\mathbf{e}_\alpha - \mathbf{v}) \cdot \mathbf{v}}{c_s^2} + \frac{(\mathbf{e}_\alpha \cdot \mathbf{v})^2}{c_s^4} \right] \cdot \mathbf{f}, \quad (3.25)$$

where  $\mathbf{v}$  is the modified fluid velocity defined by

$$\mathbf{v} = \mathbf{v} + \delta_t \frac{\mathbf{f}}{2\rho},$$

and  $c_s = c / \sqrt{3}$  is the speed of sound in the system.

The first method of introducing of a body force in LBM is more suitable for simulations of flows exposed to a constant body force [9]. Since this case is, in general, not typical for electrokinetic systems, the second method was chosen to treat the body force in the EOF simulations presented in this paper.

### 3.2.4 Numerical implementation

In order to solve the lattice-Boltzmann-BGK equation the commonly utilized “stream-and-collide” algorithm was implemented. This algorithm includes two subsequent steps reiterated in turn: streaming and collision (see Algorithm 1). In the streaming phase the distribution function at each lattice node is determined by the corresponding velocity components propagated toward the node from the neighbor nodes. Then, in the collision phase, the distribution function at each lattice node is recalculated in accordance with the collision rule.

#### **Algorithm 1. Stream-and-collide algorithm**

##### *Streaming phase:*

- Propagate the distribution function components to the corresponding neighbor lattice nodes

##### *Collision phase:*

- Compute macroscopic quantities using Eqs. 3.17-3.19
- Determine the equilibrium distribution function using Eq. 3.22
- Calculate updated distribution functions using Eq. 3.21 or Eq. 3.24 depending on the method of the body force incorporation

As it has been mentioned above, the lattice-Boltzmann algorithms possess an inherent ability to be easily parallelized. This feature becomes especially significant for an implementation at parallel high-performance computers for large-scale simulations.

## **References**

1. X. He and L.-S. Luo, *J. Stat. Phys.* **88**, 927 (1997).
2. T. Abe, *J. Comp. Phys.* **131**, 241 (1997).
3. R.R. Nourgaliev, T.N. Dinh, T.G. Theofanous, and D. Joseph, *Int. J. Multiphase Flow* **29**, 117 (2003).
4. P.L. Bhatnagar, E.P. Gross, and M. Krook, *Phys. Rev.* **94**, 511 (1954).
5. S. Chapman and T.G. Cowling. *The Mathematical Theory of Non-uniform Gases*. Cambridge University Press, 1970.
6. U. Frisch, B. Hasslacher, and Y. Pomeau, *Phys. Rev. Lett.* **56**, 1505 (1986).
7. X. He, X. Shan, and G. Doolen, *Phys. Rev. Lett.* **57**, R13 (1998).
8. N.S. Martys and H. Chen, *Phys. Rev. E* **53**, 743 (1996).
9. Z. Guo, C. Zheng, and B. Shi, *Phys. Rev. E* **65**, art. no. 046308 (2002).



## Chapter 4

# Numerical Simulation of Mass Transport in Microfluidic Systems

This chapter is concerned with the application of the approach presented in Chapters 2 and 3 to the numerical simulation of mass transport in various microfluidic systems. It begins with the numerical simulation of EOF in straight cylindrical microchannels with a non-uniform distribution of the  $\zeta$ -potential (Section 4.1). Two basic patterns with axial and angular inhomogeneities in the  $\zeta$ -potential distribution (that can be employed to construct various, more complicated configurations) were investigated. Then, the EOF in a slit microchannel with heterogeneous and variable surface charge density at the channel walls is considered in order to investigate the effect of possible local surface charge modifications on the generated electroosmotic flow field (Section 4.2). Further, electrokinetic microfluidics in periodic colloidal systems is numerically simulated and the influence of a number of physical parameters, such as the electrical double layer thickness,  $\zeta$ -potential, applied electric field, as well as the computational grid resolution are studied (Section 4.3). The spatially definite and periodic structure of colloidal crystals allows to eliminate any stochastic effects that are peculiar to random packings and reduces considerably the computational expenses required to involve high numerical accuracy. After that, random packings of spherical particles (as model of porous media which are contained, e.g., in chromatographic columns or fixed bed reactors) are used for numerical simulations of hydraulic flow and hydrodynamic dispersion (Section 4.4). The existence of mesopores (of the size of a few tens of nanometers) inside the particles results in the necessity to involve different length-scales, and they extremely complicate the direct numerical simulation of transport phenomena in such structures. The semi-empirical approach presented in Section 4.4 allows to overcome this restriction and incorporate, in addition to the simulation of fluid dispersion in the interstitial space between particles caused both by convection and diffusion, the purely diffusive mass transport in intraparticle pore spaces. Finally, the problem of EOF through confined random packings of spherical particles is considered. This kind of random packings represents the fixed bed in actual

(electro)chromatographic columns with typically low column-to-particle diameter ratio and structural inhomogeneity which can significantly affect the efficiency of chromatographic separations due to the imposed complex hydrodynamics. In particular, it was shown that the more ordered structure of packing regions adjacent to the confining wall results in reduced hydrodynamical resistance, lower local tortuosity and, as a consequence, in an increased local velocity of the EOF.

#### **4.1. Coupled lattice-Boltzmann and finite-difference simulation of electroosmosis in microfluidic channels\***

In this section we are concerned with an extension of the lattice-Boltzmann method for numerical simulation of three-dimensional electroosmotic flow problems in porous media. The description is evaluated using simple geometries as those encountered in open-channel structures of microfluidic devices. In particular, we consider electroosmosis in straight cylindrical capillaries with (non)uniform zeta-potential distribution for ratios of the capillary inner radius to a thickness of the electrical double layer from 10 to 100. The general case of heterogeneous zeta-potential distributions at the inner surface of a capillary requires solution of the following coupled equations in three dimensions: Navier-Stokes equation for liquid flow, Poisson equation for electrical potential distribution, and Nernst-Planck equation for the distribution of ionic species. The hydrodynamic problem has been treated with high efficiency by code parallelization via the lattice-Boltzmann method. For validation the velocity fields were simulated in several microcapillary systems and good agreement with results predicted either theoretically or obtained by alternative numerical methods could be established. These results are also discussed with respect to the use of a slip boundary condition for the velocity field at the surface of the solid.

##### *4.1.1. Introduction*

Rapid recent developments in design, patterning, and utilization of microfluidic devices (valves, pumps, mixers, reactors, sensors and actuators, or three-dimensional channel networks) have found many applications in the devised bulk transport, separation, identification, synthesis, and manipulation of a wide range of chemical and biological species [1-6]. It is an advancement that becomes particularly important for the lab-on-a-chip concept [7] where transport processes, including the efficient mixing of micro- and nanoliter liquid

---

\*This section is based on a manuscript submitted to *Int. J. Num. Meth. Fluids*.



volumes, control and enhancement of reaction rates, heat and mass transfer, as well as the selectivity of chromatographic separations occur on much smaller time and length scale than traditional engineering technologies. With channel diameters from several to a few hundred micrometers (inherently placing microfluidics in the low-Reynolds number regime of hydrodynamics) and channel lengths approaching centimeter dimension, these systems permit a miniaturization of chemical processes and large-scale integration of engineering principles allowing fast response times at low operational costs [6].

A number of scientific issues have been addressed using microstructures to confine and also manipulate liquids including the flow through percolation structures or fundamental properties of liquids in small geometries where surface forces (surface tension, electrical effects, van der Waals interaction, surface roughness) are more important than usual. One of the challenges is to tailor these effects and produce functional devices.

Concerning the bulk transport of liquid through a microfluidic channel electroosmosis can offer distinct advantages over pressure-driven flow. Electroosmotic flow (EOF) is generated by interaction of an externally applied electrical field with that part of the electrolyte solution that has become locally charged at the interface to the stationary and oppositely charged solid surface of the confining porous medium [8, 9]. The extension into the bulk solution of the fluid-side domain of this electrical double layer can be as small as a few nanometers compared to a channel diameter of micrometer dimension, a fact that has some important consequences for the EOF dynamics under these conditions [10]. First, from a macroscopic point of view, bulk liquid moves as in plug flow, i.e., the velocity apparently slips at the wall, which is in contrast to the parabolic velocity profile typical for Poiseuille flow. Second, because the ratio of electroosmotic to hydraulic volumetric flow rates (at a fixed potential and pressure gradient) is inversely proportional to the squared channel diameter, the EOF becomes increasingly effective in liquid transport through the finer channels as their size is reduced. Thus the benefit of using EOF is that chemical and biological species may be easily transported in microfluidic devices over comparatively long distances with negligible mass transfer resistance. Hydrodynamic dispersion can then be limited almost to that by longitudinal diffusion alone which has been demonstrated experimentally [11, 12].

Stimulated by the enormous potential and accompanying need for a detailed characterization of electrokinetically driven mass transport in microfabricated (microchip) devices, numerical simulation of EOF in microfluidic channels has received increased attention over the past few years [13-28]. These investigations have revealed that in good

agreement with available experimental data the transport characteristics of flow in microchannels clearly depend on properties of the working fluid and the geometrical (and physico-chemical) parameters of the surface. For example, the work of Griffiths and Nilson [16] which is based on the direct solution of governing transport equations demonstrates that, over a wide range of conditions, the coefficient of longitudinal dispersion of a neutral nonreacting solute in EOF may be many orders of magnitude smaller than for the parabolic (or nearly so) velocity profile in pressure-driven flow. Ermakov et al. [15] used a 2D code to address electrokinetic species transport with respect to some basic microfluidic elements: They considered sample focusing in a channel cross and sample mixing at a T-junction. Patankar and Hu [14] carried out 3D flow field simulations to investigate the EOF behaviour at a channel cross, while Bianchi et al. [17] used their finite element-based simulations to describe the flow division at a decoupling T-junction, encountering combined electroosmotic and pressure-driven flows. Fu et al. [25] presented a physical model (and numerical method) for studying geometrical effects on the performance of electrophoresis microchips. Erickson and Li [27] utilized 3D finite element-based numerical simulations to resolve the influence of heterogeneous surface charge distributions on local flow circulation within the bulk liquid (under the aspect of enhanced sample mixing in a T-shaped micromixer).

While these numerical approaches give valuable insight into the flow behaviour in relatively simple channel geometries traditional computational fluid dynamics can face drawbacks if higher code flexibility is required, e.g., when dealing with a much more complicated pore space morphology (as in random particulate and fractured porous media), complex flows (multiphase or close to surfaces with a chemically and/or physically irregular pattern), or code parallelization.

Over the last decade lattice-Boltzmann (LB) methods [29-34] have achieved great success as alternative and efficient numerical schemes in the simulation of a variety of transport phenomena in porous media, with particular emphasis on the dynamics of pressure-driven liquid flow through complex porous media [34-50]. Besides their flexibility and accuracy in dealing with the confining geometry and actual boundary conditions LB methods are inherently parallel and, thus, they are ideally suited for high-performance parallel computing. In contrast to the conventional numerical schemes based on a discretization of macroscopic continuum equations, the LB method utilizes mesoscopic kinetic equations to recover the macroscopic Navier-Stokes equation for fluid motion in a long-time, large-scale limit [34]. Further, some early systematic problems of LB methods like the existence of velocity-dependent pressures and lack of a Galilean invariance are essentially resolved, and

algorithms have been simplified by the single relaxation time scheme of Bhatnagar et al. [51-53].

So far, only a few reports have been published in which LB simulations also touch electrokinetic phenomena (and electroosmotic flow, in particular). Quite recently, the LB method has been implemented to model high-Reynolds number pressure-driven flow in microfluidics, taking into account electroviscous effects that can become important due to the finite thickness of the electrical double layer compared to typical channel sizes [54], and a good agreement with published experimental data on the friction factor – Reynolds number relation in microchannels [55] was obtained. Further, in the work by Nie et al. [56] an extension of the LB method was proposed that is based on a density-dependent viscosity model and technique for imposing a slip-velocity at the wall. It was demonstrated that this approach can capture fundamental characteristics of microchannel flow such as non-linear pressure drop along the channel and the behaviour of mass flow rate for varying Kundsén numbers. Warren [57] analyzed the electrokinetic transport in a parallel-sided slit with a constant electrical charge (or potential) at this solid-liquid interface. The resulting one-dimensional problem was further restrained by assuming a quite thick electrical double layer compared to the width of the slit. While this work addresses special cases of significant double layer overlap encountered, for example, with ultrafine capillaries [58], in many situations of technological relevance, as for the electrokinetic species transport in (open-channel) microchip devices, the characteristic channel dimension normal to the local flow direction becomes (much) larger than the typical thickness of electrical double layers at the solid-liquid interface. It is this condition, in particular, that has to be satisfied in order to gain full potential of EOF (as compared to pressure-driven flow) with respect to the longitudinal dispersion and permeability [59]. Further many industrial and natural porous media are characterized by random or hierarchically-structured, but relatively broad pore size distributions, contrasting with the network of uniformly sized and shaped channels on microfluidic devices. Thus, in the general case, bulk transport involves conditions for which the ratio of a local pore radius to the electrical double layer thickness covers a spectrum from below unity up to hundreds [60]. The numerical approach that is presented in this work can cope with any geometry and possible surface heterogeneity, and it will be particularly efficient in resolving details of the flow field which govern mass transport and the dispersion in a transient, as well as long-time (asymptotic) regime.

### 4.1.2. Electrokinetics

#### Electroosmotic flow in a microfluidic channel

Figure 4.1 illustrates, at different length scales, the basic aspects of electroosmosis in a microfluidic channel with locally flat, smooth surface. When a dielectric solid (e.g., a fused-silica capillary) is contacted with a liquid electrolyte (e.g., a dilute aqueous NaCl solution) an electrical double layer (EDL) develops at the solid-liquid interface due to ionizable groups of the material (dissociation of silanol groups in the above example:  $\equiv\text{Si}-\text{OH} + \text{H}_2\text{O} \leftrightarrow \equiv\text{Si}-\text{O}^- + \text{H}_3\text{O}^+$ ) or by ions adsorbing on its surface. The resulting negative charge density of the capillary (channel) inner wall affects the distribution of hydrated sodium (counter)ions in the solution: In immediate proximity to the surface there exists a layer of ions which are relatively strongly fixed by electrostatic forces. It forms the inner or compact part of the fluid-side domain of the EDL and its typical thickness is of the order of only one ion diameter (about 0.5 nm). The outer Helmholtz plane (OHP, Fig. 4.1c) separates inner and diffusive layers which, together, constitute the EDL. While the ionic species in the diffusive layer undergo

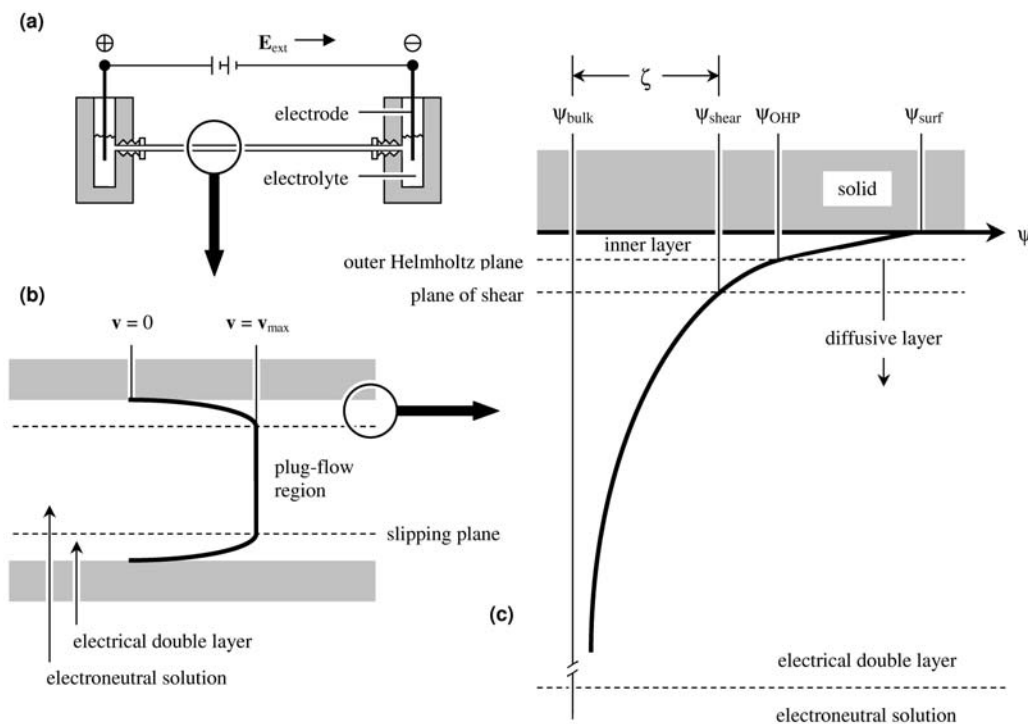


**Figure 4.1.** Illustration of some features of electrokinetically-driven flow of liquid (electroosmosis) through a straight cylindrical capillary ( $\zeta < 0$ ). (a) Experimental set-up, (b) pore-scale EOF velocity profile, and (c) distribution of electrical potential in the EDL.

Brownian motion, they are also influenced by the local electrostatic potential. At equilibrium their accumulation in this region can be described by the Boltzmann equation. The spatial dimension of the diffusive layer is typically between a few and hundred nanometres.

EOF sets in when an external electrical field ( $\mathbf{E}_{\text{ext}} = -\nabla\phi$ ) is applied. It interacts with the EDL field to create an electrokinetic body force on the liquid. Consequently, the bulk of liquid is driven by a viscous drag via the shear stresses concentrated in the relatively thin EDL (compared to a capillary radius  $r_c$  of micrometer dimension). The potential ( $\psi$ ) at the so-called shear plane separating the mobile and immobile phases is the electrokinetic (or  $\zeta$ ) potential. For the case considered here (smooth surface, simple ions)  $\zeta$  must be close to, if not coincident with the diffusive double layer potential  $\psi_{\text{OHP}}$  (cf. Fig.4.1c). The fluid velocity rises from zero at the shear plane to a limiting value  $\mathbf{v}_{\text{max}}$  beyond the EDL where, from a macroscopic point of view, the liquid seems to slip past the surface (Fig. 4.1b)

$$\mathbf{v}_{\text{max}} = \mu_{\text{eo}} \mathbf{E}_{\text{ext}} = -\varepsilon_0 \varepsilon_r \left( \frac{\zeta}{\eta} \right) \mathbf{E}_{\text{ext}}. \quad (4.1)$$

$\mu_{\text{eo}}$  denotes the electroosmotic mobility and  $\eta$  is the dynamic viscosity of the fluid.  $\varepsilon_0$  is the permittivity of vacuum and  $\varepsilon_r$  the relative permittivity of the electrolyte solution. The minus sign in Eq. 4.1 means that  $\mathbf{v}_{\text{max}}$  and  $\mathbf{E}_{\text{ext}}$  are in the same direction when  $\zeta$  is negative. Without any externally applied pressure forces and uniform distribution of  $\zeta$  along the channel wall the liquid moves as in plug-flow as the gradient in  $\psi$  beyond the EDL is negligible. The thickness of the EDL is characterized by

$$\lambda_D = \left( \frac{\varepsilon_0 \varepsilon_r RT}{F^2 \sum_i z_i^2 c_{i,\infty}} \right)^{1/2}, \quad (4.2)$$

where  $R$  is the gas constant,  $T$  the absolute temperature and  $F$  Faraday's constant,  $z_i$  is the valency of ionic species  $i$  and  $c_{i,\infty}$  its molar concentration in the electroneutral solution.  $\lambda_D$  is the Debye screening length and about 10 nm for a  $10^{-3}$  M 1:1 aqueous electrolyte solution. In this case the EDL is much smaller than the radius of micrometer channels ( $r_c/\lambda_D > 100$ ) and the volumetric EOF rate is approximately given by  $Q = v_{\text{max}}A$  (where  $A$  is the cross-sectional area of a channel). However, as the channel diameter approaches submicrometer dimension and/or as  $\lambda_D$  increases the EDL cannot be considered as thin any longer (e.g.,  $r_c/\lambda_D \approx 10$ ) and

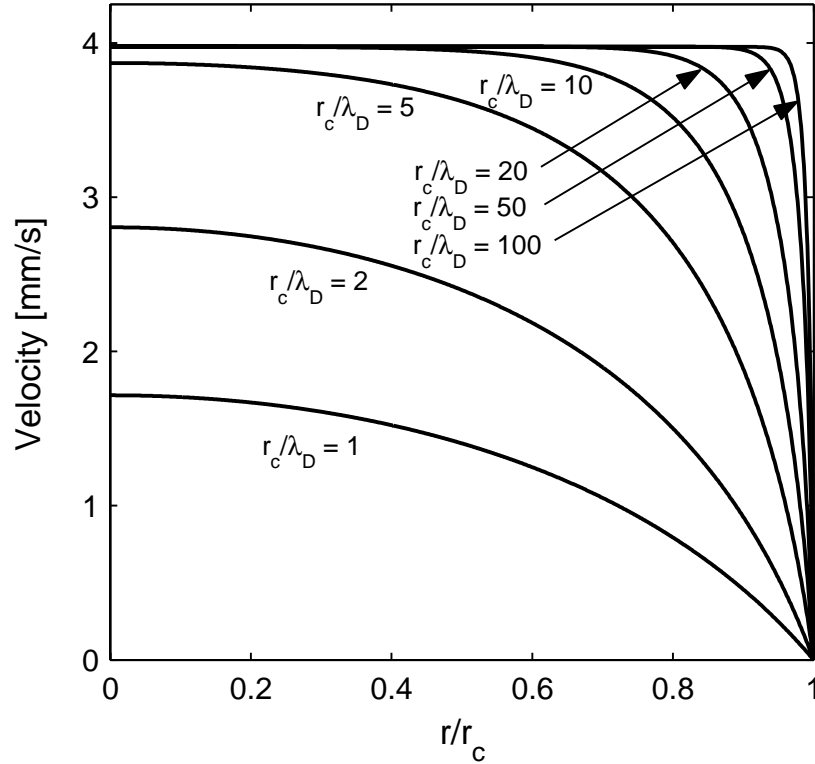


**Figure 4.2.** Velocity profiles of EOF in an open-straight, cylindrical capillary for different values of  $r_c/\lambda_D$  obtained by solution of the momentum balance equation [61]. Externally applied electrical field  $E_{\text{ext}} = 5 \times 10^4 \text{ V}\cdot\text{m}^{-1}$ ,  $\zeta = -0.1 \text{ V}$ ,  $\epsilon_r = 80$ , the liquid density and viscosity are  $10^3 \text{ kg}\cdot\text{m}^{-3}$  and  $0.89 \times 10^{-4} \text{ kg}\cdot\text{m}^{-1}\cdot\text{s}^{-1}$ , respectively (at  $T = 298.15 \text{ K}$ ). The Debye screening length ( $\lambda_D$ ) is 10 nm.

the plug-like velocity profile deteriorates towards a parabola, as is known for Poiseuille flow ( $r_c/\lambda_D = 2$ ), with an accompanying increase in hydrodynamic dispersion evidenced by Fig. 4.2 [10, 61].

#### General mathematical formulation

The velocity field of an incompressible Newtonian electrolyte solution in low-Reynolds number flow through a microfluidic channel is governed by the Navier-Stokes equation

$$\rho_f \left( \frac{\partial \mathbf{v}}{\partial t} + (\mathbf{v} \cdot \nabla) \mathbf{v} \right) = -\nabla p + \eta \nabla^2 \mathbf{v} + \mathbf{f}, \quad (4.3)$$

where  $\rho_f$  is the density of the fluid,  $\mathbf{v}$  represents the divergence-free velocity field ( $\nabla \cdot \mathbf{v} = 0$ ), and  $p$  denotes hydrostatic pressure. The body force  $\mathbf{f}$  is related to the volume density of charge  $\rho_q$  and the local electrical field ( $\mathbf{E} = -\nabla\Phi$ ) by

$$\mathbf{f} = \rho_q \mathbf{E} = -q_e \nabla \Phi \sum_{i=1}^N z_i n_i, \quad \text{for } i = 1, \dots, N, \quad (4.4)$$

where  $q_e$  stands for the elementary charge,  $n_i$  is the number concentration of ionic species  $i$  in the  $N$ -component electrolyte solution, and  $\Phi$  denotes the local electrostatic potential which is governed by the Poisson equation

$$\nabla^2 \Phi = -\frac{\rho_q}{\epsilon_0 \epsilon_r}. \quad (4.5)$$

The flux density  $\mathbf{j}_i$  (the number of ions per unit area passing through the surface of a volume element) is related to the local fluid velocity and gradients in ion density and electrical potential by the Nernst-Planck equation

$$\mathbf{j}_i = \left( \mathbf{v} - \frac{q_e z_i D_i \nabla \Phi}{k_B T} \right) n_i - D_i \nabla n_i, \quad (4.6)$$

where  $D_i$  is the mass diffusion coefficient and  $k_B$  is the Boltzmann constant. Each ionic species satisfies the following conservation

$$\frac{\partial n_i}{\partial t} + \nabla \cdot \mathbf{j}_i = 0. \quad (4.7)$$

Together with appropriate initial and boundary conditions Eqs. 4.3-4.7 describe the mass transport in systems with arbitrary geometry, distribution (and magnitude) of  $\zeta$ , and aspect ratio. It is important to note that we consider here (cf. Eqs. 4.4-4.6), without further simplification, the local electrostatic potential in the channel which, in general, includes contributions from both the EDL and  $\mathbf{E}_{\text{ext}}$ . Further, the presented description does not rely on the Boltzmann distribution for electrical charges in the diffusive part of the EDL applicable only at thermodynamic equilibrium. It would assume that this distribution remains undisturbed by external convective influences which is justified only under certain limiting

conditions, e.g., at a low Peclet number in channels of arbitrary geometry and for a uniform distribution of  $\zeta$  [13].

In this work we consider fully-developed, steady, isothermal EOF in the microfluidic channel. It eliminates the time derivatives in Eqs. 4.3 and 4.7, as well as the need for initial conditions. Thus, we remain concerned with the following set of coupled equations.

$$\rho_f (\mathbf{v} \cdot \nabla) \mathbf{v} = -\nabla p + \eta \nabla^2 \mathbf{v} - q_e \nabla \Phi \sum_{i=1}^N z_i n_i \quad (4.8a)$$

$$\nabla \cdot \mathbf{v} = 0 \quad (4.8b)$$

$$\nabla^2 \Phi = -q_e \sum_{i=1}^N z_i n_i / \epsilon_0 \epsilon_r \quad (4.8c)$$

$$\mathbf{v} \nabla n_i - D_i \nabla^2 n_i - \frac{q_e z_i D_i}{k_B T} \nabla \cdot (n_i \nabla \Phi) = 0 \quad (4.8d)$$

### Boundary conditions

Because the length of a microfluidic channel is large compared to heterogeneities in the fluid flow field and species transport on any length (and associated time) scale we assume longitudinal spatial periodicity [62]. Thus, our description reduces to that of a representative unit (Fig. 4.3a) with periodic (outer) boundary conditions

$$[[\Phi]] = C, [[n_i]] = 0, [[\mathbf{v}]] = 0, \quad (4.9)$$

where  $C$  is a constant related to the conditions of an experiment (including pH, the electrolyte concentration,  $\mathbf{E}_{\text{ext}}$ , surface adsorption, or the temperature) and  $[[\dots]]$  denotes the difference between values of a function at opposite points lying on the corresponding unit boundaries.

The outer boundary conditions have to be complemented by inner boundary conditions which define the values of the electrical potential (or charge), the flow velocity and species number concentrations at the solid-liquid interface. The common no-slip and normal-zero-flux conditions are recognized at this interface for the fluid flow velocity and number concentrations, respectively



$$\mathbf{v} = 0, \mathbf{v} \cdot \mathbf{j}_i = 0, \quad (4.10a, b)$$

where  $\mathbf{v}$  is the outer normal to the solid-liquid interface. In turn, an electrical boundary condition can be represented by either the surface charge density or  $\zeta$ -potential. Since these characteristics, in particular, depend on both the nature of contacting media and the local environment, e.g., the interfacial space morphology or the local pH, they can be considered, in general, as spatially variable quantities. Thus, the electrical boundary conditions at the solid-liquid interface can be imposed in two alternative ways: by given surface charge density or  $\zeta$ -potential distributions, respectively

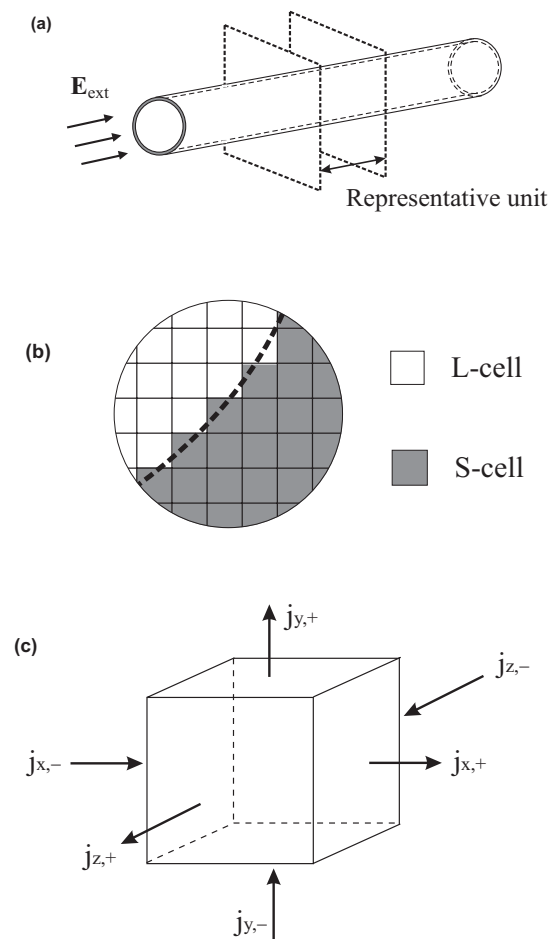


**Figure 4.3.** Discretization and approximation of the solution domain. (a) Capillary scale. Spatial periodicity reduces the description to that of a representative unit with periodic boundary conditions. (b) Solid-liquid interface. The solution domain is represented by a set of uniform cubic cells. (c) Single L-cell. Entry and exit flux density components.

$$\mathbf{v} \cdot \nabla \Phi = -\frac{\sigma(\mathbf{r})}{\varepsilon_0 \varepsilon_r} \quad \text{or} \quad \Phi = \zeta(\mathbf{r}). \quad (4.11a, b)$$

The former equation corresponds to the Neumann-type, the latter to the Dirichlet-type boundary condition.

This presentation of inner boundary conditions assumes that the boundary values of all quantities (the flow velocity, species flux, surface charge density, and  $\zeta$ -potential) are related to the same location. In fact, while the no-slip and normal-zero-flux conditions, as well as the given surface charge density are recognized directly at the solid-liquid interface, the  $\zeta$ -potential is defined with respect to the shear plane (cf. Fig. 4.1). However, since this plane is located in immediate proximity ( $\approx 0.5$  nm) to the solid-liquid interface, it is assumed that these surfaces coincide.

#### 4.1.3. Computational methods

##### General scheme

To solve the system of time-independent partial differential equations, Eqs. 4.8a-4.8d, subject to inner and outer boundary conditions, Eqs. 4.9-4.11, an iterative scheme (Fig. 4.4) was implemented. At each iteration first the coupled Nernst-Planck and Poisson equations, Eq. 4.8d and Eq. 4.8c, were solved numerically. Then, the Navier-Stokes equation, Eq. 4.8a, together with the continuity equation, Eq. 4.8b, were solved. The iterative solution had continued until convergence of the flow field was reached. As initial guess zero flow field, as well as bulk number concentrations and the electrical potential distribution caused by the applied field were used. This contribution to the local electrical potential is assumed to be point-wise constant during iterations. Thus, the numerical scheme requires the solution of the Poisson, Nernst-Planck, and Navier-Stokes equations (where the last problem is, by far, the more difficult computational task). While traditional finite-difference methods were used to resolve the first two problems, the lattice-Boltzmann method has been applied for solution of the Navier-Stokes problem.

##### Geometry and discretization of the solution domain

A uniform mesh has been utilized for numerical solution of all of the above-mentioned problems. Thus, the solution domain can be represented by a set of equal cubic cells of size  $\Delta h$  (Fig. 4.3b). Cells were divided into two subsets, i.e., cells having their geometrical centre in the liquid phase (L-cells) or in the solid phase (S-cells). During a simulation the electrical

potential, charge number concentration, and fluid velocity are determined at the centres of only the L-cells. S-cells adjacent to L-cells are considered as interface cells and the actual values of physical quantities at their centres are used as boundary values.

Numerical solution of the Poisson-Nernst-Planck problem

The finite-difference scheme for solution of the Nernst-Planck equation is based on the total flux density in an L-cell. For steady-state the net flux is zero. This situation can be represented by entry and exit components on each of the six cell surfaces (Fig. 4.3c)

$$j_{k,l,m}^{x,+} + j_{k,l,m}^{x,-} + j_{k,l,m}^{y,+} + j_{k,l,m}^{y,-} + j_{k,l,m}^{z,+} + j_{k,l,m}^{z,-} = 0, \quad (4.12)$$

where  $k$ ,  $l$ , and  $m$  define the discrete coordinates of a cell. If an L-cell is not lying adjacent to the interface each of the flux density components is expressed in terms of the flow velocity, concentration, and electrical potential at the centre of a given and neighbouring points. For a particular species, for example, we have

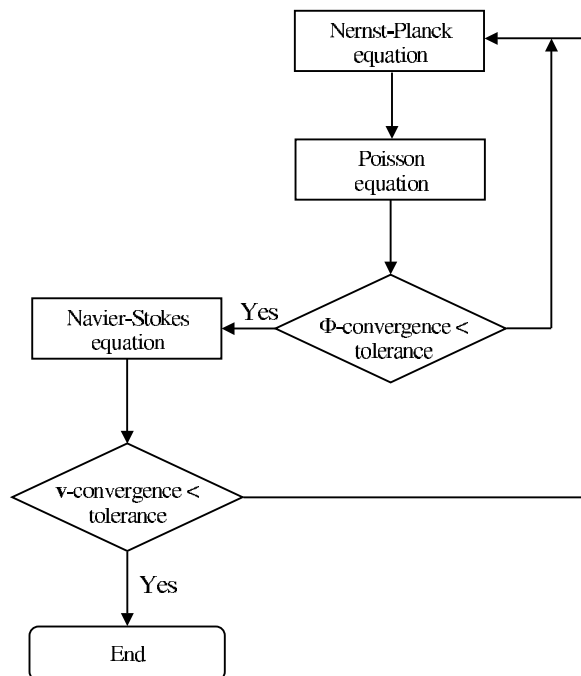


**Figure 4.4.** Flow-chart of the computational scheme employed for our PNP-LB (Poisson-Nernst-Planck coupled with lattice-Boltzmann) simulations.

$$\begin{aligned}
 j_{k,l,m}^{x,+} = & \frac{v_{k+1,l,m}^x + v_{k,l,m}^x}{2} \frac{n_{k+1,l,m} + n_{k,l,m}}{2} \\
 & - D \frac{n_{k+1,l,m} - n_{k,l,m}}{h} \\
 & - \frac{q_e z D}{k_B T} \frac{n_{k+1,l,m} + n_{k,l,m}}{2} \frac{\Phi_{k+1,l,m} - \Phi_{k,l,m}}{h}
 \end{aligned} \tag{4.13}$$

If a given L-cell is adjacent to the interface and the normal-zero-flux boundary conditions are applied, the corresponding term in Eq. 4.12 is eliminated. By assuming that interface and boundary values lie on the border between L- and S-cells the distance  $h/2$  (instead of  $h$ ) should be selected. This is consistent with the location of the no-slip wall in LB simulations based on the bounce-back boundary condition [63].

By using similar expressions for the other flux components, substituting into Eq. 4.13 and solving the resulting equation for  $n_{k,l,m}$  one can obtain an explicit expression for calculation of its updated value. It is determined by the concentration values from a previous iteration, as well as with the flow velocity and electrical potential values in a given and neighbouring cells. An SOR scheme was used to get more rapid convergence

$$\hat{n}_{k,l,m} = \omega n_{k,l,m} + (1 - \omega) \tilde{n}_{k,l,m}, \tag{4.14}$$

where  $\hat{n}_{k,l,m}$  is the updated number concentration at the current iteration,  $\tilde{n}_{k,l,m}$  is the number concentration from a previous iteration, and  $\omega$  is the relaxation parameter. Then, updated number concentration values for each species in all cells are used for solution of the Poisson equation. Its finite-difference representation is

$$\begin{aligned}
 -\frac{\sum n_{k,l,m} z q_e}{\epsilon_0 \epsilon_r} = & \frac{2}{h_{k+1/2} + h_{k-1/2}} \left( \frac{\Phi_{k+1,l,m} - \Phi_{k,l,m}}{h_{k+1/2}} - \frac{\Phi_{k,l,m} - \Phi_{k-1,l,m}}{h_{k-1/2}} \right) \\
 & + \frac{2}{h_{l+1/2} + h_{l-1/2}} \left( \frac{\Phi_{k,l+1,m} - \Phi_{k,l,m}}{h_{l+1/2}} - \frac{\Phi_{k,l,m} - \Phi_{k,l-1,m}}{h_{l-1/2}} \right), \\
 & + \frac{2}{h_{m+1/2} + h_{m-1/2}} \left( \frac{\Phi_{k,l,m+1} - \Phi_{k,l,m}}{h_{m+1/2}} - \frac{\Phi_{k,l,m} - \Phi_{k,l,m-1}}{h_{m-1/2}} \right)
 \end{aligned} \tag{4.15}$$

where, for example,  $h_{k+1/2}$  is the distance between the centers of cells  $(k+1,l,m)$  and  $(k,l,m)$ , and a summation should be performed over all ionic species. As for the Nernst-Planck equation, this expression needs to be modified if the cell is adjacent to the interface by

replacing either the corresponding distance  $h$  by  $h/2$  (Dirichlet boundary condition) or the corresponding potential difference by  $2\sigma/(h\epsilon_0\epsilon_r)$  (Neumann boundary condition). By applying the traditional Gauss-Seidel iterative procedure Eq. 4.15 allows to obtain an explicit expression for determination of the updated value of the electrical potential which, in the case of the Dirichlet boundary condition, can be written as

$$\begin{aligned} \hat{\Phi}_{k,l,m} = & \left( \frac{1}{h_{k+1/2}h_{k-1/2}} + \frac{1}{h_{l+1/2}h_{l-1/2}} + \frac{1}{h_{m+1/2}h_{m-1/2}} \right)^{-1} \\ & \times \left( \frac{\sum n_{k,l,m} z q_e}{2\epsilon_0\epsilon_r} + \frac{h_{k-1/2}\check{\Phi}_{k+1,l,m} + h_{k+1/2}\hat{\Phi}_{k-1,l,m}}{h_{k+1/2}h_{k-1/2}(h_{k+1/2} + h_{k-1/2})} \right. \\ & \left. + \frac{h_{l-1/2}\check{\Phi}_{k,l+1,m} + h_{l+1/2}\hat{\Phi}_{k,l-1,m}}{h_{l+1/2}h_{l-1/2}(h_{l+1/2} + h_{l-1/2})} + \frac{h_{m-1/2}\check{\Phi}_{k,l,m+1} + h_{m+1/2}\hat{\Phi}_{k,l,m-1}}{h_{m+1/2}h_{m-1/2}(h_{m+1/2} + h_{m-1/2})} \right) \end{aligned} \quad (4.16)$$

Calculations of number concentration and electrical potential stop when the convergence rate

$$\gamma_{\text{PNP}} = \sqrt{\frac{\sum_{k,l,m} (\hat{\Phi}_{k,l,m} - \check{\Phi}_{k,l,m})^2}{\sum_{k,l,m} \check{\Phi}_{k,l,m}^2}} \quad (4.17)$$

becomes less than the predefined value  $\delta_{\text{PNP}}$  (PNP  $\equiv$  Poisson-Nernst-Planck), which is typically set to  $10^{-6}$ .

### The lattice-Boltzmann algorithm

The electrolyte solution as a statistical system can be described in terms of a distribution function  $\mathcal{F}(\mathbf{r}, \mathbf{u}, t)$  defined such that  $\mathcal{F}(\mathbf{r}, \mathbf{u}, t) d\mathbf{r} d\mathbf{u}$  provides the number of fluid molecules which, at time  $t$ , are located between  $\mathbf{r}$  and  $(\mathbf{r} + d\mathbf{r})$  and have velocities in the range from  $\mathbf{u}$  to  $(\mathbf{u} + d\mathbf{u})$ . Macroscopic quantities like fluid density  $\rho_f$  and velocity  $\mathbf{v}$  can be determined from momentum integration of this distribution function

$$\rho_f(\mathbf{r}, t) = \int M_m \mathcal{F}(\mathbf{r}, \mathbf{u}, t) d\mathbf{u}, \text{ and} \quad (4.18)$$

$$\mathbf{v}(\mathbf{r}, t) = \frac{1}{\rho_f(\mathbf{r}, t)} \int M_m \mathbf{u} \mathcal{F}(\mathbf{r}, \mathbf{u}, t) d\mathbf{u}, \quad (4.19)$$

where  $M_m$  denotes molecular mass. The evolution of the distribution function can be described by the following equation

$$\mathcal{F}\left(\mathbf{r} + \mathbf{u}dt, \mathbf{u} + \frac{\mathbf{F}}{M_m} dt, t + dt\right) d\mathbf{r}d\mathbf{u} = \mathcal{F}(\mathbf{r}, \mathbf{c}, t) + \Omega_c(\mathcal{F}) d\mathbf{r}d\mathbf{u}dt, \quad (4.20)$$

where  $\mathbf{F}$  is the acting external force and  $\Omega_c$  denotes the collision operator. It is well known that macroscopic properties are not directly dependent on the details of microscopic behaviour, but are mainly defined by the interactions between molecules expressed, for example, by an appropriate collision operator. Therefore, a transition toward a simplified dynamics with discrete space, time, and molecular velocities becomes feasible. The discrete analogy of Eq. 4.20 is

$$\mathcal{F}_\alpha(\mathbf{r} + \mathbf{e}_\alpha \Delta t, t + \Delta t) = \mathcal{F}_\alpha(\mathbf{r}, t) + \Omega_\alpha(\mathcal{F}_\alpha) + \Delta t \mathcal{F}_\alpha, \quad (4.21)$$

where  $\mathcal{F}_\alpha$  is the distribution function for the  $\alpha$ -th discrete velocity  $\mathbf{e}_\alpha$  at position  $\mathbf{r}$  and time  $t$ , and  $\Delta t$  is the time step. In this work we are concerned with a modification of the LB approach, the so-called lattice-BGK (Bhatnagar-Gross-Krook) model [34, 52], described by the discrete Boltzmann equation with a single-time relaxation collision operator

$$\mathcal{F}_\alpha(\mathbf{r} + \mathbf{e}_\alpha \Delta t, t + \Delta t) = \mathcal{F}_\alpha(\mathbf{r}, t) + \frac{1}{\tau} \left[ \mathcal{F}_\alpha^{\text{eq}}(\mathbf{r}, t) - \mathcal{F}_\alpha(\mathbf{r}, t) + \Delta t \mathbf{F}_\alpha \right], \quad (4.22)$$

where  $\mathcal{F}_\alpha^{\text{eq}}$  represents the equilibrium distribution function and  $\tau$  is a dimensionless relaxation time. For the  $D_3Q_{19}$  lattice-BGK model [32]  $\mathcal{F}_\alpha^{\text{eq}}$  can be expressed by

$$\mathcal{F}_\alpha^{\text{eq}} = \rho_f w_\alpha \left[ 1 + \frac{3}{c_s^2} \mathbf{e}_\alpha \cdot \mathbf{v} + \frac{9}{2c_s^4} (\mathbf{e}_\alpha \cdot \mathbf{v})^2 - \frac{3}{2c_s^2} \mathbf{v} \cdot \mathbf{v} \right], \quad (4.23)$$

where  $c_s$  is the speed of sound and  $w_\alpha$  is a weighting factor depending on the length of the vector  $\mathbf{e}_\alpha$  given by [52]

$$w_\alpha = \begin{cases} 1/3, & \alpha = 0 \text{ (rest particle)}, \\ 1/18, & \alpha = 1, 2, \dots, 6 \text{ (nearest neighbours)}, \\ 1/36, & \alpha = 7, 8, \dots, 18 \text{ (next - nearest neighbours)}. \end{cases} \quad (4.24)$$

The incorporation of a body force term caused by the interaction of the EDL field with the externally applied electrical field into the discrete Boltzmann equation has been performed using the method described by Guo et al. [64]

$$F_\alpha = \left(1 - \frac{1}{2\tau}\right) w_\alpha \left[ \frac{\mathbf{e}_\alpha - \mathbf{v}}{c_s^2} + \frac{(\mathbf{e}_\alpha \cdot \mathbf{v})}{c_s^4} \mathbf{e}_\alpha \right] \cdot \mathbf{F}. \quad (4.25)$$

After each iteration the divergence rate

$$\gamma_{\text{NS}} = \sqrt{\frac{\sum_{k,l,m} (\tilde{v}_{k,l,m} - \check{v}_{k,l,m})^2}{\sum_{k,l,m} \check{v}_{k,l,m}^2}} \quad (4.26)$$

is calculated and compared with a predefined value of  $\delta_{\text{NS}}$  (NS  $\equiv$  Navier-Stokes). The simulation stops when the condition  $\gamma_{\text{NS}} < \delta_{\text{NS}}$  (its typical value was  $10^{-4}$ ) is satisfied. It should be noted that the overwhelming majority of real electrokinetic systems operates in the low-Mach number limit which is a necessary condition for application of the lattice-Boltzmann method. Typical EOF velocities are of the order of a few millimetres per second which is significantly less than the speed of sound in liquid media.

#### 4.1.4. Results of simulations

Although the presented model is capable of dealing with both arbitrary zeta-potential distribution and geometrical configurations of the solid-liquid interface, we start from the EOF simulation in relatively simple systems for which either an analytical solution to the problem exists or results of other numerical simulations are available for comparison. Quantitative analysis of the computed fields of a physical quantity  $\Theta$  (e.g., the species number concentration or flow velocity components) is based on the global relative error  $\gamma$  defined with respect to some appropriate reference value

$$\gamma = \frac{\sqrt{\sum (\Theta - \Theta_{\text{ref}})^2}}{\sqrt{\sum \Theta_{\text{ref}}^2}}. \quad (4.27)$$

In particular, for the lattice-Boltzmann EOF velocity field in a homogeneous capillary, reference values may be obtained by numerical solution of the momentum balance equation using the Runge-Kutta method. To test the adequacy of the model for simulating electrical charge distribution in the diffusive part of the EDL (cf. Fig. 4.1c) we begin with an isolated, homogeneous solid-liquid interface for which the typical dimension of surface roughness is smaller than the EDL thickness, and simulate the ionic number concentration in the electrolyte in contact with the surface by solving the Poisson and Nernst-Planck problems. At equilibrium, without any concentration gradients and in the absence of an externally applied field, the electrical potential distribution can be obtained from the Poisson-Boltzmann equation

$$\nabla^2 \Psi = -\frac{q_e}{\varepsilon_0 \varepsilon_r} \sum_{i=1}^N z_i n_{i,\infty} \exp\left(-\frac{q_e z_i \Psi}{k_B T}\right), \quad (4.28)$$

where the local concentration is determined by the Boltzmann distribution

$$n_i = n_{i,\infty} \exp\left(-\frac{q_e z_i \Psi}{k_B T}\right). \quad (4.29)$$

The analytical solution of Eq. 4.28 (this equation presents the starting point of the Gouy-Chapman description [65] of a diffusive electrical double layer) for a charged flat surface, symmetrical 1:1 electrolyte such as NaCl ( $z_1 = -z_2 = z$ ) and an arbitrary magnitude, but uniform distribution of the zeta-potential is [66]



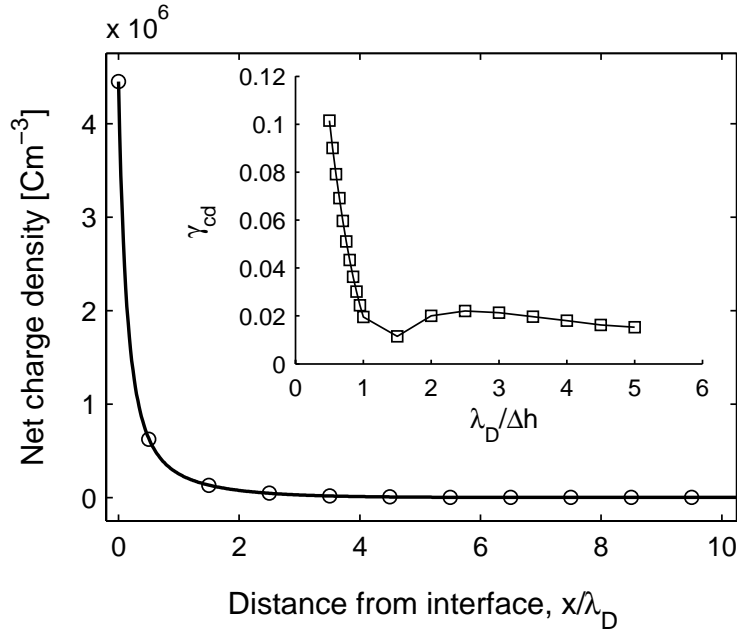


**Figure 4.5.** Distribution of net electrical charge in the EDL at a flat solid-liquid interface (open circles are results of the numerical solution, solid line: analytical solution) and dependence of the global relative error ( $\gamma_{cd}$ ) on grid resolution with respect to the double layer thickness (inset).

$$\psi(x) = \frac{2k_B T}{q_e z} \ln \left[ \frac{1 + e^{-x/\lambda_D} \tanh\left(\frac{q_e z \zeta}{4k_B T}\right)}{1 - e^{-x/\lambda_D} \tanh\left(\frac{q_e z \zeta}{4k_B T}\right)} \right], \quad (4.30)$$

where  $x$  gives the distance from the surface. For values of  $\zeta$  low enough (below about 25 mV) Equation (4.30) reduces to the so-called Debye-Hückel equation,  $\psi(x) = \zeta e^{-x/\lambda_D}$ . Results for the distribution of net electrical charge density based on the analytical solution (Eqs. 4.29 and 4.30) and the numerical treatment are shown in Fig. 4.5. Because  $\lambda_D$  appears as characteristic decay length for the potential, we analyzed the global relative error in dependence of the grid resolution with respect to  $\lambda_D$  (see inset). As electrolyte we considered an aqueous solution of NaCl at 298.15 K with a concentration ( $9.43 \times 10^{-4}$  M) adjusted such that  $\lambda_D$  is 10 nm (Eq. 4.2), while the surface is characterized by  $\zeta = -100$  mV. The main conclusion to be drawn from Fig. 4.5 is that the net charge density (cd) away from a charged surface can be computed with global relative errors ( $\gamma_{cd}$ ) better than 2% for a grid resolution  $\lambda_D/\Delta x$  of 1 and higher ( $\gamma_{cd} = 0.59\%$  for  $\lambda_D/\Delta x = 30$ ) by using the Poisson-Nernst-Planck solver described above. Further,

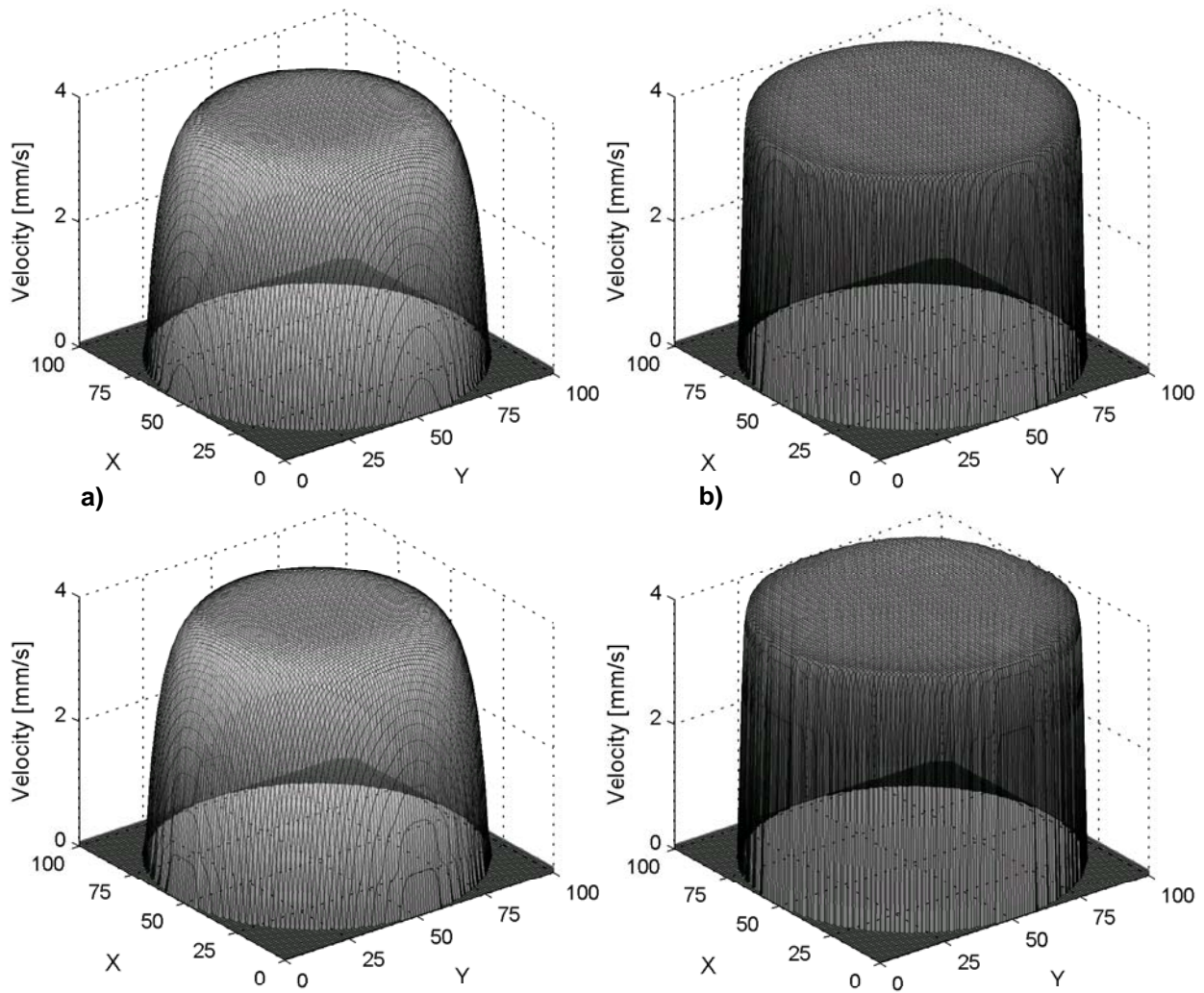


**Figure 4.6.** The EOF velocity field in an open-straight, cylindrical capillary with homogeneous and smooth surface: Solution of the momentum balance equation (top) vs. the PNP-LB approach (bottom) for a)  $r_c/\lambda_D = 10$  and b)  $r_c/\lambda_D = 100$ . The same conditions as in Fig. 2 have been used here.

it is evident that after a distance of about  $5\lambda_D$  from the surface the solution is practically electroneutral. Recalling that this distance is about 50 nm under the present set of conditions, it is only a thin liquid layer close to the interface that becomes locally charged, in general, when considering electrolytes confined by pores of micrometer dimension.

As the next step the EOF in a straight, homogeneous, cylindrical capillary was simulated. The spatial homogeneity of this system alleviates the use of an iterative procedure for obtaining a steady-state flow velocity field. Ionic number concentrations are not disturbed by the forced convection. Thus, the Poisson-Nernst-Planck solver and LB-code are run only once. Because there is no general analytical solution available for the EOF problem in a

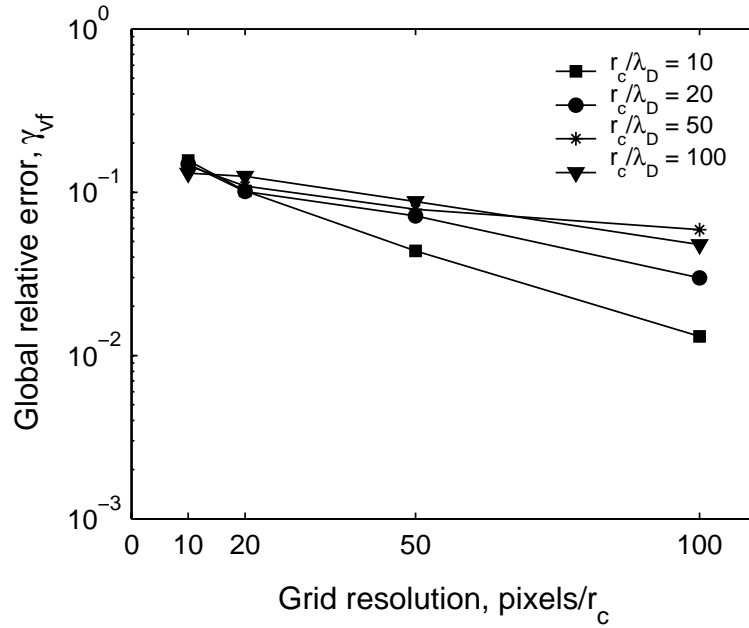


**Figure 4.7.** Global relative error of a simulated velocity field ( $\gamma_{vf}$ ) relative to the solution of the momentum balance equation: Accuracy of the PNP-LB approach depending on spatial resolution with respect to the capillary radius at various aspect ratios ( $r_c/\lambda_D$ ).

cylindrical capillary, the simulated velocity field was compared with another one obtained by numerical solution of the one-dimensional momentum balance equation [61]

$$\frac{d^2 v_x}{dr^2} + \frac{1}{r} \frac{dv_x}{dr} = \frac{2E_{\text{ext}} q_e n_\infty}{\eta_f} \sinh\left(\frac{q_e \Psi}{k_B T}\right). \quad (4.31)$$

The solution of this equation provides the radial distribution of the axial velocity component of EOF in the cylindrical capillary. Equation 4.31 was solved with a very fine resolution ( $2 \times 10^5$  points per channel diameter). Further, the use of different capillary radii allowed to realize aspect ratios  $r_c/\lambda_D$  from 10 to 100. Fig. 4.6 compares the velocity profiles obtained via both procedures. As was already emanating from Fig. 4.5, an applied electrical field will be interacting with the electrolyte solution only in the EDL where the liquid phase has acquired a net charge. Thus, the driving force for EOF is not constant over the capillary diameter: it dominates in vicinity of the capillary wall, but soon becomes zero in the central region of the capillary lumen. There, motion of bulk liquid is caused by a viscous drag force, leading to the plug-like velocity profile beyond the slipping plane (Fig. 4.1b). The dependence of the global relative error  $\gamma_{vf}$  of the axial component in a velocity field (vf) on spatial resolution (with respect to the capillary inner diameter  $r_c$ ) for different aspect ratios is

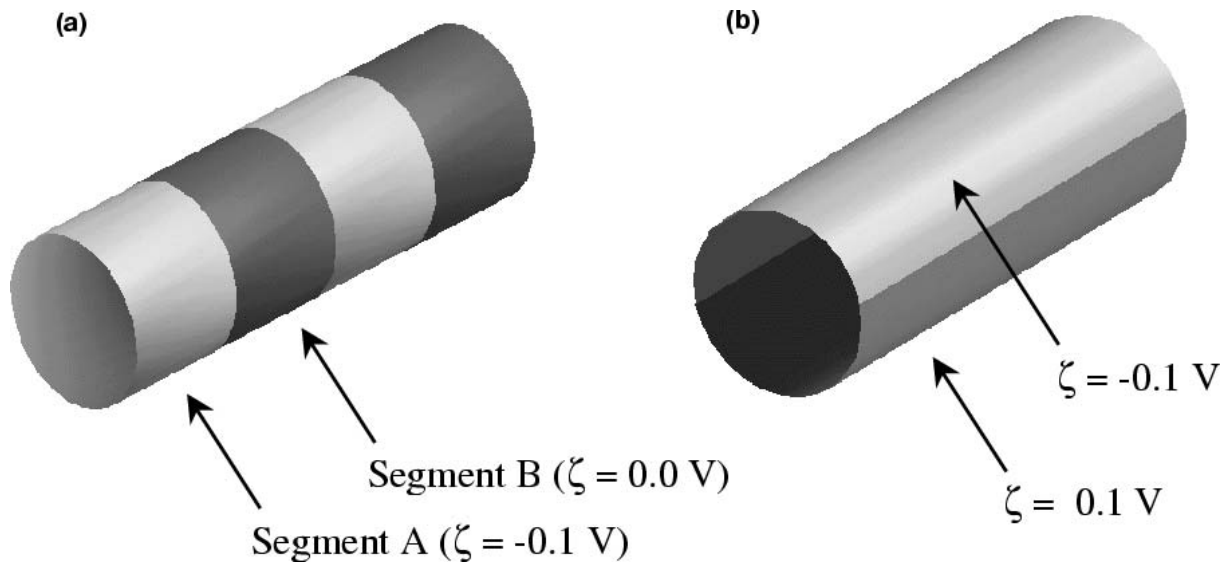


**Figure 4.8.** Inhomogeneous charge distributions (discrete patterns) at the inner wall of a cylindrical capillary. a) Surface charge pattern 1 (P1): Step changes of  $\zeta$  in the axial direction, angular uniformity. b) P2: Step changes of  $\zeta$  in the angular direction, axial uniformity.

demonstrated in Fig. 4.7. The error related to spatial resolution manifests itself in an inaccuracy of both the calculated electrical charge distribution and velocity field. Grid refinement can achieve higher accuracy, e.g., the use of 100 grid points over one capillary diameter results in  $\gamma_{vf}$  of less than 6% for all aspect ratios. On the other hand, computation time grows with the third power of spatial resolution.

The complete simulation of EOF in a cylindrical capillary (using  $r_0/h = 50$ ) took about 15 CPU minutes per cross-sectional layer for one computer node. In general, all EOF simulations were run on a Hewlett-Packard Superdome at the Otto-von-Guericke-Universität Magdeburg (Germany).

Next, the EOF in cylindrical capillaries with destined axial and angular distribution of the  $\zeta$ -potential (Fig. 4.8) was modelled. This configuration can be considered as simplified approach for dealing with a heterogeneous surface charge distribution in porous media under more general conditions. In fact, the spatial scale of locally varying electrical potential is often significant with respect to the thickness of the EDL, and it can have a number of reasons. For example, it may already be introduced by the inherent manufacturing process of a material, specific aging, storage conditions, chemical reactions, or the (eventually irreversible) adsorption of molecular or colloidal species on the surface, with a concomitant

change of the local roughness and electrokinetic properties [61, 67-73]. Consequently, the favourable (i.e., plug-like) EOF velocity profile becomes disturbed by (induced) pressure gradients resulting from an axial variation of the surface charge at the inner wall of a microfluidic channel [71-74]. In turn, this necessarily leads to additional hydrodynamic dispersion. The problem is especially severe for the transport of sample mixtures containing large biomolecules such as proteins, peptides or DNA [75] which are charged and, thus, can interact strongly with the (in most cases) oppositely charged surfaces by hydrophobic and electrostatic mechanisms. As their adsorption progresses in time, it continues to cause unreproducible local, as well as average EOF velocities and significant loss of resolution in the separation of individual components due to an increased axial dispersion coefficient and a strong tailing in the residence-time distributions (characterized by non-Gaussian shape).

In general, the local variations in electrical potential produce a nonuniform electrokinetic driving force that requires a local (positive or negative) pore pressure for compensating the associated momentum in an incompressible fluid [71-74]. Unfortunately, the actual spatial and temporal distribution of electrical potential in a real porous medium is usually unknown making it difficult to study on quantitative basis. On the other hand, this effect may be tailored, e.g., for enhanced microfluidic mixing, by employing surfaces with a patterned charge distribution [27, 76]. For example, Stroock et al. [76] studied the EOF driven by two patterned geometries in rectangular microchannels for the limit of thin double layers. They considered the variation of surface charge both parallel and perpendicular to the applied

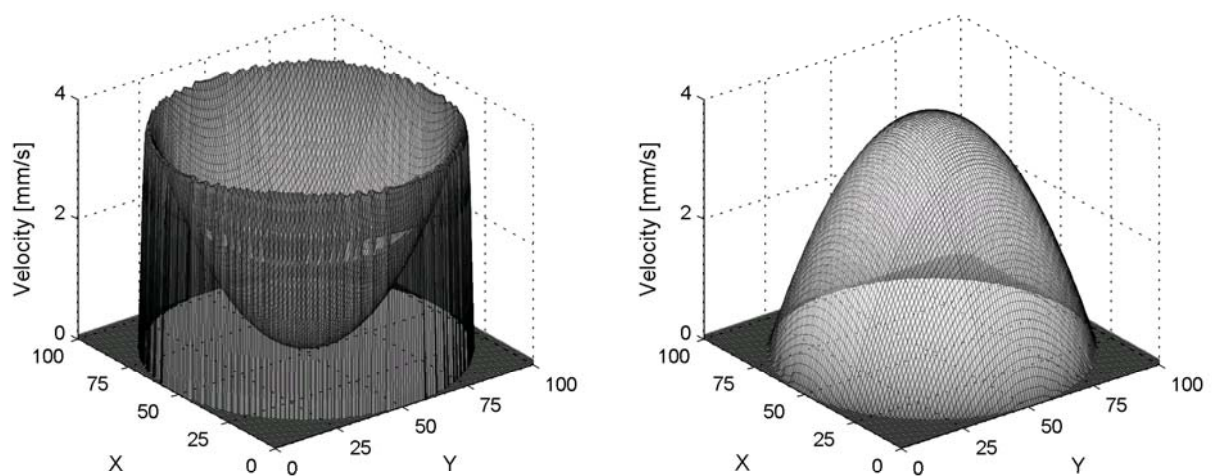


**Figure 4.9.** Local flow profiles in the capillary with surface charge pattern P1 (cf. Fig. 4.8a). Velocity distributions in the center cross-section of each segment for segment A,  $\zeta = -100$  mV (left) and segment B,  $\zeta = 0$  mV (right). The Debye screening length ( $\lambda_D$ ) is 10 nm and  $r_c/\lambda_D = 100$ . Conditions:  $E = 5 \times 10^4$  Vm<sup>-1</sup>, density and viscosity of liquid: 10<sup>3</sup> kg·m<sup>-3</sup> and 0.89×10<sup>-4</sup> kg·m<sup>-1</sup>s<sup>-1</sup>, respectively,  $\epsilon_r = 80$ ,  $T = 298.15$  K.

electrical field: While a recirculating flow develops in the former case, multidirectional flow along the field (and channel axis) results in the latter [76]. Because these types of pattern act as a basis from which more general three-dimensional flows may be constructed and the fluid mechanical consequences of (non)intended surface charge distributions in microfluidic environments be evaluated [77], we also treated similar zeta-potential distributions in cylindrical capillaries (Fig. 4.8). The first pattern (P1) consists of cylindrical segments with a (spatially constant) nonzero and zero zeta-potential, alternating in the axial direction and having the length  $l = 2r_c$ . The second pattern (P2) contains half-cylinders with zeta-potentials of opposite sign, but identical magnitude. The EOF simulations were carried out with a computational resolution of  $r_c/h = 100$  ( $\lambda_D/h = 2$ ). Characteristic local velocity distributions for steady, fully-developed flow resulting when an external electrical field is superimposed on the EDL field in a general electrolyte solution in contact with surface pattern P1 and P2 are shown in Figs. 4.9 and 4.10, respectively.

The EOF in capillaries with heterogeneous distribution of surface charge (or value of  $\zeta$ ) has been the topic of several previous studies. Anderson and Idol [67] have developed an infinite-series analytical solution for EOF through a cylindrical capillary with the  $\zeta$ -potential varying periodically (and solely) in the axial direction. By using a similar approach, Long et al. [74] obtained an explicit solution for specific surface charge defects. Herr et al. [71] considered the EOF in a cylindrical capillary with a step-change of the  $\zeta$ -potential in the axial direction and obtained good agreement with their experimental data. Potoček et al. [68] and

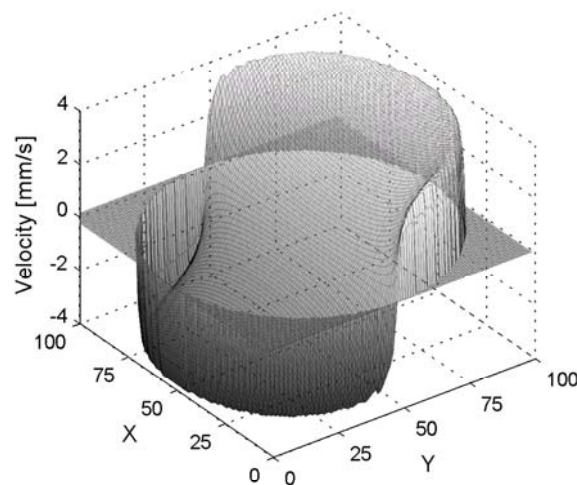


**Figure 4.10.** Simulated axial velocity distribution in a cross-section of the open cylindrical capillary with surface charge pattern P2 (cf. Fig. 4.8b) for  $r_c/\lambda_D = 100$  ( $r_c = 1 \mu\text{m}$ ) and the same conditions as in Fig. 4.9.

Ren and Li [61] have numerically studied the velocity distributions for EOF in circular microchannels for various non-uniform distributions of  $\zeta$ . More recently, Gleeson [78] developed an analytical solution for the EOF problem in a cylindrical capillary with random  $\zeta$ -potential distribution. It should be emphasized that all of the above-mentioned studies were dealing with an axisymmetrical heterogeneity only. Moreover, except for the work of Ren and Li [61], they assumed a negligibly small EDL thickness which allowed to replace the no-slip boundary condition for the fluid velocity at the solid-liquid interface by the Helmholtz-Smoluchowski apparent-slip velocity, Eq. 4.1 and simplify the analytical solution. Ghosal [72] presented a theory for EOF in channels of arbitrary cross-sectional geometry (and distribution of the  $\zeta$ -potential) in the lubrication-limit where all axial variations exist on length scales which are large with respect to a characteristic microchannel width, but the assumption of a thin EDL has been involved also in that theory. Thus, reference values for a quantitative analysis of accuracy with which LB flow fields were computed can be obtained only on the basis of this approximation. It should be pointed out that the "slip" boundary condition eliminates a fluid region close to the surface where velocity rises from zero to some bulk value at the slipping plane. Since the thickness of this region does not depend on channel geometry, the relative contribution of that simplification to the total error decreases with increasing channel diameter or characteristic transverse dimension. For a thin EDL the relation between local flow velocity and radial position in capillary segments A or B of P1 (Fig. 4.8a) can be expressed by [71]

$$v_{\text{seg}}(r) = -\frac{\varepsilon_0 \varepsilon_r E}{\eta_f} \left[ \zeta_{\text{seg}} + 2(\zeta_{\text{av}} - \zeta_{\text{seg}}) \left( 1 - \frac{r^2}{r_c^2} \right) \right], \quad (4.32)$$

where  $\zeta_{\text{av}}$  is the average value of  $\zeta$  at the capillary inner wall (for P1  $\zeta_{\text{av}} = -50$  mV) and  $r_c$  is the capillary radius (the subscript "seg" refers to  $\zeta = 0$  mV or  $\zeta = -100$  mV, respectively). The velocity profiles calculated by using Eq. 4.32 and compared to those obtained from simulated LB flow fields are shown in Fig. 4.11. The low-velocity region close to the capillary wall in the computed flow field reduces the average velocity relative to that value defined by the integration of Eq. 4.32 along the radial direction. However, as mentioned above, the discrepancy decreases with increasing aspect ratio, e.g., the difference between simulated and calculated mean velocities for  $r_c/\lambda_D = 100$  is only 0.45%, while it is 9.7% for  $r_c/\lambda_D = 20$  and 16.7% for  $r_c/\lambda_D = 10$ .

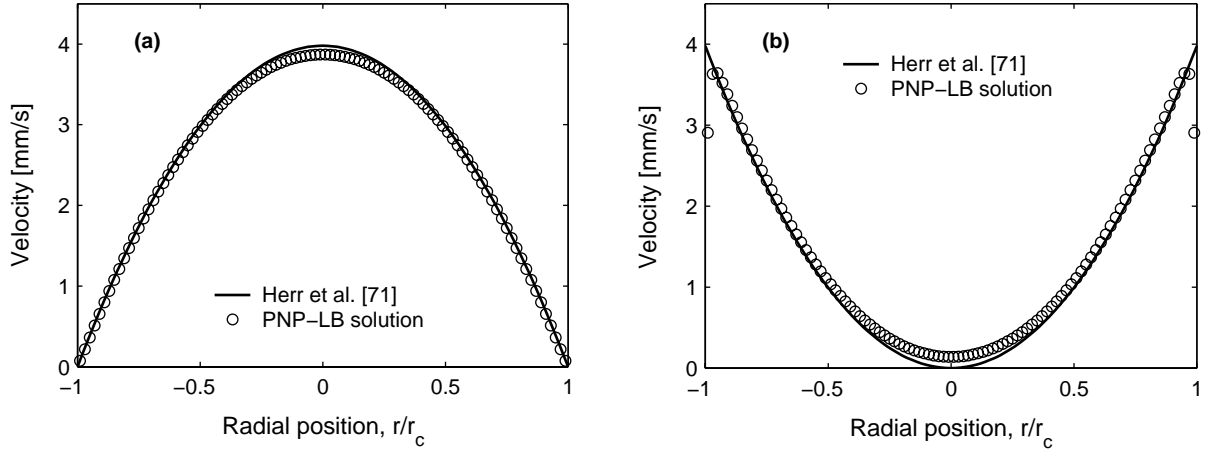


**Figure 4.11.** Capillary with surface charge pattern P1. Comparison of simulated intrasegmental velocity profiles with the analytical solution [71]. a) Center cross-section of segment A ( $\zeta = -100\text{mV}$ ) and the same for the segment B ( $\zeta = 0\text{ mV}$ ).

In contrast to the discrete axial heterogeneity of P1, the second pattern (Fig. 4.8b) is characterized by an azimuthal inhomogeneity. The velocity field for P2 can be obtained in the lubrication limit [72] by numerical solution of the boundary-value problem in polar coordinates for an effective potential  $\xi(\rho, \theta)$  ( $\rho$  and  $\theta$  are radial and azimuthal coordinates)

$$\frac{1}{\rho} \frac{\partial}{\partial \rho} \left( \rho \frac{\partial \xi}{\partial \rho} \right) + \frac{1}{\rho^2} \frac{\partial^2 \xi}{\partial \theta^2} = 0, \quad \begin{aligned} \xi(r_c, \theta) \Big|_{0 \leq \theta < \pi} &= -\zeta \\ \xi(r_c, \theta) \Big|_{\pi \leq \theta < 2\pi} &= \zeta \end{aligned} \quad (4.33)$$

The flow velocity then can be determined from Eq. 4.1 by replacing the local electrical potential  $\psi$  by the effective potential  $\xi$ , and a solution to Eq. 4.33 may be obtained via the following expansion [72]

$$\xi = -\tilde{\zeta}_0 - \sum_{m=1}^{\infty} \left[ \tilde{\zeta}_m \exp(im\theta) + \tilde{\zeta}_m^* \exp(-im\theta) \right] \rho^m, \quad (4.34)$$

where  $\tilde{\zeta}_m$  ( $m = 0, 1, \dots, \infty$ ) is the complex Fourier transform

$$\tilde{\zeta}_m = \frac{1}{2\pi} \int_0^{2\pi} \zeta(\theta) \exp(-im\theta) d\theta. \quad (4.35)$$



It should be pointed out that a quantitative evaluation of the differences between the two discrete velocity fields obtained i) by numerical solution of this problem, Eqs. 4.33-4.35, and ii) from computer simulation becomes difficult due to the different coordinate systems. While numerical solution requires a utilization of the polar (or, at least, cylindrical) system, PNP-LB computer simulations are realized in the cartesian coordinate system. As a result we have two sets of points corresponding to the polar mesh and rectangular grid. Therefore, we analyzed the two velocity fields by using some of their characteristic properties. It is obvious that due to the antisymmetry of the  $\zeta$ -potential distribution in P2 (with respect to a center plane passing through the wall points where the sign of  $\zeta$  changes) the velocity distribution should possess a similar antisymmetry and (net) volumetric flow through the capillary should vanish. Indeed, the simulated velocity field demonstrates such a "self-compensation" (Fig. 4.10) by a deviation of the average velocity from zero of less than  $10^{-6}$  % as compared to the average velocity in the capillary with uniform zeta-potential ( $\zeta = -100$  mV). The velocity profiles in the plane  $[\theta = \pi/2, \theta = 3\pi/2]$ , which is perpendicular to the antisymmetry plane, obtained by solution of the problem in Eqs. 4.33-4.35 and by computer simulation are shown in Fig. 4.12. Since the electromotive forces are effective only in a small region close to the wall of the capillary, actual differences in velocity profiles should be explained by the

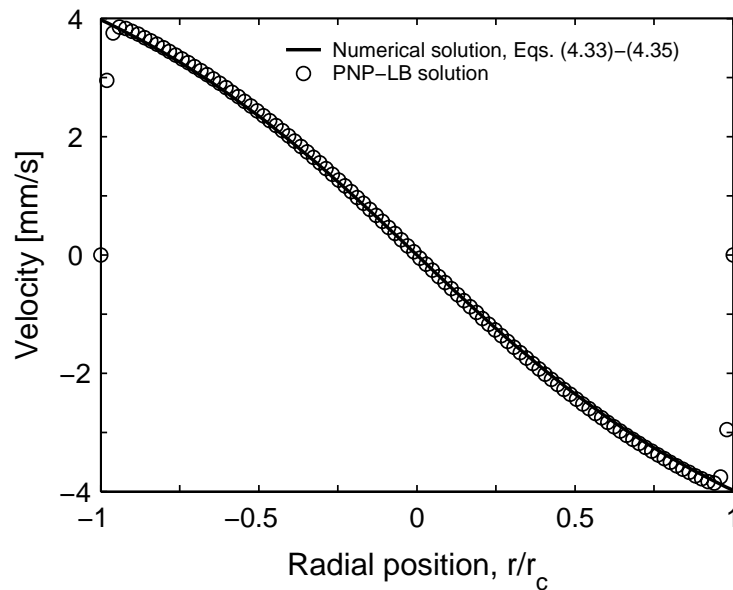


**Figure 4.12.** Comparison of velocity distributions in the plane  $[\theta = \pi/2, \theta = 3\pi/2]$  for the open capillary with surface charge pattern P2.

respective velocity boundary conditions. While the slip-condition assumes a discontinuous change of the flow velocity at points where  $\zeta$  changes its sign (Fig. 4.13) our simulated velocity field (Fig. 4.10) here demonstrates a more realistic, smooth transition. As already shown for surface charge pattern P1, the global relative error in the flow field associated with the "no-slip violation" soon becomes significant as the aspect ratio ( $r_c/\lambda_D$ ) is reduced below 50. In this domain, for  $r_c/\lambda_D < 100$ , the slip-condition should be used with care concerning a numerical investigation of the EOF and resulting hydrodynamic dispersion. Consequently, this approximation does not appear useful in simulating flow through complex porous media with a broad range of aspect ratios ( $1 \approx r_c/\lambda_D \gg 1$ ), and the more general approach described in this work could be followed.

#### 4.1.5. Conclusions and outlook

A numerical method for three-dimensional simulation of EOF in microfluidic channels was presented. It is applicable to structures with arbitrary pore space morphology (including their geometry, as well as topology) and an arbitrary distribution of the electrokinetic

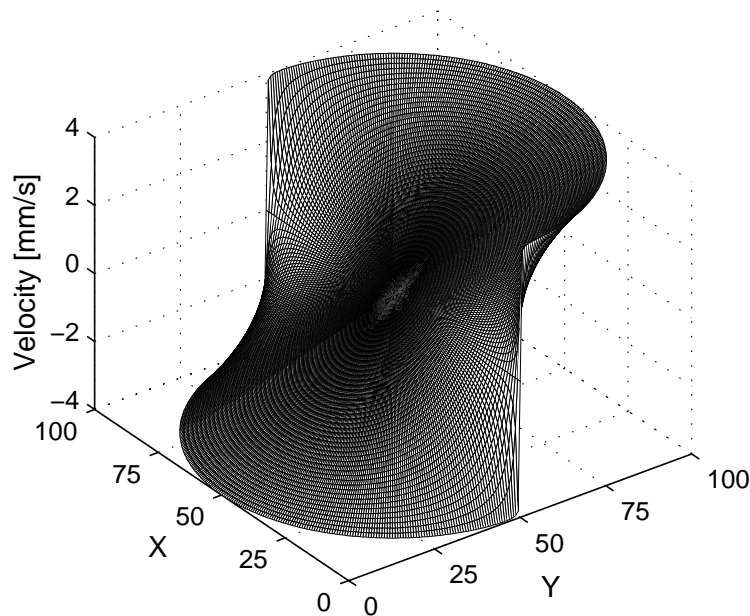


**Figure 4.13.** Velocity profile in a cross-section of the open cylindrical capillary ( $r_c = 1 \mu\text{m}$ ) with surface charge pattern P2 according to the approach of Ghosal [72]. The same conditions as in Figs. 4.9 and 4.10 have been used here.

potential at the solid-liquid interface. This also covers the existence of random pore size distributions and, as a consequence, the possibility of finding any range of aspect ratios in a particular medium. Coupled hydrodynamic, electrostatic, and mass transport problems were solved. In this work, the hydrodynamic problem has been treated with the lattice-Boltzmann method. Straight capillaries were chosen as model systems due to the possibility of comparing our simulated data with the analytical solution and results of other numerical simulations for simple system configurations in the effort to present the basis for an efficient modelling of electrokinetic transport phenomena in more complex porous media. Good agreement was obtained for different benchmark cases.

A low-Reynolds number EOF dynamics on micrometer dimension is not only encountered in the open-channel structures of microchip supports, but also in the pore space of microscopically disordered media like random sphere packings or monolithic devices [59]. For example, in capillary electrochromatography, as for most of the microchip applications, the EOF is employed for achieving a significantly less dispersive transport (compared to pressure-driven flow) of complex mixtures of (bio)molecular species which are separated on these high-surface area materials to become identified afterwards by post-column, preferably on-line detection (e.g., via mass spectrometry). Our numerical approach based on the lattice-Boltzmann flow field under most general conditions can cope with any geometry and possible surface heterogeneity, and it will be particularly efficient in resolving details of the flow field which govern mass transport and dispersion in a transient, as well as long-time asymptotic regime. For complex porous media and flow patterns the presented approach can contribute to the derivation of scaling laws for EOF involving parameters such as the Reynolds and Peclet numbers, mass diffusivity, medium morphology or electrical double layer thickness. However, this also needs further investigation of double layer resolution effects and of the limits when employing a slip-velocity boundary condition, in particular with respect to the characteristic lengths in a porous medium (e.g., the sphere or intraparticle pore diameter in a bed of porous spherical particles), continuously changing channel dimensions and varying shape, or the spatio-temporal heterogeneity of a local surface charge distribution. Another subject of research, the effect of the EOF on an electrical surface charge density at a heterogeneous solid-liquid interface, is considered in the next section.



## **4.2. Numerical Simulation of Electroosmotic Flow in Heterogeneous Slit Microchannels with Non-Equilibrium Electric Double Layer**

### *4.2.1. Introduction*

In the last years the study of electroosmotic flow (EOF) in microfluidic channels has received much attention in the scientific community since many applications in emerging microfluidic device technology and analytical (bio-)chemistry, e.g. microelectronic cooling systems, “lab-on-a-chip”, capillary electrophoresis and capillary electrochromatography (CEC), involve the manipulation of fluid transport on micro- and nanoscales. Electroosmosis offers a number of distinct advantages for fluid motion control in fine channels. First, the EOF becomes an increasingly effective means for liquid transport in channels with transversal dimensions on the order of a few micrometers and less, since to propel and control fluids inside such microchannels, a very high pressure gradient is required. Another benefit of the employment of EOF for fluid transport is reduced hydrodynamic dispersion, which can be limited almost to that by diffusion. This fact is of particular importance for use of EOF in separation techniques and critically influences the (high) efficiency of a process.

The electroosmosis phenomenon is directly related to formation of the electrical double layer (EDL) near a solid-liquid interface. Most solid surfaces obtain an electrical surface charge when they are brought in contact with a polar solvent, for instance, with an electrolyte solution. The origins of this charge can be diverse, for example, dissociation of surface groups, structural crystal defects or adsorption of ions. The surface charge, in turn, influences the ion distribution in a liquid and is compensated by the accumulation of counter-ions and depletion of co-ions in a thin liquid layer (in the EDL) next to the solid-liquid interface. At some distance away from the solid surface (this distance depends on the ionic strength of a solution), the liquid becomes neutral. At equilibrium, when neither an external electric field, nor a pressure gradient is present, ion distributions are governed only by thermal diffusion and electrostatic forces arising from the surface charge and obey the Boltzmann equation. The application of an external electric field exerts a body force on liquid in the EDL and results in fluid motion (electrokinetic flow). It should be mentioned that close to the interface counter-ions are undergoing very strong interactions with the interface by short-range attractive forces and can be regarded as immobile. The electrical potential existing at the boundary between the mobile and immobile phases of a liquid (at the so-called shear plane) is known as electrokinetic or zeta ( $\zeta$ ) potential. Hence, the EOF phenomenon is a

complex function, in general, of the local net charge density, local electrical potential, as well as the local physical characteristics of the microchannel, its walls and saturating liquid.

Most of the experimental, theoretical, and numerical studies to date have focused on EOF in an axially homogeneous channels. This assumes a uniform zeta potential distribution along the channel walls. Moreover, in straight homogeneous channels the equilibrium distribution of ions is not disturbed by steady-state fluid flow after an external electrical field or pressure gradient has been applied. This allows to describe the EOF problem in such a system by the coupled Poisson-Boltzmann and momentum balance equations [8]. Since the Poisson-Boltzmann equation has no general analytical solution, the abovementioned problem has been extensively studied by numerical methods or under the linearization (Debye-Hückel) approximation for slit, rectangular, cylindrical, annular, and trapezoidal channels [13, 22, 27, 74, 79-84]. However, the actual physico-chemical properties of the channel walls must be considered as inhomogeneous under more general conditions. Besides spatial inhomogeneities prepared intentionally during the fabrication of microfluidic devices, e.g. in electroosmotic stirrers, heterogeneous properties of microchannel walls can also arise accidentally due to, for instance, their chemical modification during operation or adsorption of transported species. Whether a surface inhomogeneity is intended or unavoidable, it affects the EOF and introduces additional heterogeneities in fluid flow. The effect of a non-uniform zeta-potential distribution on properties of EOF in planar, rectangular, and cylindrical microchannels has been investigated by a number of researchers [27, 72, 74, 76, 78, 167]. However, all of these studies have been limited by assumptions of a thin double layer (TDL) and/or an equilibrium distribution for the net charge density. The TDL approximation assumes the EDL to be infinitely thin ( $y/\lambda_D \gg 1$ , with  $y$  being the characteristic transversal dimension of a channel) and the effect of an external electric field on EOF velocity reduces to that represented by the Helmholtz-Smoluchowski equation [8]

$$\mathbf{v}_{eo} = -\frac{\varepsilon_r \varepsilon_0 \zeta \mathbf{E}_{ext}}{\eta} \quad (4.36)$$

as the boundary condition at a solid-liquid interface. Thus, this approximation replaces the original problem by a simplified, hydrodynamic one with “slip boundary conditions”. The detailed analysis of conditions required for the applicability of this “slip velocity model” has been performed by Santiago [20] and MacInnes [85]. It has been shown that a number of conditions for channel dimensions in relation to the EDL thickness must be satisfied. Though involving the solution of the Poisson-Boltzmann equation allows to exclude the restriction

$y/\lambda_D \gg 1$ , the effect of fluid flow and ion electromigration due to the external electric field on the distributions of the electrical net charge and potential within the EDL has not yet been taken into account. In the case of a heterogeneous channel, advection and the applied electric field may affect the net charge density which does not then conform to the equilibrium distribution. Fu et al. [86] shown that results provided by the Poisson-Boltzmann model can differ significantly from that obtained by adopting the Nernst-Planck equation to describe the charge transport along the microchannel with step-wise change in  $\zeta$ -potential. Their developed model was based on the numerical solution of the coupled Poisson, Nernst-Planck, and modified Navier-Stokes equations. Although the local electric potential and ion distributions within the EDL have been determined as non-equilibrium values, the aforementioned set of coupled equations has been resolved subject to boundary conditions which were assumed to be not affected by fluid motion and ion transport. Indeed, variations in the spatial gradient of surface charge density can also arise due to changes in the local chemical environment at solid surfaces caused by fluid flow or electromigration of ions. For example, adsorption of charged species from the electrolyte at the capillary walls during the sample elution in CEC can significantly change the local surface charge and electrokinetic properties of the whole system [73]. On the other hand, it is known that surface charge density and consequently the  $\zeta$ -potential of an inorganic oxides-aqueous solution interface, for instance silica—KCl electrolyte, depend particularly on the pH of the solution [87]. Hence, any local variation of pH in vicinity to the solid-liquid interface results in a local deviation of surface charge density (and  $\zeta$ -potential) due to variations in the dissociation rate of surface functional (e.g., silanol) groups which are involved in pH-dependent dissociation equilibria. Thus, a more satisfactory description of the EOF problem in microchannels with non-uniform surface charge density (or  $\zeta$ -potential) must involve an *interdependence* of the EOF and electrical boundary conditions. In other words, the whole EDL must be considered as being a *non-equilibrium* domain.

The current paper presents an analysis of the EOF in a slit microchannel with heterogeneous wall properties which are manifested in a spatially variable rate of dissociation of surface silanol groups at the “silica—aqueous solution” interface. All physical quantities such as flow velocity, local electrical potential and ion concentrations, as well as the electrical boundary conditions (the surface charge density or  $\zeta$ -potential) are assumed to be interdependent. The case of the fixed surface charge density ( $\zeta$ -potential) distribution, which implies possible spatial variations, but does not allow variations due to local changes of the chemical environment of the solid-liquid interface, can be considered as the limiting case.

Also results of the EOF simulations in a slit microchannel with the fixed surface charge density distribution are compared to those which are obtained by the model of the non-equilibrium EDL with a consequently variable surface charge.

#### 4.2.2. Mathematical description

##### General formulation

Consider steady-state low-Reynolds number flow of a Newtonian incompressible  $N$ -component electrolyte solution. When an external electric field  $\mathbf{E}_{\text{ext}}$  is applied, the EDL interacts with it and an electrostatic body force  $\mathbf{f}$  is imposed which results in electroosmotic flow. If the viscosity of the solution  $\eta$  is assumed to be constant, the EOF velocity field  $\mathbf{v}$  is governed by the following Navier-Stokes equation

$$\rho_f (\mathbf{v} \cdot \nabla) \mathbf{v} = -\nabla p + \rho_f \eta \nabla^2 \mathbf{v} + \rho_q \nabla \Phi, \quad (4.37)$$

where  $\rho_f$  is the fluid density,  $p$  is the pressure, and  $\rho_q$  is the volume net electric charge density. The distribution of the local electrical potential  $\Phi$  is described by the Poisson equation

$$\nabla^2 \Phi = -\frac{\rho_q}{\epsilon_r \epsilon_0} = -\frac{q_e}{\epsilon_r \epsilon_0} \sum_{i=1}^N z_i n_i, \quad (4.38)$$

where  $\epsilon_r$  is the dielectric constant of the solution,  $\epsilon_0$  is the permittivity of vacuum,  $q_e$  stands for the elementary charge,  $z_i$  and  $n_i$  are the valency and the number concentration of ionic species  $i$ , respectively. In turn, the flux of each ionic species  $\mathbf{j}_i$  in dilute solutions consists of three linearly superimposed contributions: convection, electromigration, and diffusion. They can be written in form of the Nernst-Planck equation

$$\mathbf{j}_i = \left( \mathbf{v} - \frac{q_e z_i D_i \nabla \Phi}{k_B T} \right) n_i - D_i \nabla n_i, \quad (4.39)$$

where  $D_i$  is the mass diffusion coefficient,  $k_B$  the Boltzmann constant and  $T$  the absolute temperature. Under steady-state conditions the species conservation leads to

$$\nabla \cdot \mathbf{j}_i = 0. \quad (4.40)$$



Coupled partial (in general case, three-dimensional) differential equations 4.37, 4.38 and 4.39 expressing the functional relations between flow velocity, electrical potential, and species number concentrations in the fluid should be complemented by boundary conditions which determine the value of these physical quantities at the solid-liquid interface  $\Omega$ . Since the mathematical solution of such a problem is generally very difficult, it will invoke a number of assumptions mentioned in the Introduction in order to simplify the problem and reduce it to a form that can be more readily solved. For tracing back how the simplifications modify the original problem, we formulate the latter in a symbolic form

$$\mathbf{v} = F_1(\Phi(\mathbf{r}), n_i(\mathbf{r})) \quad (\text{Navier-Stokes equation}), \quad (4.41)$$

$$\Phi = F_2(n_i(\mathbf{r})) \quad (\text{Poisson equation}), \quad (4.42)$$

$$n_i = F_3(\mathbf{v}(\mathbf{r}), \Phi(\mathbf{r})) \quad (\text{Nernst-Planck equations}), \quad (4.43)$$

$$\mathbf{v}|_{\Omega} = B_1(\Phi(\mathbf{r}), n_i(\mathbf{r}))|_{\Omega}, \quad (4.44)$$

$$\Phi|_{\Omega} = B_2(\mathbf{v}(\mathbf{r}), n_i(\mathbf{r}))|_{\Omega}, \quad (4.45)$$

$$n_i|_{\Omega} = B_3(\mathbf{v}(\mathbf{r}), \Phi(\mathbf{r}))|_{\Omega}, \quad (4.46)$$

where  $F_1, F_2, F_3$  and  $B_1, B_2, B_3$  are symbolic designations of the functional relations between the physical quantities in the fluid and at the solid-liquid interface, respectively. It should be realized that fluid flow over most solid-liquid interfaces can be characterized by the no-slip condition, although the correctness of its applicability on micro- and nanoscales remains to be evaluated more exactly [88, 89]. The no-slip boundary condition for the velocity field allows to replace Eq. 4.44 by

$$\mathbf{v}|_{\Omega} = 0. \quad (4.47)$$

Then, assuming the impermeability of the solid surface the distributions of the species number concentrations must satisfy the normal-zero-flux condition

$$\vec{v} \cdot \mathbf{j}_i|_{\Omega} = 0, \quad (4.48)$$

where  $\vec{v}$  is the outer normal to the solid-liquid interface. Below in the present paper, the boundary conditions for the velocity field and species concentrations are always assumed to be expressed by Eqs. 4.47 and 4.48 independently of other assumptions and approximations related to the electrical boundary conditions.

#### Thin double layer (TDL) approximation

The imposition of this approximation replaces the original electrohydrodynamic problem by a simplified hydrodynamical one. Since only bulk (neutral) fluid is considered, the conventional Navier-Stokes equation without the term related to electrostatic forces is solved, i.e. the velocity field does not depend explicitly on the electrical potential distribution. The Navier-Stokes equation must be subject to the slip velocity boundary condition that is determined by the Helmholtz-Smoluchowski equation (Eq. 4.36)

$$\mathbf{v} = F_1(\mathbf{r}), \quad (4.49)$$

$$\mathbf{v}|_{\Gamma} = B_1(\zeta(\mathbf{r}))|_{\Gamma}. \quad (4.50)$$

Non-uniform  $\zeta$ -potential reveals itself through the non-uniform slip boundary conditions. If all deviations from the equilibrium state in the EDL can be neglected (the small perturbation assumption), this approach can be effectively applied to study the EOF in heterogeneous channels, especially when channel properties vary very slowly in longitudinal direction [72] or they can be considered as locally uniform [71, 74].

#### Equilibrium EDL

If transversal dimensions of the channel are not much bigger than the EDL thickness, the TDL approximation yet cannot be applied, since the effect of the EDL field and its variations on the flow field can be quite significant. Assuming that ionic concentrations in the EDL are affected only by thermal diffusion and electrostatic forces due to the surface charge, i.e., the equilibrium EDL, the species density distribution should obey the Boltzmann equation. Hence, Eqs. 4.41-4.43 can be rewritten in the following manner:

$$\mathbf{v} = F_1(\Phi(\mathbf{r}), n_i(\mathbf{r})), \quad (4.51)$$

$$\Phi = F_2(n_i(\mathbf{r})), \quad (4.52)$$

$$n_i = F_3(\Phi(\mathbf{r})), \quad (4.53)$$

where Eq. 4.53 is the Boltzmann equation. By putting Eq. 4.52 into Eq. 4.53 this leads to the so-called Poisson-Boltzmann equation and, then, the decoupled Eq. 4.51 is solved as a separate problem with the given electrical potential and species concentration distributions. The corresponding electrical boundary conditions are

$$\Phi(\mathbf{r})|_{\Omega} = \zeta(\mathbf{r})|_{\Omega} \quad \text{or} \quad (4.54)$$

$$\nabla\Phi(\mathbf{r})|_{\Omega} = -\frac{\sigma(\mathbf{r})}{\epsilon_r\epsilon_0}|_{\Omega}. \quad (4.55)$$

This approach has been applied to study the EOF in channels with step-wise changes in the  $\zeta$ -potential [27, 61]. It should be pointed out that such approximation neglects transition regions for EOF near the locations of the  $\zeta$ -potential changes.

### Non-equilibrium EDL

Since convection and electromigration due to an external electric field can affect the species concentrations in the EDL of heterogeneous channels, the ionic distributions rather must be described by the Nernst-Planck equation than the Boltzmann equation. The symbolic problem formulation can be presented by

$$\mathbf{v} = F_1(\Phi(\mathbf{r}), n_i(\mathbf{r})) \quad (\text{Navier-Stokes equation}), \quad (4.56)$$

$$\Phi = F_2(n_i(\mathbf{r})) \quad (\text{Poisson equation}), \quad (4.57)$$

$$n_i = F_3(\mathbf{v}(\mathbf{r}), \Phi(\mathbf{r})) \quad (\text{Nernst-Planck equations}), \quad (4.58)$$

$$\Phi(\mathbf{r})|_{\Omega} = \zeta(\mathbf{r})|_{\Omega} \quad \text{or} \quad \Phi(\mathbf{r})|_{\Omega} = - \frac{\sigma(\mathbf{r})}{\epsilon_r \epsilon_0} \Big|_{\Omega}. \quad (4.59, 4.60)$$

Fu et al. [86] compared results of EOF simulations in a microchannel with step-wise change in the  $\zeta$ -potential (predicted by this model) with those obtained under the approximation of an equilibrium EDL and found that significant differences can exist, especially near the locations subjected to  $\zeta$ -potential changes.

*Non-equilibrium EDL with variable surface charge*

All aforementioned approaches assume that the surface charge and, consequently, the  $\zeta$ -potential do not depend on the local chemical environment and that they are only spatially dependent quantities. In fact, properties of solid surfaces can change due to fluid and ion transport in the adjacent liquid. The explicit form of the relationship between the surface charge and properties of the local chemical environment is defined by the nature of the solid-liquid interface. To become more concrete we will consider the EDL formed due to dissociation of surface silanol groups:



This mechanism of the surface charge development is peculiar to “silica—water” (or “silica—aqueous solution”) interfaces. Under extremely acidic conditions further protonation of silanol groups can take place [90], however, we disregard this case as anomalous.

If the silica surface is in contact with an aqueous solution, surface silanol groups are dissociated, giving rise to surface charge density

$$\sigma = -q_e \Gamma_{\text{SiO}^-}, \quad (4.62)$$

where  $\Gamma_{\text{SiO}^-}$  is the surface density of dissociated silanol groups, which, in turn, follows the relevant mass action law for the deprotonation reaction

$$\frac{[\text{H}^+]_0 \Gamma_{\text{SiO}^-}}{\Gamma_{\text{SiOH}}} = 10^{-\text{pK}}, \quad (4.63)$$

where  $[H^+]_0$  is the surface activity of protons and  $pK$  is the logarithmic dissociation constant. Without loss of generality, we assume the liquid to be an aqueous solution with simple symmetric 1:1 indifferent electrolyte ions such as NaCl. In this case, the surface charge density is completely determined by the surface density of dissociated silanol groups and can be expressed by combining of Eqs. 4.62 and 4.63

$$\sigma = -\frac{q_e \Gamma_{\text{tot}} \cdot 10^{-pK}}{[H^+]_0 + 10^{-pK}}, \quad (4.64)$$

where  $\Gamma_{\text{tot}} = \Gamma_{\text{SiOH}} + \Gamma_{\text{SiO}^-}$  is the total surface density of chargeable silanol groups. Equation 4.64 can be considered as the explicit form of Eq. 4.45, which relates the electrical boundary condition to the species concentrations.

#### 4.2.3. EOF in a slit heterogeneous microchannel

We consider the problem of EOF in a slit heterogeneous microchannel (Fig. 4.13a) using the mathematical formulation presented in the previous section. The channel consists of two identical, infinitely large, parallel and impermeable plates, and these gap between the plates is filled with an electrolyte solution. Then, we assume that the heterogeneity of the inner surface is manifested in the total surface density of chargeable silanol groups  $\Gamma_{\text{tot}}$ , which characterizes the surface charge density formed due to the dissociation of surface silanol groups (see Eq. 4.64). If the non-uniformity exists only along one direction, for instance along the  $x$ -axis, the problem can be reduced to the two-dimensional case ( $x, y$ ). In addition, we assume spatial periodicity along the  $x$ -direction which allows to reduce the problem description to that of the unit cell (Fig. 4.13b).

Below in the present paper we assume also that a strong acid (e.g., HCl) or a strong base (e.g., NaOH) is added to the aqueous solution of a 1:1 electrolyte (e.g., NaCl), in order to adjust its pH. Then, the ionic structure of a liquid phase can be assumed to consist of the following four components (species):

- Cations:  $\text{Na}^+, \text{H}_3\text{O}^+$
- Anions:  $\text{OH}^-, \text{Cl}^-$

The governing equations have to be solved subject to the periodic conditions at the entry and outlet boundaries of the unit cell

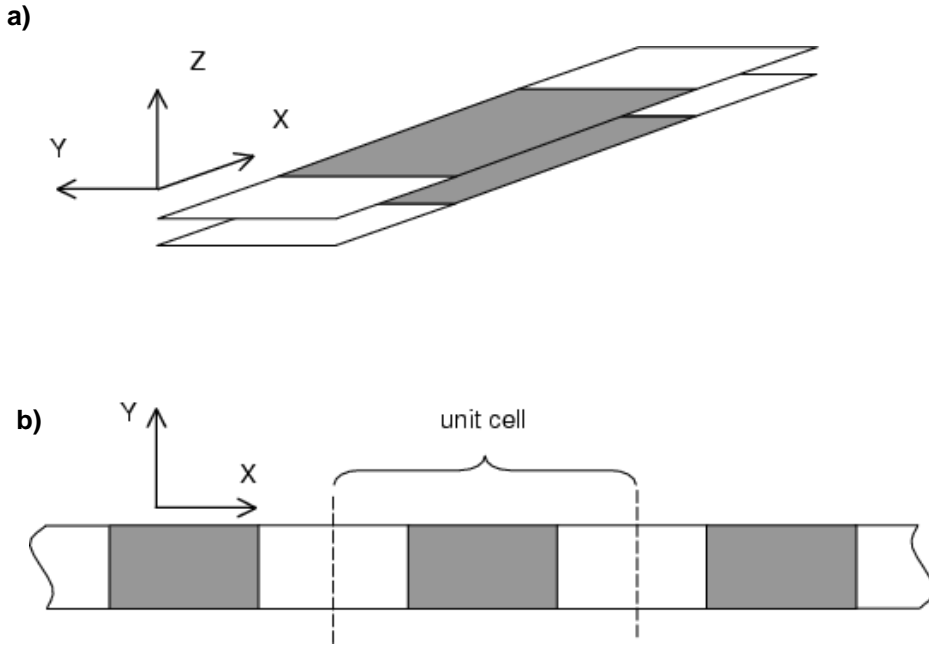


**Figure 4.13.** Schematics of a slit microchannel. (a) The unit cell, (b) periodic sequence of unit cells forming an infinite structure.

$$[[\Phi]] = C, [[n_i]] = 0, [[\mathbf{v}]] = 0, \quad (4.65)$$

as well as to the lateral boundary conditions at the solid-liquid interface at the walls

$$\nabla\Phi(\mathbf{r})|_{\Omega} = -\frac{\sigma(\mathbf{r})}{\epsilon_r\epsilon_0}\Big|_{\Omega}, \quad \vec{\nu}\cdot\mathbf{j}_i|_{\Omega} = 0, \quad \mathbf{v}|_{\Omega} = 0, \quad (4.66)$$

where  $C$  is a constant related to the conditions of an experiment (including pH, the electrolyte concentration,  $\mathbf{E}_{\text{ext}}$ , surface adsorption, or temperature) and  $[[\dots]]$  denotes the difference between values of a function at opposite points lying on the corresponding unit boundaries. In addition, since the present model does not include buffer reservoirs, the species density distribution must satisfy the mass conservation principle within the unit cell

$$\int_V n_i dV = N_i, \quad (4.67)$$

where  $V$  is the volume of the unit cell and  $N_i$  is the total number of ions of the  $i$ th species.

The total numbers of  $\text{Na}^+$  and  $\text{Cl}^-$  ions ( $N_{\text{Na}}$  and  $N_{\text{Cl}}$ ) are constants determined only by the amount of the dissolved solute ( $N_{\text{Na}}^{\text{salt}}$  and  $N_{\text{Cl}}^{\text{salt}}$ ) and the added acid/base ( $N_{\text{Na}}^{\text{base}}$  and  $N_{\text{Cl}}^{\text{acid}}$ ), or in terms of molarities:

$$c_{\text{Na}} = c_{\text{Na}}^{\text{salt}} + c_{\text{Na}}^{\text{base}}, \quad (4.68)$$

$$c_{\text{Cl}} = c_{\text{Cl}}^{\text{salt}} + c_{\text{Cl}}^{\text{acid}}, \quad (4.69)$$

while the total concentrations of hydrogen (hydronium) and hydroxyl ions,  $c_{\text{H}_3\text{O}^+}$  and  $c_{\text{OH}^-}$ , depend on the amount of added acid/base and are regulated also by the autodissociation of water,  $2\text{H}_2\text{O} \Leftrightarrow \text{H}_3\text{O}^+ + \text{OH}^-$

$$c_{\text{H}_3\text{O}^+} = c_{\text{H}_3\text{O}^+}^{\text{water}} + c_{\text{H}_3\text{O}^+}^{\text{acid}}, \quad (4.70)$$

$$c_{\text{OH}^-} = c_{\text{OH}^-}^{\text{water}} + c_{\text{OH}^-}^{\text{base}}, \quad (4.71)$$

$$c_{\text{H}_3\text{O}^+} c_{\text{OH}^-} = K_w, \quad (4.72)$$

where  $K_w$ , the dissociation constant of water, has the value of  $1.0 \times 10^{-14}$  at  $25^\circ\text{C}$ . Addition of acid or base compounds causes an increase, respectively, in the hydronium or hydroxyl ion concentrations, but does not change their product. Since  $c_{\text{Na}}^{\text{base}} = c_{\text{OH}^-}^{\text{base}}$ ,  $c_{\text{Cl}}^{\text{acid}} = c_{\text{H}_3\text{O}^+}^{\text{acid}}$  and recalling the relation between pH and  $c_{\text{H}_3\text{O}^+}$ , Eqs. 4.48-4.72 allow to determine the ionic composition of the solution that can be used for the species density normalization in accordance with Eq. 4.67.

#### 4.2.4. Implementation and results of the simulations

The presented approach to the EOF flow simulation in a heterogeneous slit microchannel (Fig. 4.13) with variable surface charge density was implemented as parallel computer code and employed to analyse the simulated EOF velocity fields. The details of the numerical implementation were described in Section 4.1, therefore only a brief account is given below. As compared to the numerical scheme presented in Section 4.1, only one

modification was made. After each iterative solution of the Nernst-Planck equation, the local concentrations of hydronium and hydroxyl ions were normalized in accordance with the water dissociation equilibrium (Eq. 4.72). Then, the updated distribution of the hydronium ion concentration was used to calculate the current local surface charge density by Eq. 4.64.

EOF was modelled by the iterative numerical solution of the coupled Poisson, Nernst-Planck, and Navier-Stokes equations using a uniform 3-D grid. While the traditional finite-difference schemes were used to solve the first two equations, the Navier-Stokes problem was resolved by the lattice Boltzmann algorithm. The boundary conditions at a solid-liquid interface for the flow velocity and ionic flux were the no-slip and normal-zero-flux conditions, respectively. The electrical boundary condition was formulated in terms of the local surface charge density which depends on the local hydronium ion concentration, as well as on the local total surface density of chargeable silanol groups (Eq. 4.64). The iterative solution stopped as the divergence rate for the velocity field

$$\gamma = \sqrt{\frac{\sum_{k,l,m} (\hat{v}_{k,l,m} - \tilde{v}_{k,l,m})^2}{\sum_{k,l,m} \tilde{v}_{k,l,m}^2}}$$

became less than the predefined value (in this paper we used  $10^{-4}$  as that value).  $\hat{v}_{k,l,m}$  and  $\tilde{v}_{k,l,m}$  correspond to velocity at the  $(k,l,m)$ -node for the current and previous iterations, respectively. The summation in the above equation was performed over all computational grid nodes. The computational grid resolution was  $400 \times 200$  nodes along the  $x$ - and  $y$ -directions, respectively.

First, we verified the ability of the model to simulate adequately EOF in systems with various values of pH and ionic concentration of the solution. For that purpose EOF through a *homogeneous* slit microchannel with three different 1:1 electrolyte concentrations, 0.1 mM, 1.0 mM, and 10 mM was modelled. The microchannel wall material was assumed to be glass with a total surface density of chargeable silanol groups of  $\Gamma_{\text{tot}} = 4.6 \times 10^{18} \text{ m}^{-2}$  [91] and an intrinsic equilibrium constant for silanol dissociation of  $\text{pK} = 6.37$  [92]. For each concentration, the pH was varied in the range from 5.0 to 7.0 by adding strong (monoprotic) acid or strong base. The transversal dimension of the microchannel ( $Y$ ) was adjusted to keep constant the ratio  $\alpha$  with respect to the electrical double layer thickness ( $\lambda_D$ ),  $\alpha = Y/\lambda_D = 100$ . This precluded an overlap of the electrical double layers from opposite walls and allowed to involve the thin double layer approximation in order to calculate the  $\zeta$ -potential by the



Helmholtz-Smoluchowski equation (Eq. 4.36) for each value of the electrolyte concentration and pH. Then, these calculated values were compared with selected values obtained for silica-solution interfaces by streaming potential measurements [87], as well as with results of a direct numerical simulation of the equilibrium  $\zeta$ -potential of silica capillaries [93]. In Figure 4.14

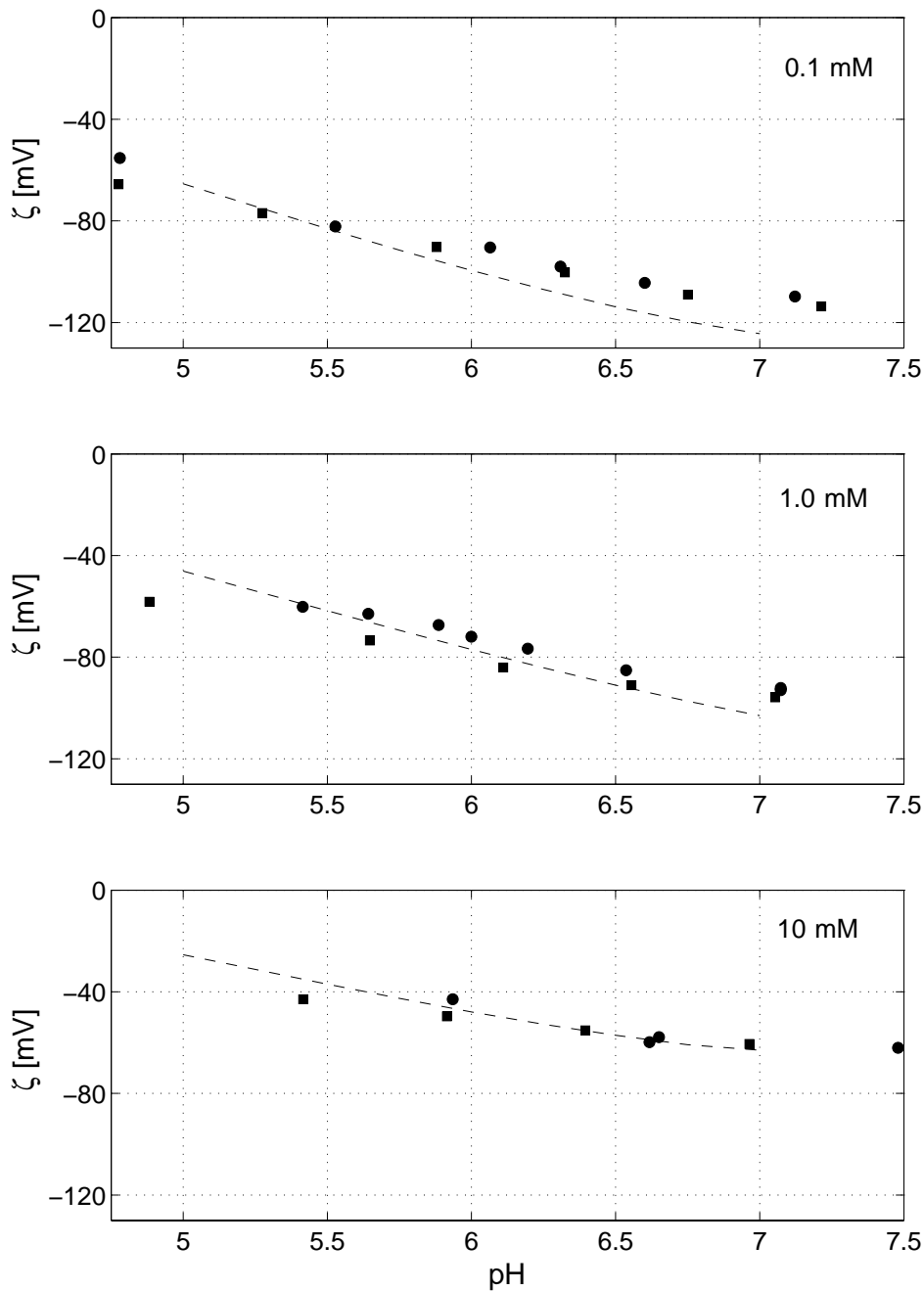


**Figure 4.14.**  $\zeta$ -potential of the silica surface as a function of pH for different concentrations of a (1:1) electrolyte. Symbols are experimental data from Scales et al. [87] (solid circles) and results of simulations from Berli et al. [93] (solid squares). Dashed lines correspond to the results obtained with the presented numerical approach.

the results of both involved studies are compared with data obtained by our presented approach. Although the simulated results suggest a certain overestimation for 0.1 mM at higher pH, the overall agreement with the referenced data is good and one can conclude that the model describes with sufficient accuracy the electrokinetic behaviour of the simulated systems when the species concentrations, pH and, as a consequence, surface charge density have to be considered as locally variable.

In the next step we modelled electroosmotic flow in a microchannel with inhomogeneous wall properties concerning the aforementioned parameters. The simulation domain was reduced to the unit cell due to the assumed homogeneity in transversal directions and axial periodicity. The axial wall inhomogeneity was manifested in an alternation of stripe-like zones with different values of  $\Gamma_{\text{tot}}$ . As it was supposed above, these zones are assumed to be oriented perpendicularly to the applied electric field, whence the problem can be reduced to a two-dimensional one (Fig. 4.13b). It should be realized that such a reduction pursued exclusively the possibility to present more clearly the results of our simulations, since the presented approach was implemented in three dimensions. Further, the stripe-like pattern was assumed to result from the alteration of only two types of zones, with  $\Gamma_{\text{tot}} = 4.6 \times 10^{18} \text{ m}^{-2}$  and  $\Gamma_{\text{tot}} = 0$ , i.e., the latter corresponds to regions without surface electrical charges. Both types of zones had the same width  $l$ . As before, the liquid phase was represented by a 1:1 electrolyte, and acid or base was allowed to be added as pH-regulating compounds. The microchannel geometrical dimensions,  $L$  and  $l$ , were adjusted for each simulation to maintain a constant ratio with respect to the EDL thickness,  $L = l = 100\lambda_{\text{D}}$ , which was determined by

$$\lambda_{\text{D}} = \sqrt{\frac{\varepsilon_r \varepsilon_0 k_{\text{B}} T}{q_{\text{e}}^2 (n_{\infty}^{\text{salt}} + n_{\infty}^{\text{reg}})}},$$

where  $n_{\infty}^{\text{salt}}$  and  $n_{\infty}^{\text{reg}}$  are bulk number concentrations of a dissolved salt and a pH-regulating compound. For each value of the electrolyte concentration and applied electric field a numerical simulation of the EOF was performed three times reproducing A) the case of the equilibrium EDL, B) the non-equilibrium EDL and case of non-variable surface charge density, and C) the case of the non-equilibrium EDL with variable surface charge density. Results of these simulations contained the complete distributions of the EOF velocity, electrical potential, number concentration of each species, as well as surface charge density at the channel walls.

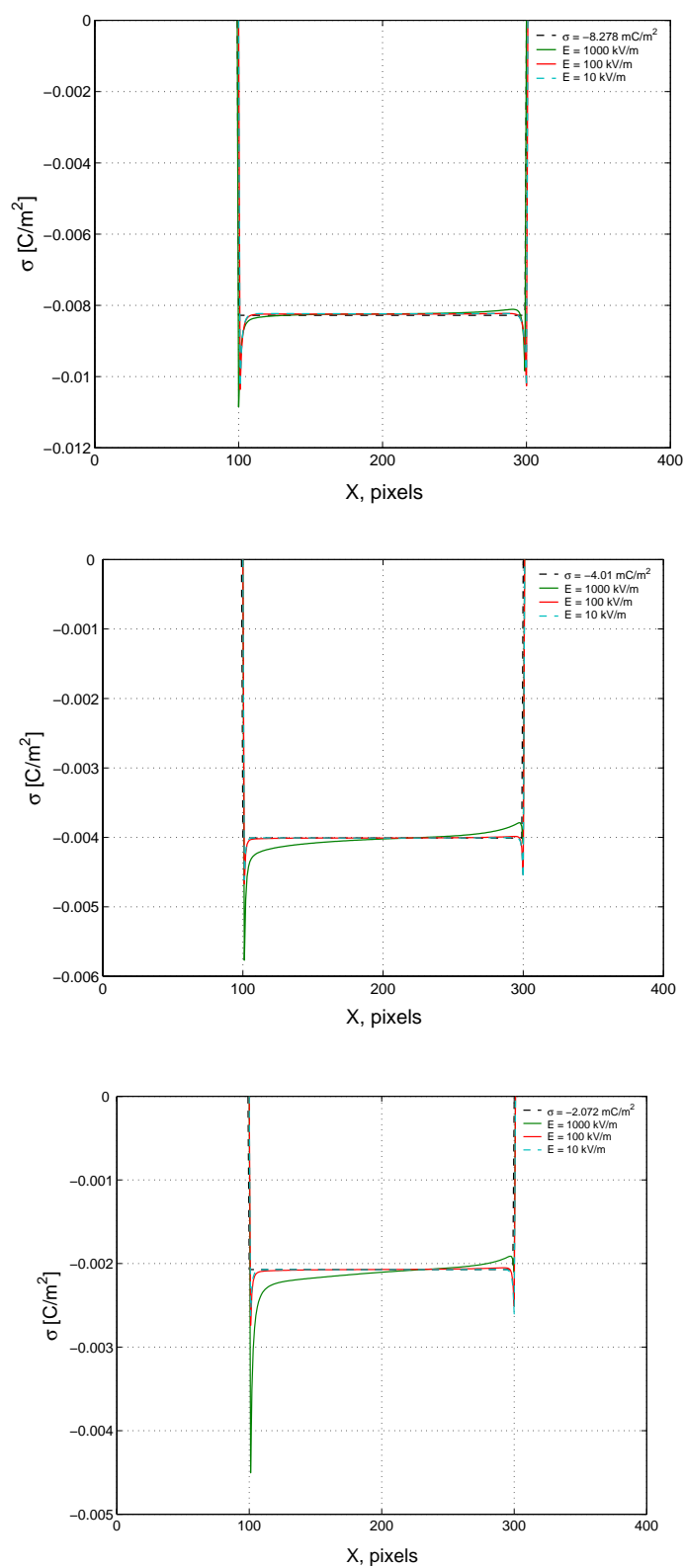


**Figure 4.15.** Distributions of the variable surface charge density along the channel wall for different values of the applied electric field (colour lines) compared to the case of non-variable charge density (black line). The electrolyte concentration is 10 mM (top), 1.0 mM (middle), and 0.1 mM (bottom). The applied electric field is directed from left to right, pH = 5.0.

We start from the analysis of the surface charge distributions, since this quantity is immediately related to the electrokinetic characteristics of any microfluidic system. In Figure 4.15 the surface charge density distributions along the axial direction for different values of electrolyte concentration and applied electric field are shown. The non-variable charge density cases A and B possess identical piece-wise constant distributions with step changes at positions 100 and 300 pixels. The magnitude of  $\sigma$  in the middle regions (between pixels 100 and 300) was dependent on only the electrolyte concentration, increasing with the latter in agreement with predictions of the Gouy-Chapman model. Ion transport due to convection and diffusion does not affect the surface charge density. The new condition that

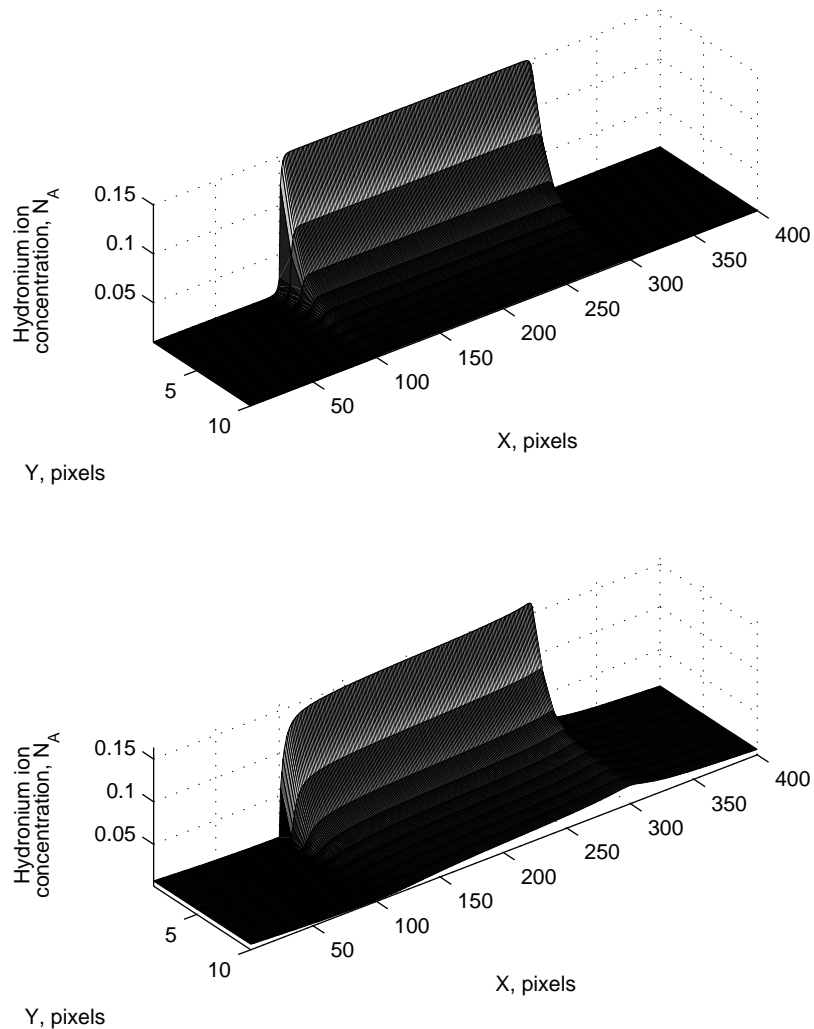


**Figure 4.16.** The hydronium ion concentration (normalized by the Avogadro number,  $N_A = 6.02214 \times 10^{22} \text{ mol}^{-1}$ ) in the near-wall region for the case of variable surface charge density. The electric field is directed from left to right,  $E = 10$  kV/m (top) and 1000 kV/m (bottom),  $c = 0.1$  mM, pH = 5.0.

the surface charge density depends on the local ionic concentration which is affected by convective and diffusive transport changes the picture substantially. Near the locations of the changes in  $\Gamma_{\text{tot}}$  the absolute value of  $\sigma$  sharply increases. This can be explained by the decreased concentration of hydronium ions in the vicinity of the boundary between two different zones of the wall. Hydronium ions diffuse from the EDL region adjacent to the zone border toward a neighbouring near-wall region with zero surface charge density. A decrease in the local hydronium ion concentration induces dissociation of surface silanol groups and results in an increasing surface charge density in the boundary regions. The imposition of the external electric field destroyed the symmetry of the above picture, since the induced EOF and associated convective transport deplete additionally the hydronium ion concentration in the upstream (left) EDL boundary region and particularly accumulate hydronium ions in the downstream (right) boundary region. This distribution is proportional to the velocity of the EOF and applied electric field (Fig. 4.16). The contribution of the hydronium ion in the total ion redistribution is inversely proportional to the electrolyte concentrations. In the limit when the liquid phase consists of pure water and the ionic structure is represented only by hydronium and hydroxyl ions, the above distribution effect will be most pronounced. Therefore, the strongest differences between the left and right boundary regions in Figure 4.15 are realized with the lowest electrolyte concentration (bottom figure).

The distinctions in the surface charge distributions corresponding to cases A, B, and C result properly in different EOF velocities. Table 4.1 contains a summary of the comparison of EOF velocity fields computed for various electrolyte concentrations and external applied electric fields between cases A and C, as well as B and C. The analysed quantities were the root-mean-square axial, transversal and absolute velocities,  $\langle |v_x| \rangle$ ,  $\langle |v_y| \rangle$  and  $\langle |v| \rangle = \langle (v_x^2 + v_y^2)^{1/2} \rangle$ , respectively, as well as their variances,  $\sigma_{v_x}^2$ ,  $\sigma_{v_y}^2$ , and  $\sigma_v^2$ . The latter three quantities characterise the nonuniformity of the velocity field and can be related to hydrodynamic dispersion. All tabulated quantities were normalized by the value of the corresponding quantity for case C, e.g., the table cell marked off by the grey colour contains the following value

$$\left| 1 - \frac{\langle v_x^A \rangle}{\langle v_x^C \rangle} \right|,$$

where  $\langle v_x^A \rangle$  and  $\langle v_x^C \rangle$  denote the root-mean-square axial velocities for cases A and C, respectively.

**Table 4.1.** Relative differences in EOF velocity fields between cases A and C, and B and C.

**c = 10 mM**

	<b>E<sub>ext</sub> = 1000 kV/m</b>		<b>E<sub>ext</sub> = 100 kV/m</b>		<b>E<sub>ext</sub> = 10 kV/m</b>	
	Equilibrium EDL (case A)	Non-variable charge density (case B)	Equilibrium EDL (case A)	Non-variable charge density (case B)	Equilibrium EDL (case A)	Non-variable charge density (case B)
$\langle  v_x  \rangle$	0.033	0.011	0.009	0.012	0.047	0.016
$\langle  v_y  \rangle$	0.024	0.020	0.008	0.048	0.196	0.033
$\langle  v  \rangle$	0.033	0.011	0.009	0.012	0.040	0.016
$\sigma_{vx}^2$	0.025	0.019	0.009	0.026	0.116	0.005
$\sigma_{vy}^2$	0.043	0.020	0.015	0.007	0.099	0.050
$\sigma_v^2$	0.025	0.019	0.009	0.026	0.113	0.005

**c = 1 mM**

	<b>E<sub>ext</sub> = 1000 kV/m</b>		<b>E<sub>ext</sub> = 100 kV/m</b>		<b>E<sub>ext</sub> = 10 kV/m</b>	
	Equilibrium EDL (case A)	Non-variable charge density (case B)	Equilibrium EDL (case A)	Non-variable charge density (case B)	Equilibrium EDL (case A)	Non-variable charge density (case B)
$\langle  v_x  \rangle$	0.120	0.023	0.002	0.003	0.009	0.008
$\langle  v_y  \rangle$	0.069	0.016	0.013	0.003	0.011	0.020
$\langle  v  \rangle$	0.116	0.023	0.003	0.003	0.009	0.008
$\sigma_{vx}^2$	0.063	0.005	0.017	0.004	0.007	0.010
$\sigma_{vy}^2$	0.143	0.004	0.032	0.006	0.035	0.020
$\sigma_v^2$	0.066	0.008	0.016	0.004	0.007	0.010

**c = 0.1 mM**

	<b>E<sub>ext</sub> = 1000 kV/m</b>		<b>E<sub>ext</sub> = 100 kV/m</b>		<b>E<sub>ext</sub> = 10 kV/m</b>	
	Equilibrium EDL (case A)	Non-variable charge density (case B)	Equilibrium EDL (case A)	Non-variable charge density (case B)	Equilibrium EDL (case A)	Non-variable charge density (case B)
$\langle  v_x  \rangle$	0.482	0.035	0.070	0.001	0.063	0.008
$\langle  v_y  \rangle$	0.454	0.012	0.076	0.002	0.050	0.021
$\langle  v  \rangle$	0.481	0.035	0.070	0.001	0.063	0.008
$\sigma_{vx}^2$	0.222	0.006	0.080	0.002	0.063	0.026
$\sigma_{vy}^2$	0.404	0.057	0.123	0.000	0.106	0.017
$\sigma_v^2$	0.225	0.009	0.079	0.002	0.063	0.025

As it was expected, the largest relative differences between cases A and C for all analysed quantities occurred with the lowest electrolyte concentration, 0.1 mM, and the strongest electric field. This fact agrees with the conclusions made after analysis of the differences in surface charge distributions. A similar picture was found for relative differences between the quantities simulated for cases B and C, except for a smaller magnitude of these differences. While the largest relative

distinction between cases A and C has reached almost 50%, the corresponding maximum during comparison between cases B and C did not exceed 6%.

Besides the integral estimation of relative differences between EOF fields simulated according to different approaches, an analysis of the spatial distribution of these differences was carried out. For each pair of the velocity fields (A-C and B-C) the following relative difference field was computed

$$\delta = \left| 1 - \frac{\Theta_{\alpha}}{\Theta_C} \right|, \quad \alpha = \text{A or B},$$

where  $\Theta$  represents axial, transversal or absolute velocity. In Figures 4.17-4.19 the colour maps of  $\delta$ -fields computed concerning  $v_x$  for different values of  $c$  and  $E_{\text{ext}}$  are shown. In general, these maps contain information concerning the divergence between solution for the EOF problem obtained by the different approaches. It is evident that the location of the largest discrepancies between results obtained by different approaches is mainly associated with the near-wall regions in the vicinity to the location of the change in the surface charge density. However, when  $c = 0.1$  mM and  $E_{\text{ext}} = 1000$  kV/m the solutions obtained by different approaches demonstrate significant distinctions even for the bulk region. Overall discrepancy decreases with the increase of the electrolyte concentration that can be again explained by reduction of the hydronium ion contribution in the general picture of ion redistribution caused by non-equilibrium convective and diffusive ionic transport. Surprisingly, when the applied electric field is relatively weak ( $E_{\text{ext}} = 10$  kV/m) the equilibrium EDL approach (case A) gives a smaller divergence of the axial velocity with the variable surface charge density approach (case C) compared to the pair B-C. For the stronger field, results obtained by the non-variable and variable surface charge density (cases B and C) become more similar.

The results of the simulations demonstrate that the EOF in heterogeneous microchannels can be affected by the changes in the surface charge density caused by local variations in the physicochemical properties of a liquid electrolyte, for instance, when surface charge is formed by dissociation of surface silanol groups and depends on the local hydronium ion concentration. This effect becomes more significant at lower electrolyte concentrations, when the hydronium ions have a more important contribution in the total ionic structure of the solution. Since the problem of the analytical estimation of errors associated with the ignorance of surface charge density modifications seems to remain unresolved also in the near future, the numerical simulations of the EOF taking into account the possibility of

having variable boundary conditions is the only way to reach a more satisfactory information concerning the actual velocity distributions in view of the design of electrokinetic microfluidic systems.

In summary, the results of simulations (Fig. 4.17-4.19) indicate that solution of the EOF problem in heterogeneous systems has to be performed considering the possibility of variations in the surface charge density at the solid surface. For instance, the dissociation rate of surface silanol groups at the silica-water (aqueous solution) interface and, as a consequence, the surface charge density is affected by the local value of the pH which, in turn, depends on the EOF. Mathematically this is expressed as an interdependence of the EOF and electrical boundary conditions. The developed numerical method allows to quantify the discrepancy between the EOF velocity fields obtained by the different theoretical approaches in order to optimise the computational expenses for the required numerical accuracy.

The two last sections of this thesis will concern the modelling of electroosmotic and hydraulic flows through regular and random packings of spherical particles which can be considered as a geometrical model of fixed beds, e.g., encountered in chromatographic capillary columns.



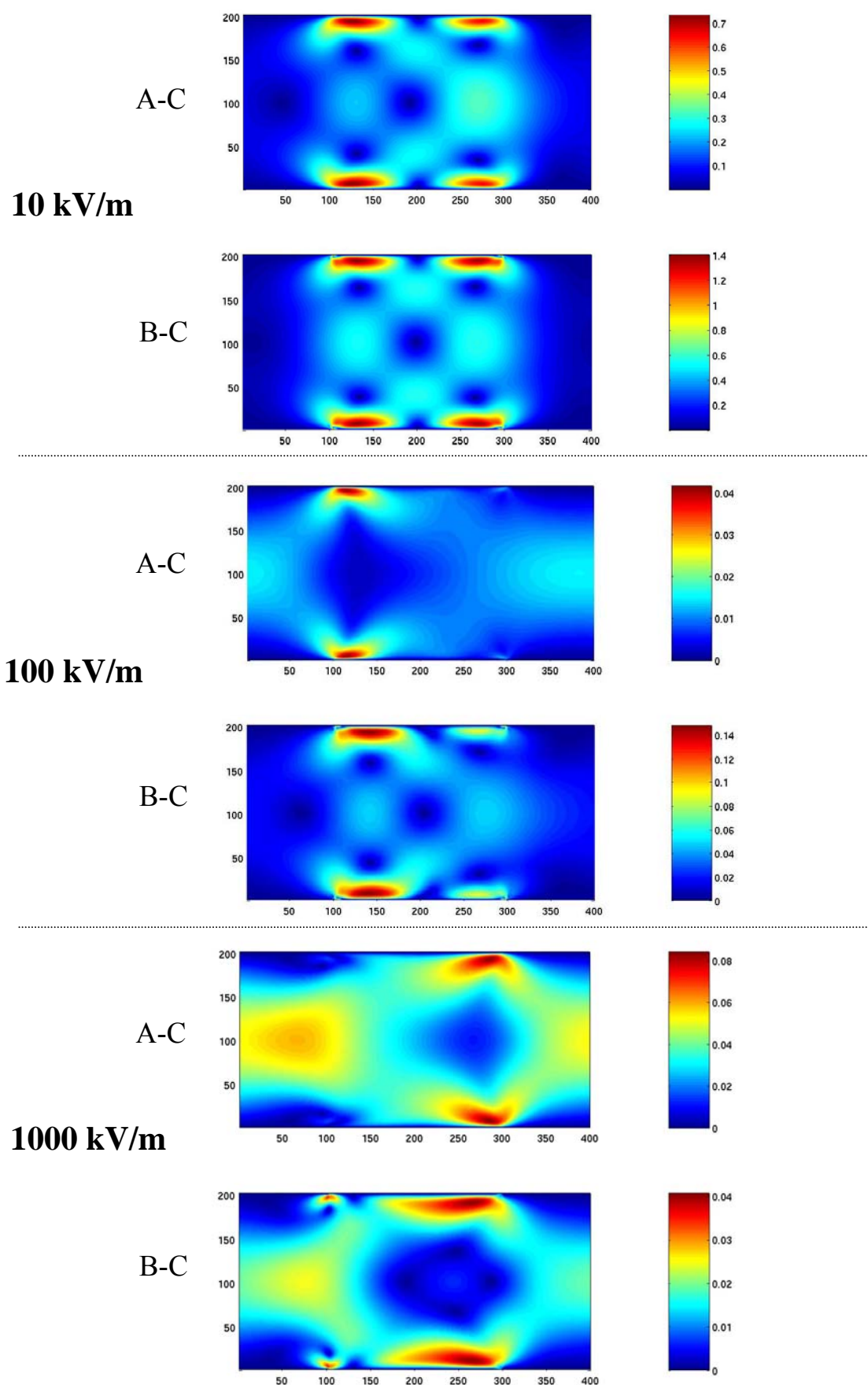


*Figure 4.17.* Color map of the  $\delta$ -field computed for the axial component of the EOF velocity,  $c = 10$  mM and  $\text{pH} = 5.0$ . The electric field is directed from left to right.

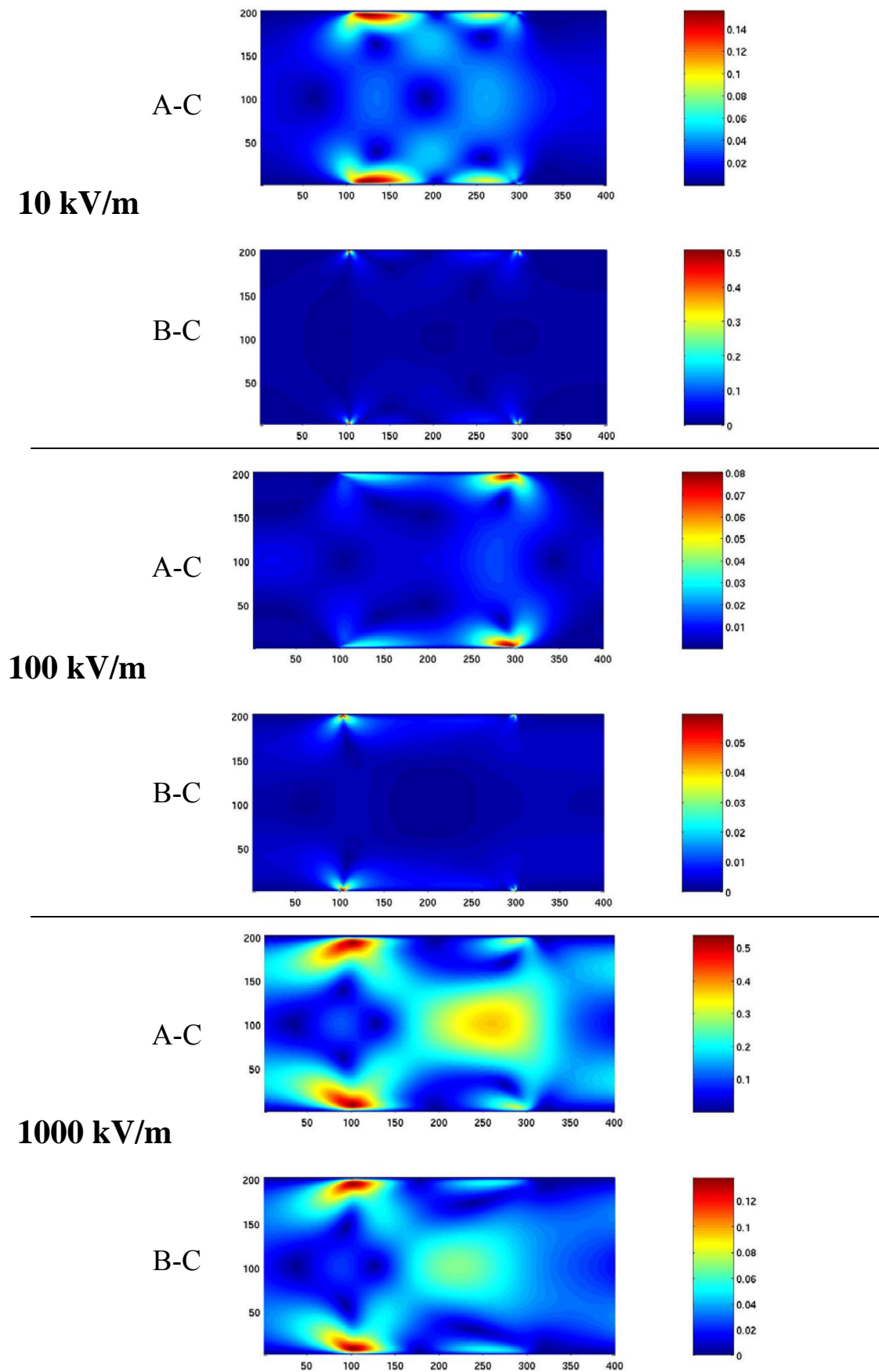


**Figure 4.18.** Color map of the  $\delta$ -field computed for the axial component of the EOF velocity,  $c = 1.0$  mM and pH = 5.0. Electric field is directed from left to right.

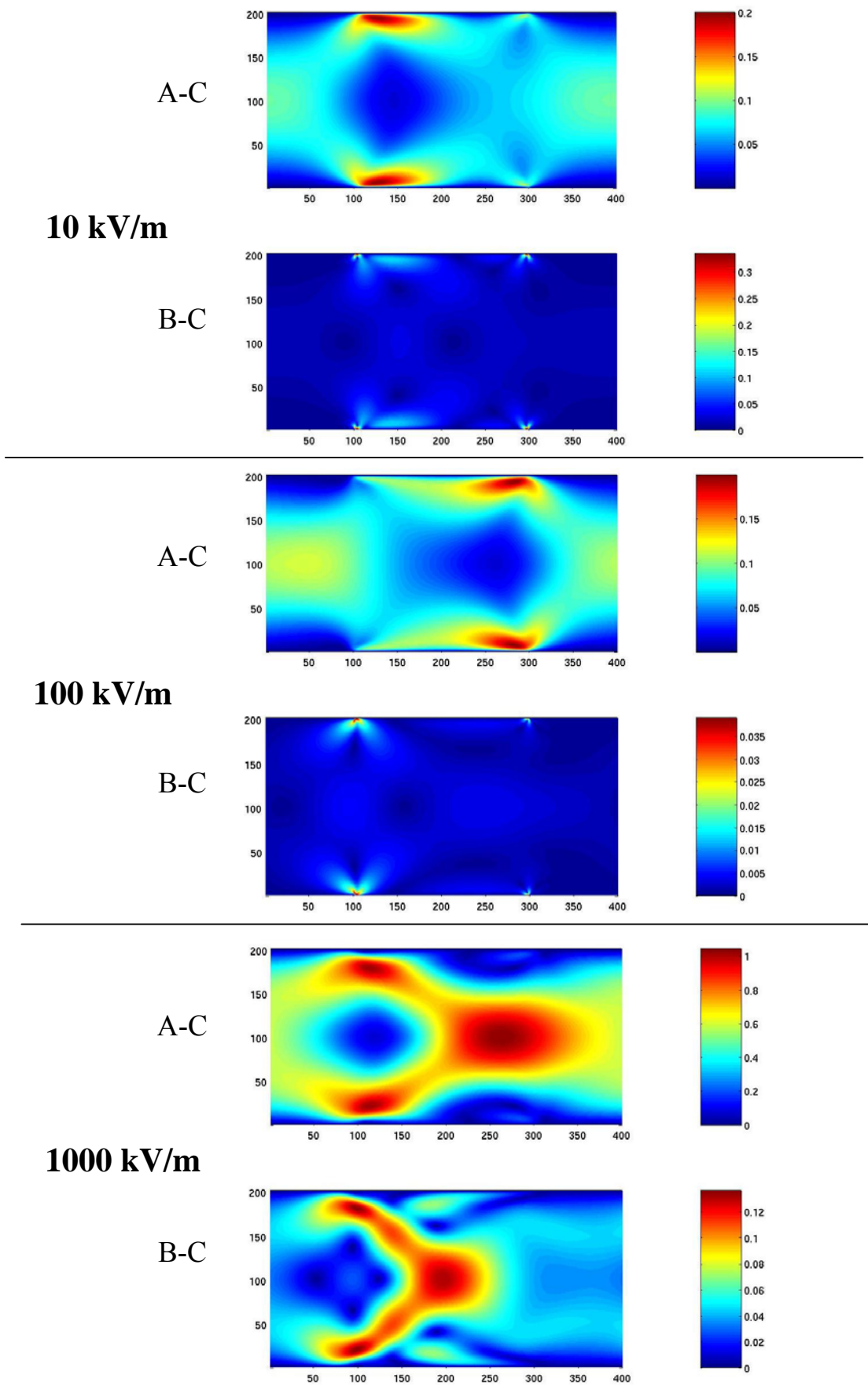


*Figure 4.19.* Color map of the  $\delta$ -field computed for the axial component of the EOF velocity,  $c = 0.1$  mM and  $\text{pH} = 5.0$ . Electric field is directed from left to right.



### 4.3. Numerical simulation of electrokinetic microfluidics in colloidal systems\*

A numerical scheme for simulating electrokinetic microfluidics in systems with an arbitrary geometry is developed. This scheme is based on numerical solution of the coupled Poisson, Nernst-Planck, and Navier-Stokes equations. While traditional finite difference methods are used to resolve the first two problems, the lattice-Boltzmann method is applied to the latter. The developed numerical scheme has been applied to computer simulations of electroosmotic flow through a simple-cubic array of micro-sized hard spheres. Volumetric electroosmotic flow has been studied as a function of the applied electrical field,  $\zeta$ -potential of the sphere surface, and ionic strength. The investigation of colloidal stability and the electrokinetics in microchip devices containing fixed bed segments (particulate or monolithic structures) represent two potential applications of this work.

#### 4.3.1. Introduction

Electrokinetic microfluidic phenomena are currently of fundamental and practical interest in various fields of science and engineering. This interest is stimulated, on one hand, by rapid recent developments in microfabrication technologies and, on the other hand, by the fact that electrokinetic transport can offer distinct advantages over pressure-driven flow, e.g., reduced hydrodynamic dispersion and mass transfer resistance, as the characteristic dimensions of devices decrease to (sub)micrometer dimensions. One of the important applications of electrokinetic transport is capillary electrochromatography (CEC), where electroosmotic flow (EOF) is used as a mechanism for transporting solvent and solutes through a chromatographic column. Compared to pressure-driven liquid chromatography, CEC can provide substantially higher separation efficiency. This feature mainly results from i) the absence of applied pressure drop, allowing to use of very small particles packed in the chromatographic (capillary) columns and so to increase the total separation performance, and ii) reduced hydrodynamic dispersion, that decreases chromatographic band broadening.

---

\* This section is based on the following publication:

D. Hlushkou, D. Kandhai, A. Seidel-Morgenstern, and U. Tallarek, *Simulation of Electrokinetic Microfluidics in Colloidal Systems*, Proc. AIChE Annual Meeting 2003, San Francisco, CA, USA, November 16-21.

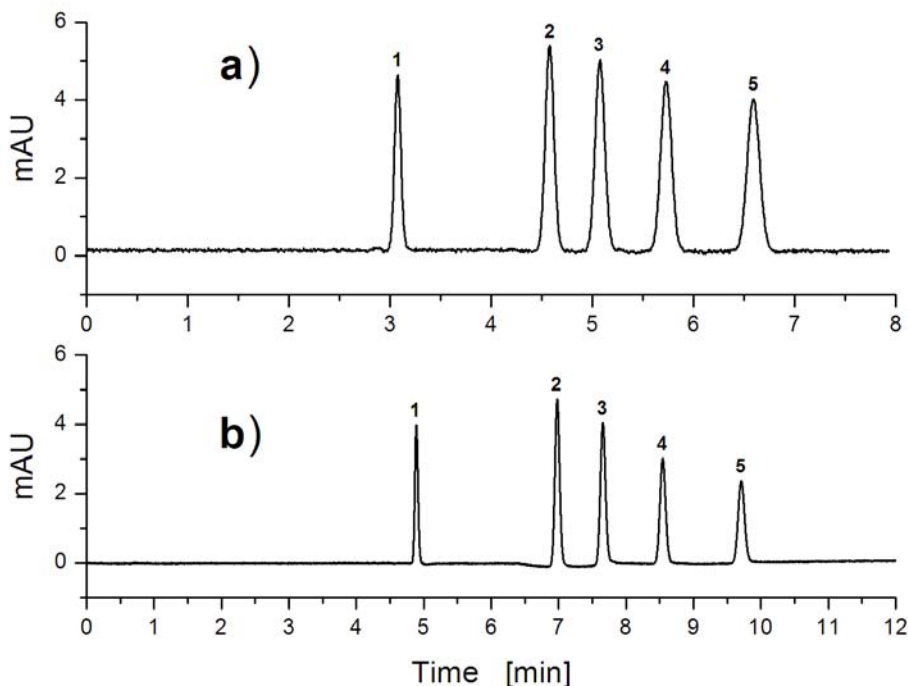


**Figure 4.20.** Separation efficiency at similar mobile phase average velocity. a) Capillary HPLC, packed bed of 150 mm length in a 100  $\mu\text{m}$  i.d. capillary, in-column detection (215 nm); analytes: (1) thiourea, (2) methylbenzoate, (3) ethylbenzoate, (4) propylbenzoate, and (5) butylbenzoate. b) CEC, 325 mm long capillary setup (effective packed bed length of 240 mm)  $\times$  100  $\mu\text{m}$  i.d., applied voltage: 20 kV. Stationary phase: Porous C18-silica particles ( $d_p = 2.45 \mu\text{m}$  and  $d_{\text{pore}} = 14 \text{ nm}$ ). The mobile phase is a 5 mM aqueous Tris (pH-8.3)/acetonitrile 20:80 (v/v) buffer solution. The separation efficiency in CEC is about  $2 \times 10^4 N_{\text{pl}}/\text{m}$ .

Figure 4.20 illustrates the difference between two chromatograms obtained experimentally during the separation process for the same sample and similar Peclet-number but with (a) pressure-driven and (b) electroosmotic flows. The narrower peaks in the second chromatogram indicate the possibility to perform the analysis at higher resolving power translating it to an increased sensitivity and lower operation costs. The efficiency in Fig. 4.20 can be estimated by the number of theoretical plates,  $N_{\text{pl}}$  determined by the following expression [94]

$$N_{\text{pl}} = \left( \frac{2.354 t_r}{\sigma} \right)^2,$$

where  $t_r$  and  $\sigma$  are the retention time and width at half-height of the corresponding chromatographic peak, respectively. As the data in the figure indicate, the efficiency of the electrochromatographic analysis is several times higher than of that obtained with pressure-

driven flow. Since packed chromatographic columns can be represented by an open capillary packed with spherical particles, the computer simulation of EOF through colloidal structures can provide complementary insight into the complex transport processes within such devices.

#### 4.3.2. Mathematical model and implementation

The general mathematical description of the steady-state electrokinetic transport problem in an  $N$ -component incompressible electrolyte consists of the set of coupled Nernst-Planck, Navier-Stokes, and Poisson equations

$$\mathbf{v}\nabla n_i - D_i\nabla^2 n_i - \frac{q_e z_i D_i}{k_B T} \nabla \cdot (n_i \nabla \Phi) = 0, \quad (4.73)$$

$$\rho_f (\mathbf{v} \cdot \nabla) \mathbf{v} = -\nabla p + \eta \nabla^2 \mathbf{v} - q_e \nabla \Phi \sum_{i=1}^N z_i n_i, \quad (4.74)$$

$$\nabla^2 \Phi = -q_e \sum_{i=1}^N z_i n_i / \epsilon_0 \epsilon_r, \quad (4.75)$$

where  $\mathbf{v}$  represents the divergence-free velocity field ( $\nabla \cdot \mathbf{v} = 0$ );  $\rho_f$ ,  $\eta$ ,  $p$ ,  $\epsilon_0$  and  $\epsilon_r$  denote the density of the fluid, its dynamic viscosity, hydrostatic pressure, the permittivity of vacuum and relative permittivity, respectively,  $n_i$ ,  $D_i$ ,  $z_i$  are the number concentration, diffusion coefficient and valency of ionic species  $i$ , respectively;  $\Phi$  is the local electrical potential,  $q_e$ ,  $k_B$  and  $T$  represent the elementary charge, Boltzmann constant and temperature, respectively. An iterative numerical scheme was developed for solving the aforementioned set of Eqs. 4.73-4.75 subject to the following boundary conditions (see Section 4.1)

$$\mathbf{j}_i \cdot \bar{\mathbf{v}} = 0, \mathbf{v} = 0, \Phi = \zeta + \phi \quad \text{at the solid-liquid interface,} \quad (4.76)$$

where  $\mathbf{j}_i$  and  $\bar{\mathbf{v}}$  are the flux density and the normal to the interface, respectively.  $\zeta$  and  $\phi$  represent the electrical potential contributions due to the surface charge at the solid-liquid interface and applied external electric field. It should be pointed out that the presented electric boundary condition assumes negligible ion-convective effects on the  $\zeta$ -potential distribution as compared to ion-diffusion or small perturbations with respect to the equilibrium state.

At each iteration the coupled Nernst-Planck, Poisson, and Navier-Stokes equations are solved by turns using a uniform cubic lattice. While conventional finite difference methods have been employed to resolve the first two problems, the lattice-Boltzmann algorithm has been applied for solution of the latter. This allowed to treat this hydrodynamic problem with high computational efficiency for systems characterized by a complex solid-liquid interface.

#### 4.3.3. Results of simulation

The implementation of the presented numerical scheme has been performed at a parallel computer (Hewlett-Packard Superdome). A number of EOF simulations for various capillary and colloidal systems has been carried out.

Initially, this computer model was tested by calculating the electric charge distribution around a single sphere immersed in an electrolyte solution. The charge distribution determines the electromotive forces which act on a liquid leading to the specific fluid velocity distribution. The simulated charge density distribution in a symmetric 1:1 electrolyte has been compared (Fig. 4.21) with the data of Loeb, Overbeek, and Wiersema, the so-called LOW-tables [95], which contain the results of a one-dimensional numerical solution for the Poisson-Boltzmann equation describing, in particular, the equilibrium distributions of the net electrical charge for a single sphere system of radius  $r_s$ . This comparison demonstrates good agreement between the two sets of data over a wide range of the net charge magnitude.

In the next step, we simulated the EOF through a simple cubic (SC) array of spheres. Although real packed chromatographic columns are represented more realistically by random sphere packings, we have chosen the regular structure in order to eliminate any effects related to the random nature of the medium model and to investigate clearly the relationship between simulated mean velocity and experimental conditions, for instance,  $\zeta$ -potential, ionic strength, and applied electric field  $E_{\text{ext}}$ . As it was mentioned above, we have assumed that the  $\zeta$ -potential is not affected by the applied electric field or liquid convection. A collection of EOF simulations has been carried out for various values of  $\zeta$ -potential, applied electric field, computational grid resolutions and aspect ratio  $\alpha$  (concerning sphere diameter to electric double layer thickness  $\lambda_D$ ), that can be easily translated to any ionic strength. All values of variable quantities which have been used in the aforementioned collection of simulations are given in Table 4.2. The complete collection consists of 512 simulations.



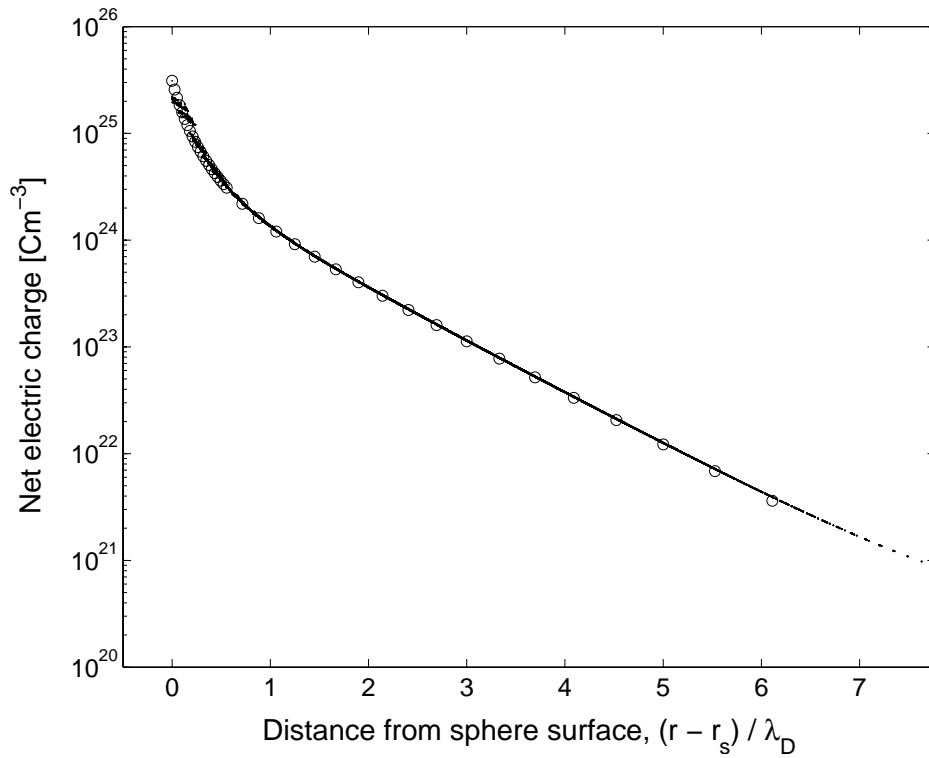


**Figure 4.21.** Point-wise comparison of the simulated electric charge distribution around a single sphere (•) with the data of Loeb, Overbeek, and Wiersema (LOW-tables) [95] (○) for a 1:1 electrolyte.  $\zeta = -102.77$  mV, the aspect ratio of sphere diameter to electric double layer thickness  $d_s/\lambda_D = 10$ , bulk concentration  $n_\infty = 5.678 \times 10^{23} \text{ m}^{-3}$ .

**Table 4.2.** The values of variable parameters used in the simulations

$\zeta$ , mV	-25.69, -51.39, -77.07, -102.77
$E_{\text{ext}}$ , kV/m	10, 25, 50, 100
Aspect ratio, $\alpha = d_s / \lambda_D$	2.272, 22.72, 50, 100
Grid resolution (points per sphere diameter), $\beta$	25, 30, 40, 50, 75, 100, 150, 200

The lowest value of employed  $\zeta$ -potential ( $-25.69 \text{ mV} = k_B T / q_e$ ) corresponds to the upper limit for the conventional use of the Debye-Hückel approximation, while the highest value ( $-102.77 \text{ mV} = 4k_B / q_e$ ) can be considered as the upper limit of  $\zeta$ -potential for many realistic solid-liquid interfaces. The smallest value of  $\alpha$  implies an overlap of EDL's of neighbouring spheres over a quite extended area, while in the case of  $\alpha = 100$  this overlap is relatively small.

The mean velocity of electroosmotic flow in the direction of the applied electric field was calculated for each set of variable parameters. Since there is no analytical solution and only a few results of other numerical simulations are published concerning EOF through a SC array that could be used for comparison the convergence of the mean velocity by further refinement of the computational grid was considered as sufficient proof of the computational accuracy. A brief presentation of the information contained in the complete collection is difficult, therefore only some results will be provided in this paper.

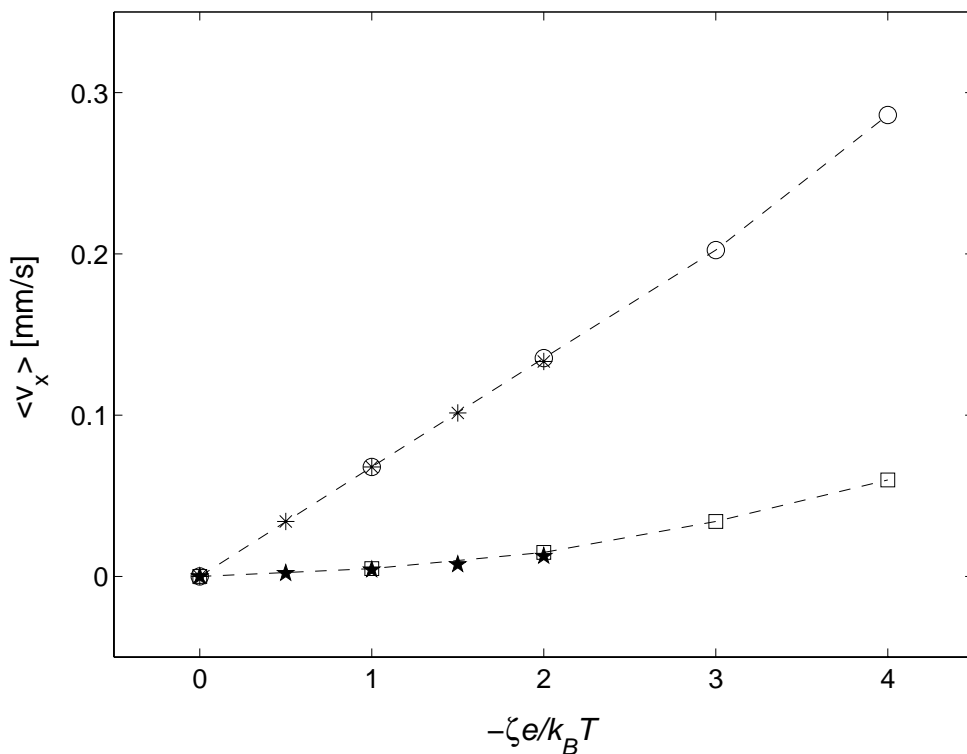


**Figure 4.22.** Point-wise comparison of simulated (○ and □) mean EOF velocities through SC array of spheres with published data in Ref. [62] (\* and ★).  $\alpha = 2.272$  for the lower data sets and 22.72 for the upper data sets,  $E_{\text{ext}} = 10 \text{ kV/m}$ ,  $\beta = 200$ .

First, we compared the simulated mean longitudinal velocity with that obtained by Coelho et al. [62]. They developed a model of electrokinetic phenomena in finely dispersed porous media under the assumptions of low  $\zeta$ -potential and small perturbations from the equilibrium state and simulated EOF, in particular, through SC array of spheres. The biggest absolute values of  $\zeta$  and aspect ratio,  $\alpha$ , in their simulations were 51.385 mV and 22.72, respectively. Figure 4.22 indicates good agreement between our simulated data and the results presented in Ref. [62].

Then, we carried out an analysis of discretization effects on the simulated velocity. Its dependence on the computational grid resolution for  $E_{\text{ext}} = 10$  kV/m and two limiting values of the  $\zeta$ -potential,  $\zeta = -25.69$  and  $\zeta = -102.77$  mV, is shown in Figure 4.23. While for  $\zeta = -25.69$  mV mean velocity decreases monotonically and independent of the aspect ratio  $\alpha$  toward some asymptotic value at finer resolutions, the velocity behaviour is quite different for small and large values of  $\alpha$  when  $\zeta = -102.77$  mV. The dip at coarser resolution for the larger values of  $\alpha$  can be explained by the error in the simulation of electrical charge distribution. The net electric charge demonstrates its locally highest density at the solid-liquid interface and then decays to zero in the bulk region. When the spatial discretization step is large with respect to the EDL thickness, even the grid point closest to the solid-liquid interface is located in a region of a relatively low electric charge density. Thus, the electromotive force is underestimated and the overall EOF is reduced. The total computational time varied from approximately 160 processor $\times$ hours ( $\beta = 200$ ) up to few processor $\times$ milliseconds ( $\beta = 25$ ).

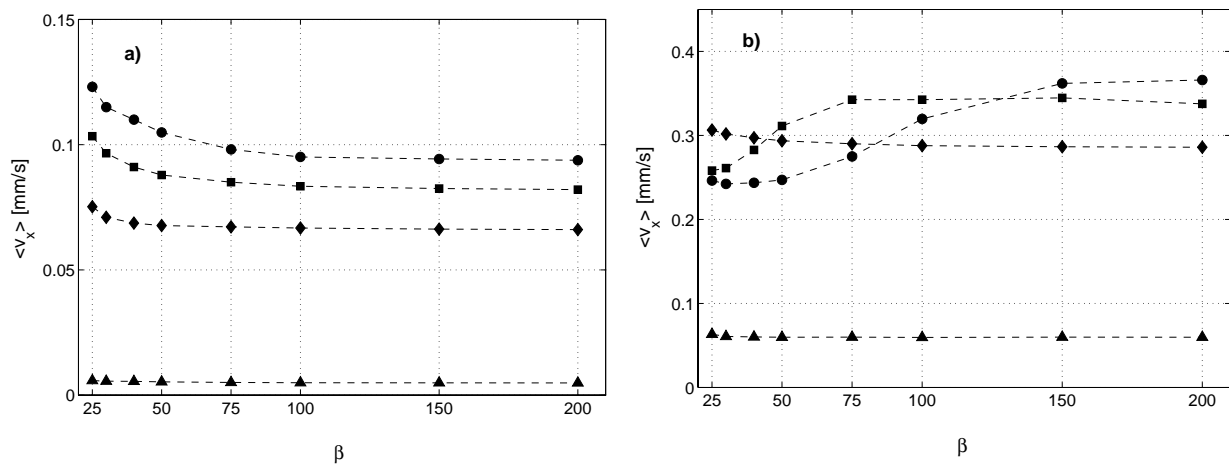


**Figure 4.23.** The mean longitudinal velocity of EOF through SC-array of spheres as a function of the computational grid resolution  $\beta$ .  $E_{\text{ext}} = 10$  kV/m,  $\zeta = -25.69$  mV (a) and  $-102.77$  mV (b),  $\alpha = 2.272$  (▲),  $22.72$  (◆),  $50$  (■) and  $100$  (●).

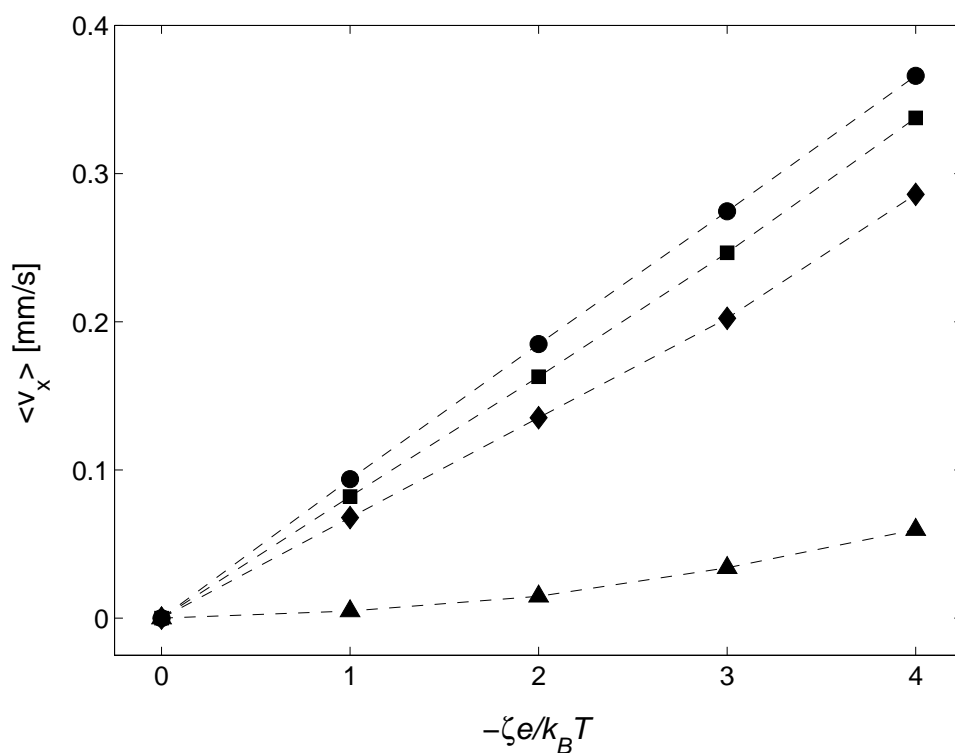


**Figure 4.24.** Simulated mean velocity as a function of  $\zeta$ -potential.  $E_{\text{ext}} = 10$  kV/m,  $\alpha = 2.272$  (▲), 22.72 (◆), 50 (■) and 100 (●),  $\beta = 200$ .

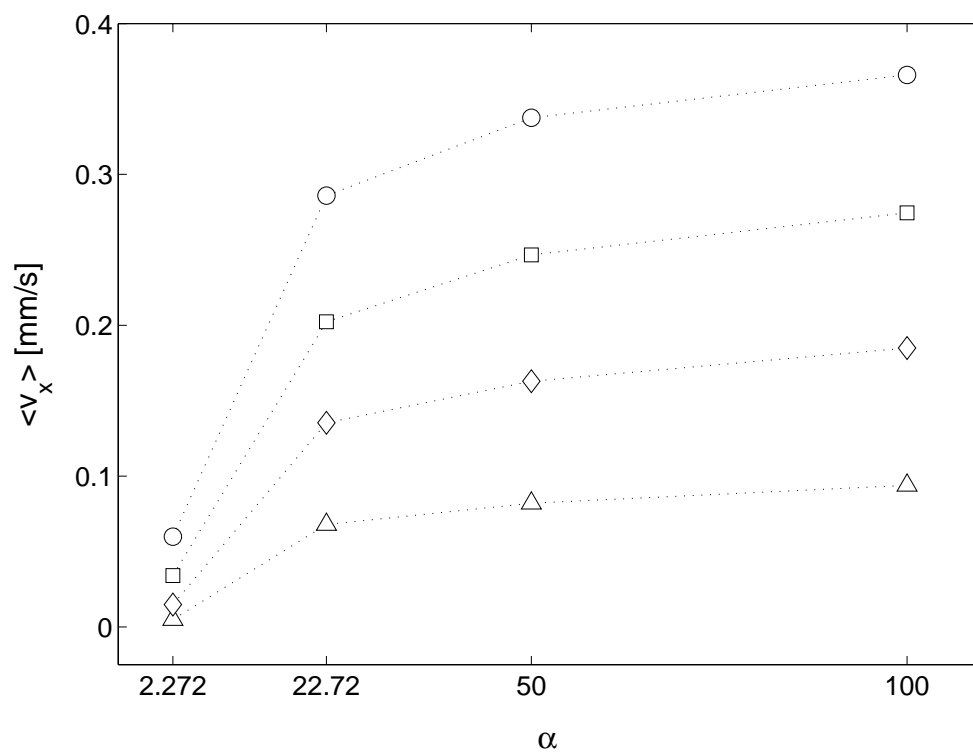


**Figure 4.25.** Simulated mean velocity as a function of  $\alpha$ .  $E_{\text{ext}} = 10$  kV/m,  $\zeta = -25.69$  mV (▲),  $-51.385$  mV (◆),  $-75.07$  mV (□) and  $-102.77$  mV (○),  $\beta = 200$ .

The effect of the value of the  $\zeta$ -potential on the simulated velocity is illustrated in Figure 4.24. With increasing aspect ratio  $\alpha$  the relation between mean velocity and  $\zeta$ -potential tends towards linear behaviour. This observation agrees with the “so-called” thin double layer (TDL) approximation when the electroosmotic (“slip”) velocity can be defined by the Helmholtz-Smoluchowski equation (Eq. 4.36) with a linear dependence on  $\zeta$ -potential. The behaviour of the simulated mean velocity with changing aspect ratio (see Fig. 4.25) for different  $\zeta$ -potentials can be explained along the same lines. The mean EOF velocity becomes unaffected by  $\alpha$  and tends to dependent on only the  $\zeta$ -potential (if the all other parameters are fixed) at the larger aspect ratio that is in agreement with the TDL approximation.

Finally, the dependence of simulated mean velocity on applied electric field has been examined. In Figure 4.26 the data for  $\zeta = -25.69$  mV are presented. The relation between electroosmotic velocity and applied electric field is practically linear for any value of  $\alpha$ . Moreover, the effect of “saturation” (when the electroosmotic velocity ceases to vary with the further increasing aspect ratio) is observed for each value of applied electric field. This

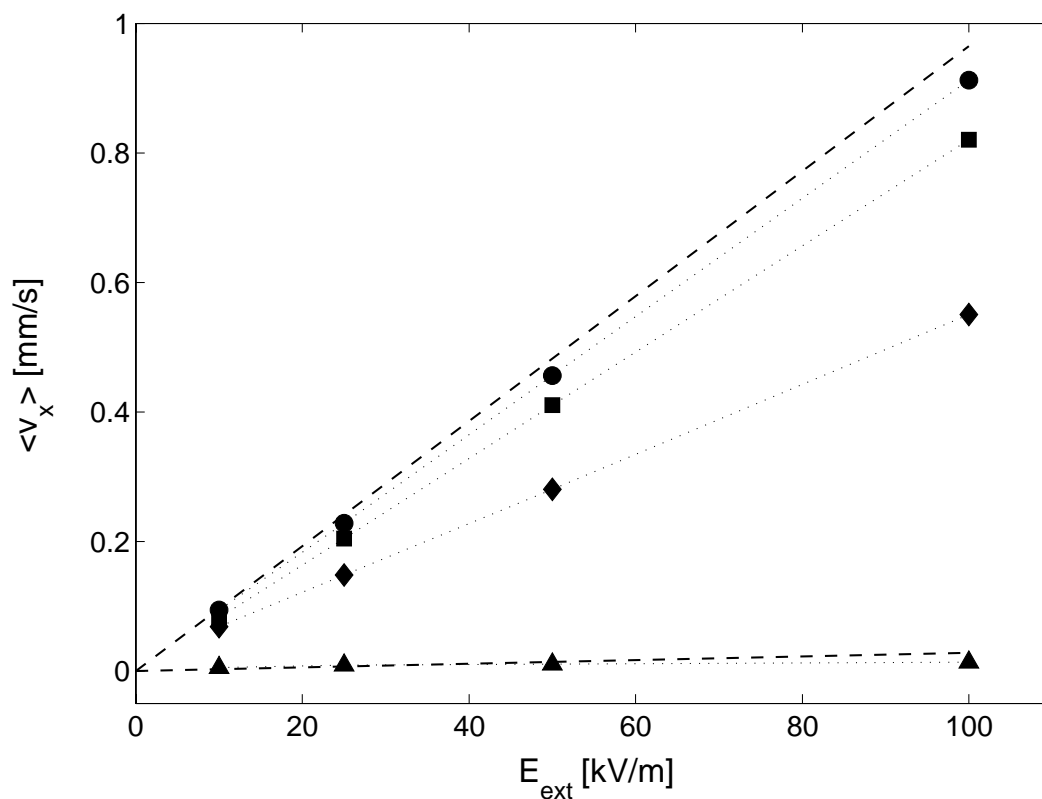


**Figure 4.26.** Simulated mean velocity as a function of  $E_{ext}$ ,  $\zeta = -25.69$  mV,  $\alpha = 2.272$  ( $\blacktriangle$ ), 22.72 ( $\blacklozenge$ ), 50 ( $\blacksquare$ ) and 100 ( $\bullet$ ),  $\beta = 200$ . The dotted lines correspond to the linear approximation of our simulated data, the dashed lines represent results obtained by the capillary model for  $\alpha = 2.272$  (bottom) and 100 (top).

corroborates the validity of the representation of a porous medium as an assembly of parallel cylindrical microcapillaries (the so-called “capillary model”) [8]. The actual sinuous nature of a porous medium can be accounted for by the introduction of the tortuosity  $\Upsilon$ . According with that approach, the mean axial EOF velocity through the SC array of spheres can be determined by [10, 167]

$$\langle v_x \rangle = -\frac{\varepsilon_0 \varepsilon_r \zeta E_{\text{ext}}}{\eta \Upsilon^2} \left[ 1 - \frac{2I_1(\kappa d_{\text{pore}})}{\kappa d_{\text{pore}} I_0(\kappa d_{\text{pore}})} \right], \quad (4.77)$$

where  $I_1$  and  $I_0$  are first-order and zero-order modified Bessel function, respectively,  $\kappa$  is the reciprocal of the EDL thickness, and  $d$  is the mean diameter of the pores between the spheres. In Figure 4.26 the results obtained by the above approach for  $\alpha = 2.272$  and 100 are presented by the dashed lines. For those calculation the diameter of sphere inscribed in the throat of the SC array of spheres was utilized as the mean diameter of the pores (i.e.,  $d_{\text{pore}} = 0.414d_s$ ), while the tortuosity factor was defined as the ratio of the diffusion coefficient of the fluid in bulk to the steady-state diffusion coefficient of a fluid in the SC array of spheres (i.e.,  $\Upsilon^2 = 1.918$  [168]). For the both values of  $\alpha$  the mean simulated EOF velocity is slightly underestimated compared to that obtained by the capillary model. This discrepancy can be caused by the not adequate representation of the interstitial pore space between spheres by capillaries with the constant cross-section and (mean) diameter. Obviously, since the representation of a porous medium by a collection of parallel microcapillaries ignores the interconnectivity of an actual pore network, the capillary model is limited to an equality of mean velocities and can become unrealistic if, for instance, hydrodynamic dispersion is evaluated.

#### 4.3.4. Conclusion and outlook

EOF through SC sphere array has been simulated by an iterative numerical solution of the coupled Navier-Stokes, Nernst-Planck and Poisson equations assuming that the  $\zeta$ -potential distribution at the solid-liquid interface is neither affected by convection, nor by the applied electric field. This novel applied combination of two different numerical techniques for the solution of the complex problem has proven to be applicable and reliable. It can be recommended to be used in further studies, including, e.g., random sphere packings.

The collection of simulations of EOF through SC sphere array has been performed for various values of applied electric field,  $\zeta$ -potential and the aspect ratio of sphere diameter to double layer thickness. The dependence of mean electroosmotic velocity on those variable

parameters has been examined and has demonstrated good agreement with a number of frequently used and limiting approximations. At the same time the developed model can assist in resolving difficult problems requiring to hold the complete information concerning the flow velocity distribution in systems with a complex morphology, as in the evaluation of hydrodynamic dispersion in electroosmotic flow through porous media. The obtained data can be used for an optimized spatial resolution in large-scale simulations relative to computational expenses and resulting accuracy.

The possible further development of the presented model can include the dissociation of surface groups or adsorption processes which can be responsible for changes in  $\zeta$ -potential or surface electric charge due to alterations in the local chemical environment caused by convection or electromigration phenomena [73].





## **4.4. Simulation of Transport Phenomena in Porous Media**

### *4.4.1. Computer generation of sphere packings*

A random array of hard spherical particles has long been of interest because of its technological importance and significance in applications throughout science and engineering including colloidal systems, ideal liquids, granular materials, and biological membranes. In particular, random sphere packings are used as a model of many types of porous media. The primary reason for its attractiveness as a model system is that the highly complex topology associated with disorder can be completely described in simple geometric terms, such as the radius and position of each sphere. Chromatographic columns are most frequently packed with spherical or spheroidal particles, therefore random sphere packings can be regarded as a quite adequate representation of various fixed beds. Since it is not simple to obtain a complete geometrical description of real packings, computer generation of such structures can serve as a good and often the only possible alternative.

### *Stratification of computer algorithms for the generation of random sphere packings*

All known sphere packing algorithms can be grouped into two general categories (Fig. 4.27). Sequential-settlement or “rain” algorithms begin with a seed sphere [96-99]. Growth of the packing then occurs by the successive placement of new spheres in accordance with determined rules. As such rules we can use the criterion of minimal total potential energy of the packing in the gravitational field, the presence at least three-point contacts for each sphere, maximum of packing entropy, etc. An example of this algorithm group is the so-called “drop-and-roll” algorithm. It supposes that each sphere is introduced at a random position above the bed of spheres already deposited and is allowed to fall until it reaches the first contact with another sphere or container walls. Then, this sphere can be rolled down on a particle surface until it deposits on a stable location. The generation is finished as soon as the container is full. An advantage of this algorithm type is the high speed of running. But the properties of the generated packing are difficult to control. Moreover, by using this method it is very difficult to create structures with porosity  $\varepsilon$  (ratio of the total void volume to total packing volume) of less than 0.4.

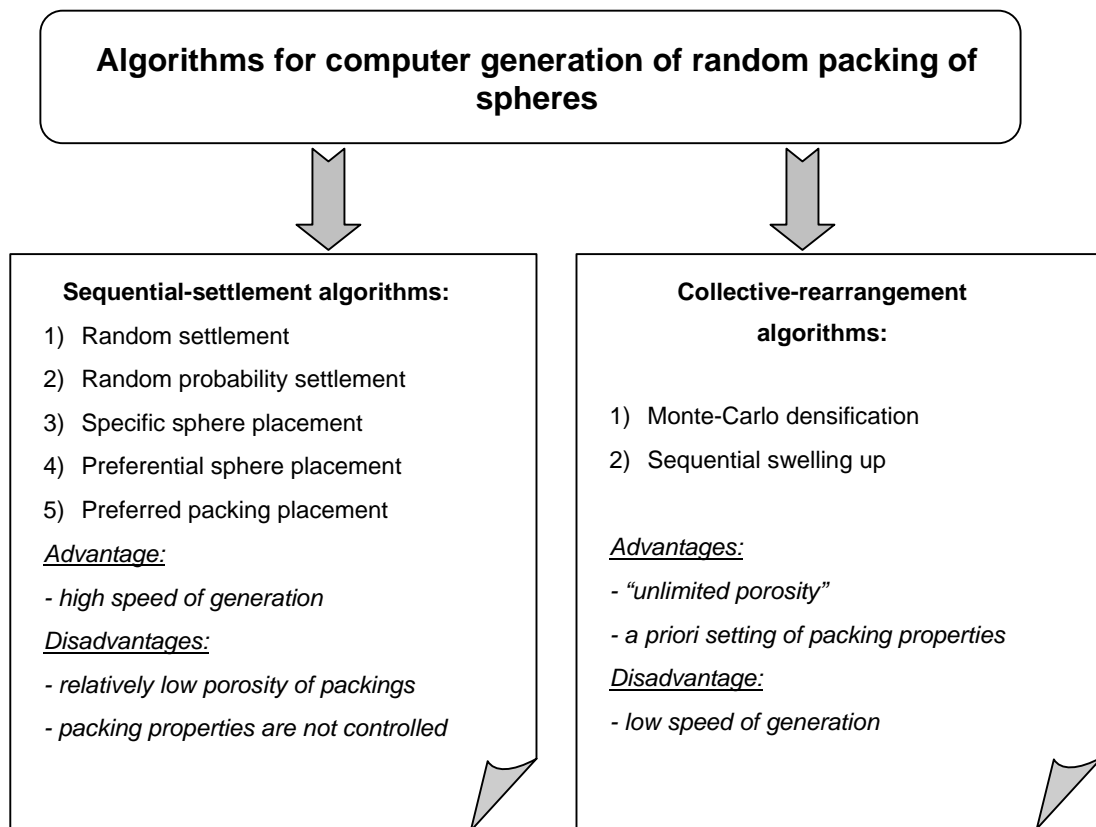


**Figure 4.27.** Schematic classification of computer algorithms for the generation of random sphere packings.

An alternative group is composed of collective rearrangement algorithms. Techniques in which spheres are randomly moved in an effort to either remove overlaps (if spheres are initially overlapped) or decrease porosity (if spheres are initially non-overlapped) are lumped into this category. Typical examples of collective rearrangement methods are the Monte-Carlo densification [100-102] and sequential swelling up [103], or Jodrey-Tory [104] algorithms. The former algorithm starts from an arbitrary "no-overlapping-configuration" of uniformly distributed hard spheres within a confining container. In order to facilitate creation of the starting configuration, the dimensions of the container are on forehand increased relative to the required size of the final packing. Further, at each iterative time step sphere coordinates are randomised and then an attempt is made to decrease the container volume by a small increment. The generation can be finished as the required porosity is reached. In contrast, the Jodrey-Tory algorithm starts from an arbitrary configuration of points uniformly distributed in the container, which corresponds already to the final packing volume. At each iteration a pair of the nearest points is determined and they are spread apart for a certain distance variable through the generation procedure. If one associates points with sphere centres, the distance between two closest points can be considered as a sphere diameter, which ensures a

configuration without overlap. A sequential growth of the sphere diameter provides the decrease of the packing porosity. Advantages of this type of algorithms are the possibility of an *a priori* complete setting of the packing properties and low porosities of generated structures (less than 0.4). However, these methods are more extensive from the point of view of computational time as compared with the first group of algorithms.

#### Modified Jodrey-Tory algorithm

Since packed chromatographic columns (fixed beds) are characterized by a relatively low porosity (commonly less than or of the order of 0.4), the Jodrey-Tory algorithm has been chosen in order to realize an adequate representation of real random-close sphere packings. To reduce the computational expense, which is becoming particularly high for low porosity and large scale packings, the generating algorithm has been implemented as parallel code at a high-performance computer. Analysis of the computational time requirements for different procedures within the Jodrey-Tory algorithm indicates that the determination of the pair of the closest points is most expensive (from the point of view of the required computational time) is. This operation consists of searching the minimal element in a square matrix which represents the distance between each pair of spheres. The parallel implementation of the Jodrey-Tory algorithm divides this matrix into several submatrices. Then, the search of the minimal distance is performed within each submatrix by an individual processor and, finally, the global minimum distance is determined using the smallest element of each submatrix.

Another modification of the original Jodrey-Tory algorithm is due to the specificity of chromatographic columns. The original algorithm deals with the generation of unconfined packings, which assumes the imposition of periodic boundaries. Actual packed columns demonstrate evident inhomogeneities introduced by the presence of (confining) column walls [105]. This structural nonuniformity results in variations of mass transport characteristics in wall regions and must be taken into account to arrive at an adequate representation of transport phenomena. Hence, the generation of confined packings should be considered as an important contribution to the realistic simulation of mass transport through packed chromatographic columns. The adaptation of the original Jodrey-Tory algorithm to the generation of confined random packings was mainly performed by revision of the procedure searching for the minimal element in the distance matrix. The modified algorithm carries out this search not only for each pair of spheres, but as well for the distances between sphere and the container wall. This allows to use a confining container of any arbitrary shape if the latter can be expressed in an analytical form, such as tubular geometry with cylindrical, quadratic,

rectangular, elliptical or trapezoidal cross-section. Figure 4.28 shows two examples of confined packings generated by the presented modification of the Jodrey-Tory algorithm.

One other modification of the original algorithm was stimulated by the necessity to take into account a distribution of sphere diameters. Particles used for the chromatographic column fabrication may possess both discrete (e.g., mono-, bi- or multisized) and continuous (e.g., normal or lognormal) distributions of their diameters. To satisfy this requirement the growth rate of an individual sphere during the generation was set in proportion to its final diameter, which was defined in advance in accordance with a given distribution. In Figure 4.29 two cylindrical packings with bimodal and normal (Gaussian) distribution of sphere diameters are shown.

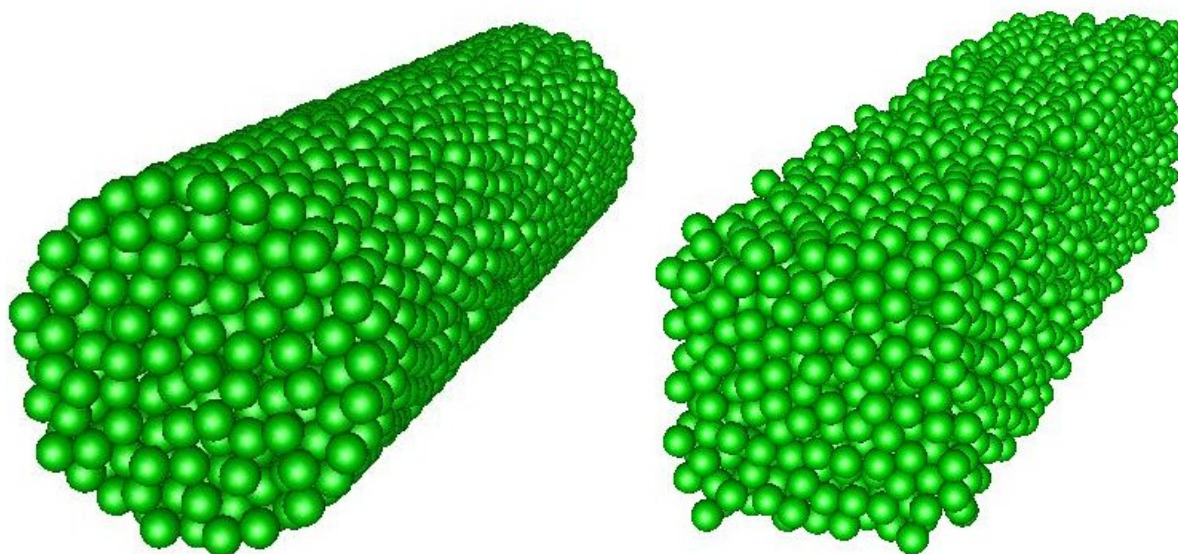


**Figure 4.28.** Random sphere packings generated by the modified Jodrey-Tory algorithm and confined by cylindrical (left) and quadratic (right) containers. Periodic boundary conditions are imposed along the longitudinal direction. The interparticle porosity of both packings is 0.4, the total number of spheres is 3600 (cylindrical packing) and 4500 (quadratic packing).

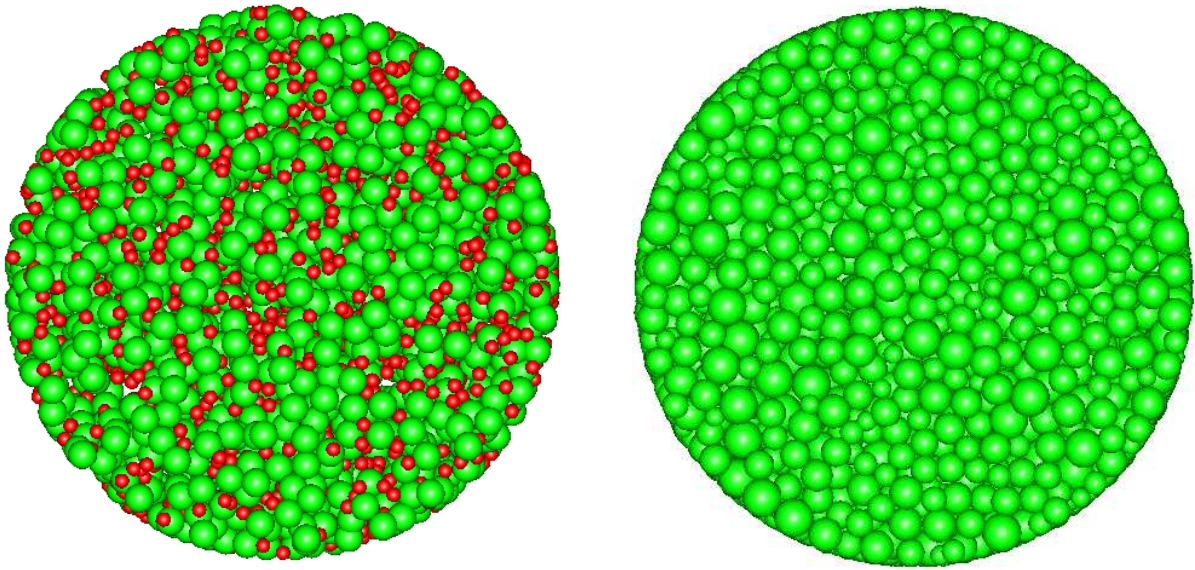


**Figure 4.29.** Top views (from the base plane) of the random cylindrical packings generated by the modified Jodrey-Tory algorithm with the bisized (left) and Gaussian (right) sphere diameter distribution.

#### Quantitative evaluation of random sphere packings

The problem of a quantitative evaluation of random packings originates from, at least, two other problems i) the aimed identity of different packings (e.g., real and computer generated) and ii) establishing of the functional relationship between geometrical properties of the packing and the description of various phenomena taking place within it (e.g., mass and heat transport). The simplest way to characterize quantitatively a packing is to define its porosity or void volume fraction,  $\varepsilon$

$$\varepsilon = 1 - \frac{V_v}{V}, \quad (4.78)$$

where  $V_v$  and  $V$  are the total void volume and total packing volume, respectively. However, with this averaged geometrical characteristic it is frequently not possible to distinguish packings with obviously different properties. For instance, it is well known that fluid flow through a simple cubic (SC) array of spheres with  $\varepsilon_{sc} = 1 - \pi/6 \approx 0.476$  differs substantially from fluid flow through a random packing of spheres with the same porosity. This fact is explained by the presence of through channels in the SC-packing, which reduce the

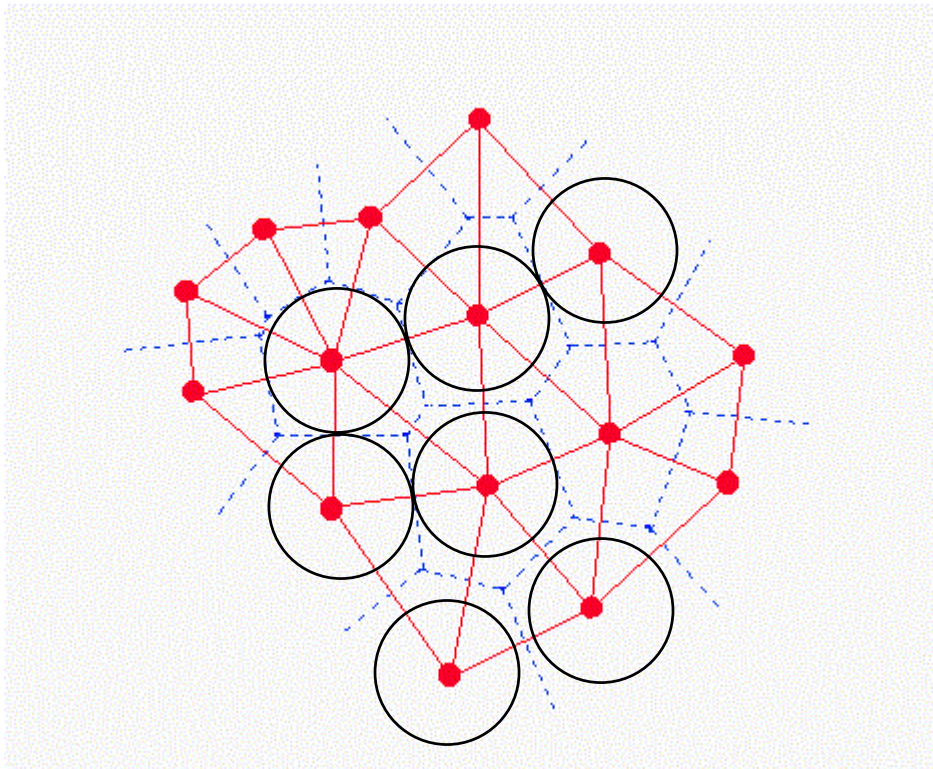


**Figure 4.30.** The Voronoi diagram (blue dashed lines) and Delaunay tessellation (red solid lines) for 2D-dimensional packing of discs.

hydrodynamic resistance along the SC-array primary axes. Hence, a characteristic which evaluates local microstructure of packings should be introduced.

In contrast to packings with crystalline order which can be relatively easy described in terms of group theory, the structure of random packings has to be characterized statistically and its numerical evaluation presents a real challenge because any reasonable compact description of such structures will be necessarily statistical in nature. This detailed statistical information can be written down exactly only for completely random or spatially uncorrelated systems, such as ideal gases. However in actual packings, interactions with other particles and container walls may cause significant deviations from randomness, which ultimately manifest themselves in the form of spatial correlations. Several approaches are commonly applied to analyse quantitatively the microstructure of random media as well as their macroscopic (or averaged) properties. These approaches can be roughly divided into the following three categories:

- Tensorial: fabric and configuration tensors [106-108];
- Topological: Voronoi diagrams and Delaunay tessellations [109-112];
- Probabilistic: correlation (distribution) functions [113,114].

Tensorial methods characterize disorder in packings of particles in terms of the tensors which describe the position of particles with respect to their nearest neighbours. The Delaunay tessellation and the Voronoi diagram are dual structures — each contains the same “information” in some sense, but it is represented in a different form. For a packing of spherical particles, the Voronoi diagram is derived by tracing the mediator plane between two neighbouring spheres (Fig. 4.30). Thus, each particle is contained by a polyhedron. Then, the polyhedrons are classified with respect to different types based on the number and size of their faces. Further statistic analysis of the distribution of the polyhedron types is carried out to derive structural information about the packing. The Delaunay tessellation represents a triangular network which is built up by tracing the centre-to-centre lines between two neighbouring particles. The centres of three neighbouring particles form a triangle. The results of statistic analysis of the distribution of angles and side lengths of the triangles can be used to describe the structure of the random packing. Finally, the pair- and high-order correlation functions related to the probability to find one or more sphere centres in a thin spherical layer can give a complete statistical description of local and long-range correlations. However, none of the abovementioned approaches can be considered as satisfactory concerning the characterization of confined packings. The tensorial formulation of the statistical-geometrical theory requires additional research to transform that theory into a tool, which can be used in analytical calculations, and to establish links between configuration tensors and experimentally measurable characteristics of random packings, such as correlation functions. Voronoi diagrams, Delaunay tessellations and pair-correlation functions are applicable only to infinite packings or those with periodic boundaries. Hence, confined packings are generally excluded as an object of investigations by these approaches. In other words, up to date the theory of a quantification of confined packings is a matter of ongoing investigations. Nevertheless, since a random packing of spherical particles confined by a cylindrical container is widely employed as a model of actual packing structures and has a large industrial relevance, the problem of the numerical characterization of this kind of packings requires a solution, even if this solution is only particularly satisfactory. At present, the most popular (if not only) method to evaluate the randomness or disorder of cylindrical packings of spheres is the analysis of the radial porosity distribution function  $\varepsilon(r)$  that can be defined as

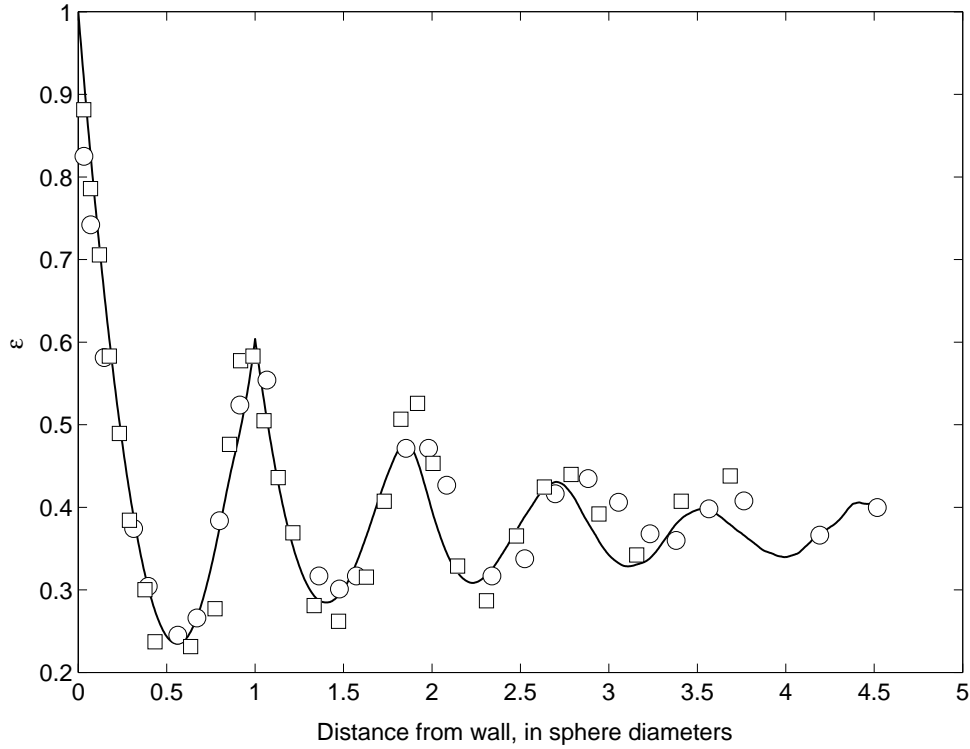


**Figure 4.31.** Radial porosity distribution functions for experimental (symbols:  $\circ$   $d_c/d_p = 14.1$  [165],  $\square$   $d_c/d_p = 9.3$  [166]) and computer generated (solid line  $d_c/d_p = 10.0$ ) cylindrical packings of spheres.

the ratio between the volume occupied by the spheres,  $dV_{\text{sph}}(r)$ , in the thin cylindrical layer of thickness  $dr$  and the volume of this layer at each radial position considered:

$$\varepsilon(r) = 1 - \frac{\int_0^H \int_0^{2\pi} \int_r^{r+dr} dV_{\text{sph}}(r)}{2\pi H r dr},$$

where  $H$  is the height of the evaluated packing. The radial porosity distribution for real packings can be relatively easily obtained by experimental techniques (see Ref. [115] and references therein). It is accepted to assume that two different cylindrical packings of equal mean porosities  $\varepsilon$ , with the same ratio of container diameter to particle diameter  $d_c/d_p$ , and identical radial porosity distribution (RPD)-functions possess identical microstructure, whence, they are invariant and *vice versa*. Naturally, the term “identical” should be interpreted from the statistical point of view.

It is known, that in a random sphere packing formed in a cylindrical container, the layers of spheres nearest to the wall tend to be highly ordered, with most of the spheres touching the wall. The next layer builds up on the surface of the first, in a less ordered



fashion. The successive layers are less and less ordered until a fully randomised arrangement is achieved in regions far enough from the wall, and the term “layer” ceases to be applicable at all. Thus, the RPD-function is an oscillatory function with decreasing oscillations in a bulk region. In Figure 4.31 the experimentally measured RPD functions for packings with different ratios  $d_c/d_p$  [165, 166] (as well as the RPD function of the generated cylindrical packing presented in Fig. 4.28) are shown. Though the validity of the RPD function to reveal small amounts of crystallization in bulk regions of packings is still in doubt, this characteristic is widely practised, in particular, to establish relationships between radial geometrical inhomogeneity of cylindrical packings and nonuniformity of axial flow velocity or hydrodynamic dispersion (e.g., see [116, 117]).

#### *4.4.2. Numerical simulation of liquid hold-up and longitudinal dispersion in biporous media with discrete stagnant zones\**

In this section the results of our study of hydrodynamic dispersion in single-phase incompressible liquid flow through a fixed bed made of spherical, permeable (porous) particles are presented. The observed behaviour was contrasted to the corresponding fluid dynamics in a random packing of impermeable (nonporous) spheres with interparticle void fraction of 0.37. Experimental data were obtained in the laminar flow regime by pulsed field gradient nuclear magnetic resonance and were complemented by numerical simulations employing a hierarchical transport model with a discrete (lattice-Boltzmann) interparticle flow field. Finite-size effects in the simulation associated with the spatial discretization of support particles or dimension and boundaries of the bed were minimized and the simulation results are in reasonable agreement with experiment.

#### Introduction

An understanding of transport phenomena in porous media is important for many technological and environmental processes such as enhanced oil recovery, paper manufacturing, subterranean transport of hazardous wastes, filtration, or fixed-bed operations in catalysis and

---

\* This section is based on the following publications

D. Kandhai, U. Tallarek, D. Hlushkou, A. Hoekstra, P.M.A. Slood and H. Van As. “Numerical simulation and measurement of liquid hold-up in biporous media containing discrete stagnant zones”. *Phil. Trans. R. Soc. Lond. A*, **360**, 521-534 (2002).

D. Kandhai, D. Hlushkou, A. Hoekstra, P.M.A. Slood, H. Van As, and U. Tallarek. “Influence of stagnant zones on transient and asymptotic dispersion in macroscopically homogeneous porous media”. *Phys. Rev. Lett.* **88**, art. no. 234501 (2002).

separation science (e.g., [118-120]). In the past several approaches have been developed to study transport phenomena in porous media and numerical simulations, in particular, were often employed to connect the theoretical analysis with experimental measurements. The extremely complex geometry inherent to porous media, however, has always been one of the major difficulties in these studies. Several simplifications in pore structure or transport mechanisms have been introduced to allow more efficient computer simulations. In the last decade lattice-gas and lattice-Boltzmann simulations (e.g., [34, 121, 122]) have proven to be versatile tools in simulating a wide variety of applications related to transport in porous media. Examples of such applications are diffusion and flow, including multi-component or multi-phase flows in several models of porous media such as spherical bead packings [123], fibrous media [40, 124], and even digitized samples of real porous media [125].

In this section we are interested in the hydrodynamic dispersion in porous media, i.e., transport of tracer particles in a solvent by flow and molecular diffusion within a complex pore network. This problem, also known as pore-scale dispersion, has been the subject of many studies (e.g., [36, 37, 102, 123, 126-135]). In these studies a wide variety of techniques have been applied to probe the motion of tracer particles in a porous medium. Significant progress has been obtained by using theoretical methods, experimental measurements based on Pulsed Field Gradient Nuclear Magnetic Resonance (PFG-NMR) and numerical simulations based on traditional finite-difference schemes and lattice-Boltzmann algorithms in combination with Monte-Carlo methods.

To the best of our knowledge all the numerical modelling efforts conducted so far have focused on porous media composed of *impermeable* spherical beads. Therefore transport is solely restricted to the void space between the bead particles or the so-called interparticle transport. Here we consider porous materials with additional purely diffusive stagnant regions inside the beads, thus allowing for intraparticle mass transport. Our model porous medium is composed of *permeable* spherical beads with rather complex tortuous network. These extra stagnant zones have a substantial influence on dispersion, since fluid molecules entrained in the deep diffusive pools of the particles give rise to a holdup contribution and affect both the timescale of (transient) dispersion and the value of the asymptotic dispersion coefficient [129, 132, 136].

From a computational point of view the main difference between our system and those studied previously is that characteristic time and length scales associated with an exchange of fluid molecules moving in velocity extremes of the flow field may differ by several orders of magnitude. Therefore, a direct numerical simulation that resolves transport processes

including geometrical details of the tortuous pore network inside the permeable beads is not feasible, even with current state-of-the-art high performance computer systems. Instead we followed a hierarchical and semi-empirical modelling approach. The flow field in a computer-generated model of the interparticle pore space was computed by means of a lattice-Boltzmann algorithm. A particle tracking method was then used to record tracer dispersion in the entire interconnected (inter- and intraparticle) pore network. The actual morphology of the intraparticle pore space is lumped into the model by an effective intraparticle diffusion coefficient  $D_{\text{intra}}$ , itself obtained from the PFG-NMR measurements. Mass transfer through the inter/intraparticle interface is accounted for by a stochastic approach.

### Simulation methods

It has already been indicated in the introduction that fluid transport through the packed bed involves a hierarchy of time and length scales. In the measurements, for example, we used spherical, totally porous particles with average diameter of 50  $\mu\text{m}$  packed into a 4.6 mm i.d. ( $d_c$ ) cylindrical column. Pores inside the particles have a mean diameter ( $d_{\text{pore}}$ ) of only 12 nm. The size of interparticle voids is about 25-40% of the particle size [119] and exceeds the intraparticle pore size by a factor of more than  $10^3$ . Mainly due to this variety of spatial and corresponding temporal scales with respect to the flow heterogeneity and mass transfer (see Figure 4.32) we did not attempt a model which simultaneously resolves details at all scales, but exploited a hierarchical approach.

#### *(a) Interparticle transport*

Fluid transport in the voids between bead particles is due to a combination of pressure-driven convection and molecular diffusion. Similar to the detailed work reported by Maier et al. [123] we used a lattice-Boltzmann (LB) algorithm for the computation of the fluid flow field and a particle tracking method to calculate tracer motion in the LB velocities. In LB methods local streaming and collision rules define a mesoscopic world from which the correct hydrodynamic behaviour in certain flow regimes emerges at a macroscopic level [34, 122]. In this paper we used the  $D_3Q_{19}$  lattice BGK model where the collision operator is based on a single-time relaxation to the local equilibrium distribution [53, 122]. To define the displacement probability distributions or averaged propagators  $P_{\text{av}}(\mathbf{R}, \Delta)$  a large number of tracer molecules has been distributed in the computational domain. Since interparticle transport is driven by flow and diffusion the position of each tracer particle during an

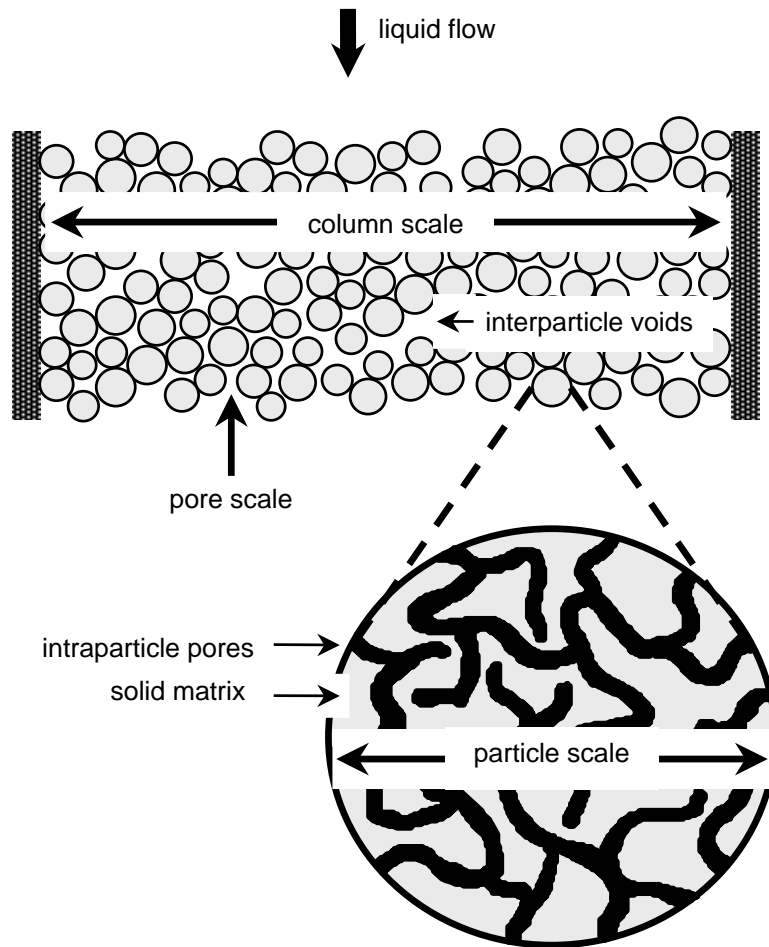


**Figure 4.32.** Illustration of different spatio-temporal scales concerning possible velocity extremes in the mobile phase (and associated mass transfer phenomena based on molecular diffusion or lateral dispersion) in a packed bed.

elementary time step  $\delta_t$  is determined by convective and diffusive contributions and its time evolution can be described by [123]

$$\mathbf{r}(t + \delta_t) = \mathbf{r}(t) + \mathbf{v}(\mathbf{r}(t))\delta_t + \delta\mathbf{r}^D \quad (4.79)$$

where  $\mathbf{v}(\mathbf{r})$  is the local velocity at  $\mathbf{r}$  approximated with the computed flow field by a linear interpolation of velocities at neighbouring lattice nodes.  $\delta\mathbf{r}^D$  is the displacement due to molecular diffusion and can be modelled by a random-walk process

$$\delta\mathbf{r}^D = \xi\sqrt{6D_m\delta_t} \quad (4.80)$$

where  $D_m$  is the free molecular diffusion coefficient ( $D_m = 2.15 \times 10^{-9} \text{ m}^2\text{s}^{-1}$  for water at 25°C) and  $\xi$  is the unit vector with a random orientation in space.  $P_{av}(\mathbf{R}, \Delta)$  is then determined by calculating the number of particles with a net displacement  $\mathbf{R}$  after time  $\Delta$ . The total number of tracer particles is chosen such that statistical fluctuations in  $P_{av}(\mathbf{R}, \Delta)$  are small, and the time step in these simulations is constrained by the maximum net displacement and the lattice spacing [123].

*(b) Intraparticle transport*

Transport inside the bead is purely diffusive because the mean velocity through a network of interconnected pores increases with the square of the pore diameter [118]. Thus, intraparticle pores (assuming that they are well interconnected like interparticle pores in a bed of uniform hard spheres – which is even not guaranteed) restrain fluid motion to a velocity approximately a factor of  $10^6$  less than the interparticle average. Intraparticle diffusion is incorporated in the simulation semi-empirically, i.e., we use  $D_{intra} = 7.3 \times 10^{-6} \text{ cm}^2\text{s}^{-1}$  obtained experimentally for this packing material by PFG-NMR [135]. The motion of tracer particles is modelled by Eq. 4.79, neglecting the convective term.

*(c) Mass transfer between intra- and interparticle pore space*

Close to the particles external surface, in the thin hydrodynamic boundary layer, transport normal to the solid-liquid interface is dominated by diffusion. In the case of porous beads molecules can enter or leave the deep pools of stagnant fluid only through pores that lead from the particles interior to the external surface. Initially, tracer molecules are distributed uniformly in the interconnected pore space. In dealing with the geometrical restrictions for the tracer flux through the spheres external surface we follow a probabilistic approach. Close to this interface fluid transport is diffusive in both the inner ( $D_{intra}$ ) and outer ( $\approx D_m$ ) pore space. Corresponding differences in diffusive displacements within the inter- and intraparticle pore space become apparent in different probabilities for entering or leaving a sphere. By using mass balance arguments the following relation can be derived for the entrance and exit probabilities  $p_{enter}$  and  $p_{exit}$

$$p_{enter} = \frac{D_{intra} n_{intra}}{D_m n_{inter}} p_{exit} = \frac{D_{intra}}{D_m} \frac{N_{intra} \varepsilon_{inter}}{N_{inter} (1 - \varepsilon_{inter})} p_{exit} \quad (4.81)$$

Here  $\varepsilon_{\text{inter}}$  is the porosity of the interparticle pore space and  $N_{\text{inter}}$  and  $N_{\text{intra}}$  are the number of particles in the inter- and intraparticle pore space, respectively.  $n_{\text{intra}} = N_{\text{intra}}/(1 - \varepsilon_{\text{inter}})V$  and  $n_{\text{inter}} = N_{\text{inter}}/\varepsilon_{\text{inter}}V$  are the intraparticle and interparticle tracer concentrations, and  $V$  is the total volume of the porous medium.

In the simulations, we assume the probability for leaving a particle is 1. This choice is optional because the important aspect is the ratio of entrance and exit probabilities.

### Experimental setup and measurements

#### (a) Packed column

A  $4.6 \times 150$  mm poly(arylether-ether-ketone) column was packed and consolidated using the slurry technique (e.g., [137]). We used conventional silica-based particles as packing material. These spherical particles have a relatively narrow and Gaussian size distribution which has been measured on a Coulter LS 130 particle size analyzer (Beckman Coulter, Fullerton, CA). Particles are porous (by 50 %) and intraparticle pores have an average size of  $120 \pm 15$  Å. The mean particle diameter ( $d_p$ ) is  $50.2$  μm, with a standard deviation of  $10.6$  μm. In general, the interparticle porosity  $\varepsilon_{\text{inter}}$  in columns packed by using slurry technology (as in our case) ranges between 0.38-0.4 [138], but can be smaller (about 0.35) when compression techniques like hydraulic axial or radial compression are applied [137, 139]).

#### (b) Displacement probability distributions by PFG-NMR

In an ideal PFG-NMR experiment [140] without spatial localization gradients the complex signal,  $E(\mathbf{q}, \Delta)$ , bears a direct Fourier relation with the Lagrangian averaged propagator,  $P_{\text{av}}(\mathbf{R}, \Delta)$ , of the fluid molecules [141-143]

$$E(\mathbf{q}, \Delta) = \frac{S(\mathbf{q}, \Delta)}{S(0, \Delta)} = \int P_{\text{av}}(\mathbf{R}, \Delta) \exp(i2\pi\mathbf{q} \cdot \mathbf{R}) d\mathbf{R} . \quad (4.82)$$

$P_{\text{av}}(\mathbf{R}, \Delta)$  gives the average probability for any particle to travel a dynamic (net) displacement  $\mathbf{R}$  over time  $\Delta$  in the direction of the pulsed magnetic field gradients of amplitude  $\mathbf{g}$  and duration  $\delta$  [142]. This gradient area defines a wavevector  $\mathbf{q} = (2\pi)^{-1}\gamma\delta\mathbf{g}$  in  $\mathbf{q}$ -space which is space reciprocal to the dynamic displacement  $\mathbf{R}$  [144, 145]. Thus  $P_{\text{av}}(\mathbf{R}, \Delta)$  can be

reconstructed from the PFG-NMR signal by Fourier transformation of  $E(\mathbf{q}, \Delta)$  with respect to  $\mathbf{q}$ . Due to the inherent timescale (including values for  $\Delta$  from a few milliseconds up to a few seconds) it is possible to recover convective and stagnant fluid in  $P_{av}(\mathbf{R}, \Delta)$  and study the associated mass transfer kinetics if, in general,  $\Delta \ll l_{stag}^2/2D_{stag}$  where  $l_{stag}$  is a characteristic dimension of the stagnant zone and  $D_{stag}$  the diffusion coefficient. In this way PFG-NMR has been used to measure the intraparticle effective diffusion coefficient  $D_{intra}$  that we subsequently employ in the simulation to account for the actual morphology of the intraparticle pore space [135, 146]. Experiments were performed with a constant gradient pulse duration ( $\delta = 2.5$  ms), but incremented gradient amplitude using the stimulated echo sequence [147], taking 64  $\mathbf{q}$ -steps in the range of  $\pm \mathbf{q}_{max}$  and 56 phase-alternated signal averages at each value of  $\mathbf{q}$ . Details of the NMR hardware configuration can be found in an earlier publication [146].

## Results and discussion

### *(a) Porous medium*

Prior to a presentation of the actual results concerning the inherent dispersion process we briefly discuss some important aspects of our model porous medium. The packed bed used in the NMR experiments is characterized by a column-to-particle diameter (aspect) ratio,  $\psi_d = d_c/d_p$ , of the order of 100. For the simulations, however, we needed to restrict ourselves to a much smaller system ( $\psi_d = 10$  and a length of  $40 d_p$ ) because of computational limitations. In this respect it is well known that for beds of identical spheres the interstitial porosity ( $\epsilon_{inter}$ ) starts with a maximum value of unity at the column wall and displays damped oscillations with a period close to  $d_p$  over a distance of up to  $5 d_p$  into the bulk until the void fraction reaches values which are typical for random packings ( $\epsilon_{inter} = 0.38-0.40$ ) [117, 148]. It is caused by a decrease of packing order as the distance from the wall increases.

The consequences of this geometrical wall effect for macroscopic flow heterogeneity on a column-scale (see Figure 4.32), axial dispersion, and particle-to-fluid heat and mass transfer are particularly severe at aspect ratios below 15 where the critical “wall annulus” occupies a substantial fraction of the beds cross-section [149-152]. For systems with a larger  $\psi_d$ , however, these effects become smaller and it was found that, e.g., the dispersion in beds of spheres is then independent of  $\psi_d$  [126]. To represent closer the column cross-sectional average of fluid transport in the PFG-NMR measurements ( $\psi_d \approx 100$ ) we considered periodic packings in the simulations ( $\psi_d = 10$ ).

There exists a number of algorithms which may be used to generate a random packing of spheres even though the expression of actual randomness in such a system still poses challenges [154]. In particular, Monte-Carlo schemes [153] and drop-and-roll methods [102, 155] have been used. To obtain an adequate representation of our porous medium a random packing of identical hard spheres has been simulated using the Jodrey-Tory algorithm [104]. This method was chosen because of its efficiency and the dense bed that we actually required ( $\epsilon_{\text{inter}} = 0.37$ ). Since we have reproduced this algorithm with only slight differences we will not discuss it. One of the most widely known tools for investigating “randomness” of a bed structure is an analysis of the pair-correlation function  $g(\mathbf{r})$ .  $g(\mathbf{r})d_p^3\mathbf{r}$  is proportional to the probability of finding a sphere with its center in a volume  $d_p^3\mathbf{r}$  at distance  $\mathbf{r}$  from a given point. It is normalized to unity when  $\mathbf{r}$  goes to infinity. We checked whether  $g(\mathbf{r})$  of the bed exhibits features well known for random structures [156]. In particular, a double-peak characteristic for close packing appears in the range 1.7-2.0, and oscillations decay to unity at larger  $\mathbf{r}$  (Fig. 4.33).

(b) Finite-size effects

LB methods have proven to be versatile tools in the simulation of fluid flow through

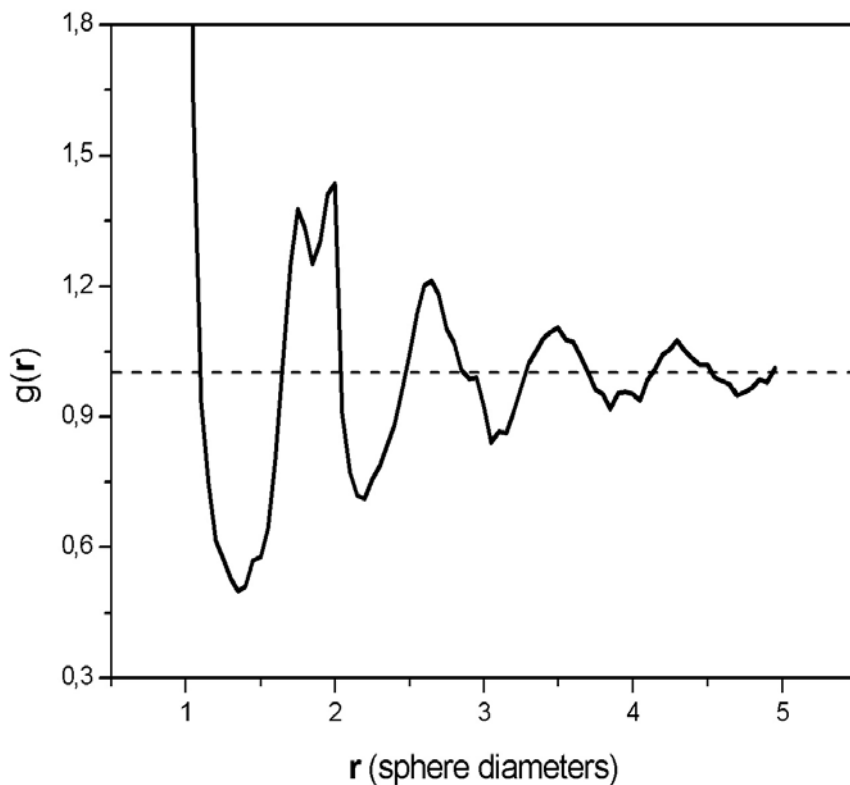


**Figure 4.33.** Pair-correlation function for a sphere packing of dimension  $10D \times 10D \times 10D$ .



porous media [34, 40, 124], mainly due to their flexibility in dealing with arbitrary and complex geometries. Further, the inherent spatial and temporal locality of the simulation algorithm makes it ideal for parallel processing, facilitating large-scale simulations [157]. Commonly, the no-slip condition at the solid-liquid interface is implemented by a simple bounce-back formalism. However, it has been pointed out that problems related to this bounce-back boundary condition may lead to a significant error in the flow field (e.g., [63]). In practice, a sufficiently large computational grid is often required to reduce these effects. To gain more insight into this artifact we performed preliminary simulations for flow in a periodic box of dimension  $10D \times 10D \times 10D$  (with  $D$  equal to the diameter of the beads in lattice units) and  $\varepsilon_{\text{inter}} = 0.37$ . The BGK relaxation parameter is unity and viscous flow is driven by a constant body force. From the flow field we computed the hydraulic permeability,  $K$ , using sphere diameters of 10, 15, 20, 25 and 30 lattice points.  $K$  is often used to characterize flow through porous media and expresses the flow resistance by the solid phase [118]. Figure 4.34a shows computed values of dimensionless permeability  $k = 4K/d_p^2$  for a different sphere discretization. It is obvious that as the resolution is increased  $k$  approaches a constant value and the difference between results obtained with a diameter of 20 lattice points is less than 11% compared to 25 lattice points. A further increase does not significantly improve the results.

Besides numerical errors associated with the boundary conditions, recorrelation effects due to the periodic boundaries may also influence dispersion. These effects were studied in detail by Maier et al. [123] and can be analysed to some extent via the velocity autocorrelation function (VACF) for a simulation box and Peclet number while changing dimensions. The VACF measures the decay of the velocity autocovariance from its initial value. The longitudinal velocity autocovariance  $C_L(t)$  is defined as

$$C_L(t) = \sum_{i=1}^N (v_i(t) - v_{\text{av}})(v_i(0) - v_{\text{av}}), \quad (4.83)$$

with  $v_i(t)$ , the velocity of tracer particle  $i$  at time  $t$ ,  $v_{\text{av}}$  is the mean velocity of tracers and the VACF is given by  $C_L(t)/C_L(0)$ . Figure 4.34b compares the behaviour of systems with dimension  $10D \times 10D \times 10D$  and  $40D \times 10D \times 10D$ . It is clear that stronger recorrelation

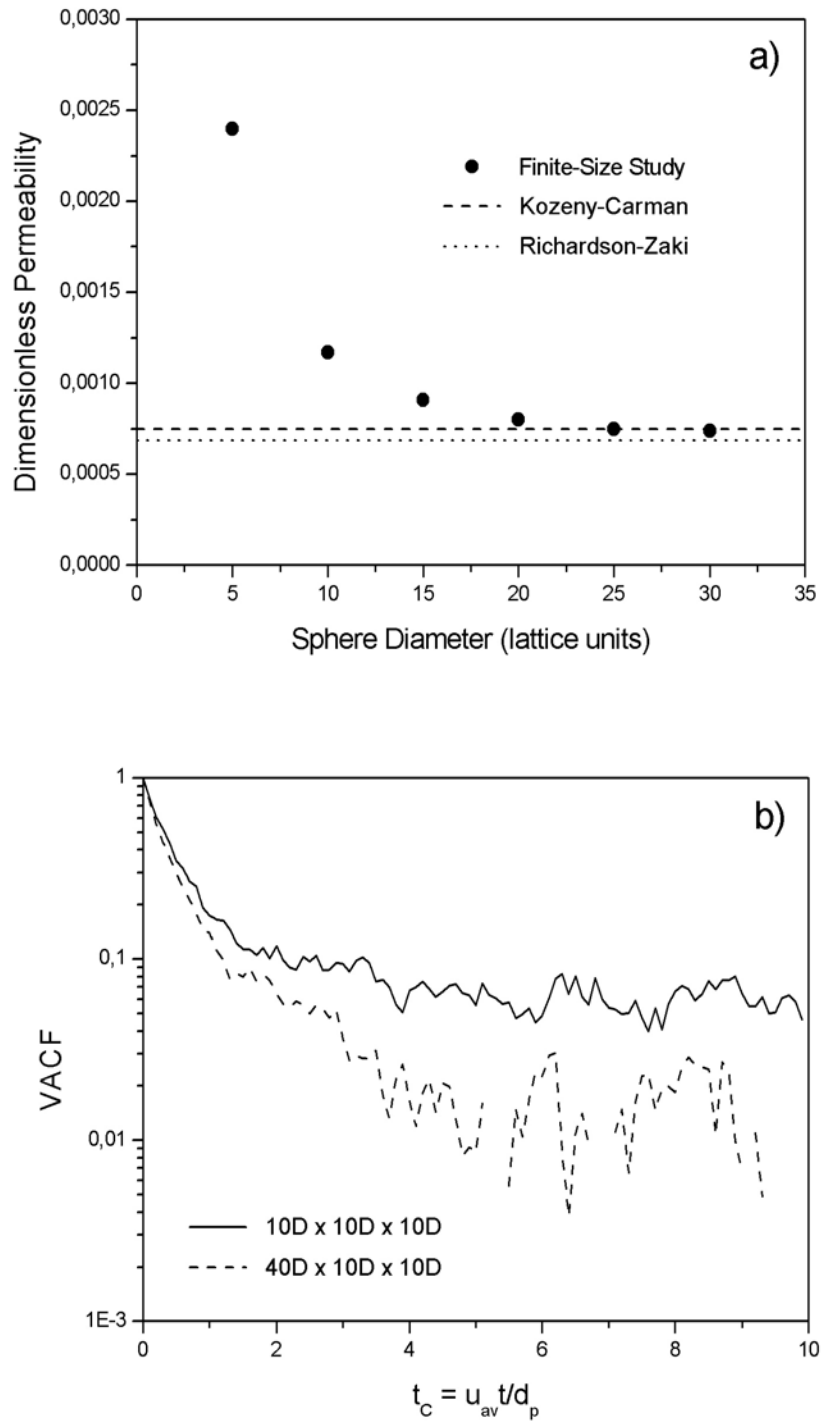


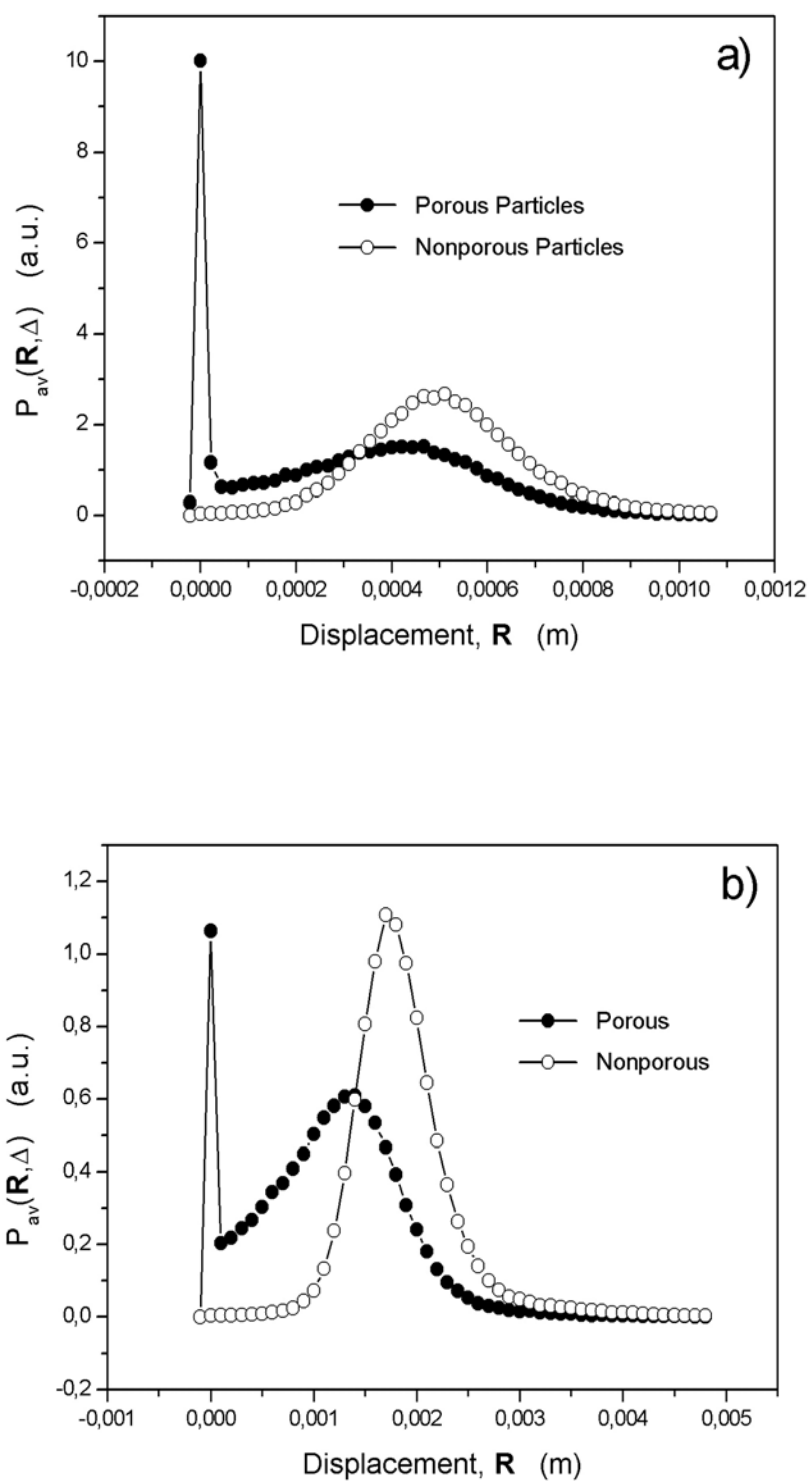
**Figure 4.34.** Finite-size effects. a) Dimensionless bed permeability ( $k = 4K/d_p^2$ ) vs. the spatial discretization of a particle. b) Velocity autocorrelation function  $C_L(t)/C_L(0)$  (cf. Eq. 4.83) vs. the dimensionless convective time in random sphere packings of different length,  $\epsilon_{inter} = 0.37$ .

effects are present in the smaller system. They tend to slow down the decay of the VACF, thereby increasing the longitudinal dispersion coefficient by an artificial contribution [123]. Based on these observations we used the system with  $40D \times 10D \times 10D$ ,  $D = 20$  lattice points and, thus, a grid size of  $800 \times 200 \times 200$  in our final simulations.

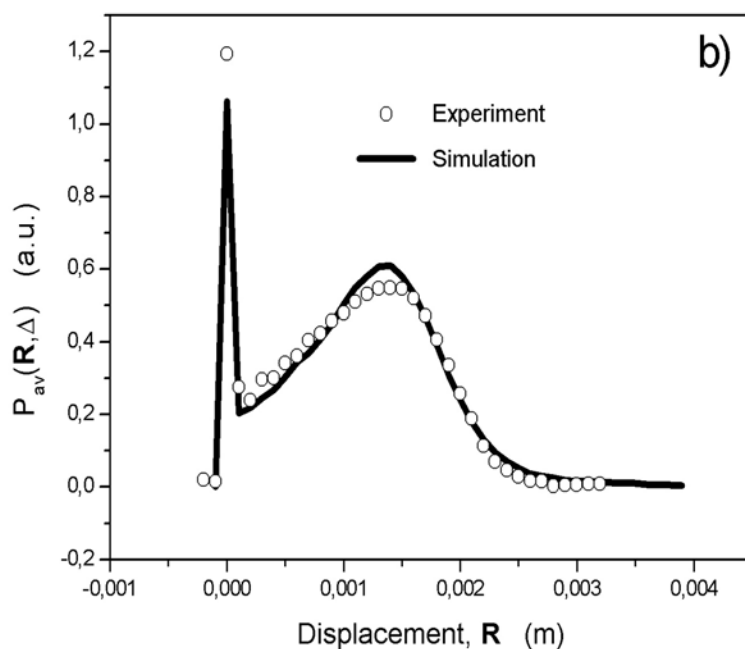
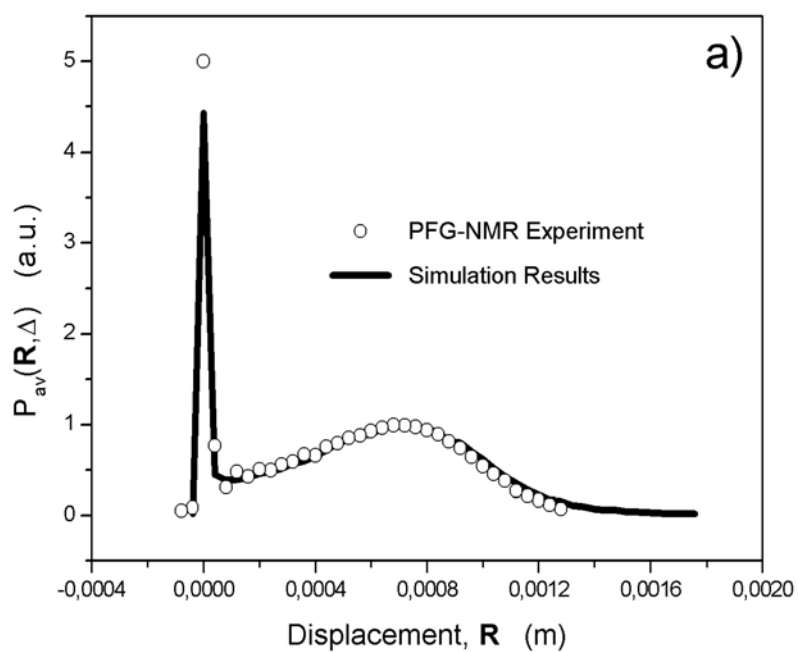
(c) *Propagator distributions*

Figure 4.35 begins with a comparison of simulated propagator distributions for the random packings of nonporous (impermeable) and porous (permeable) uniform spheres. The characteristic differences in propagator position and shape for the otherwise identical sphere packings originate in the existence of a pronounced intraparticle stagnant zone in the case of porous particles. The volumetric flow rate ( $Q$ ) is the same in both cases, but it results in different averaged linear velocities through the bed ( $v_{av} = Q/\varepsilon_T A$  with  $A$ , the columns free cross-sectional area) according to the total porosity  $\varepsilon_T$  of the respective pore space:  $\varepsilon_T = \varepsilon_{inter} = 0.37$  for nonporous spheres and  $\varepsilon_T = \varepsilon_{inter} + (1 - \varepsilon_{inter})\varepsilon_{intra} = 0.68$  for porous spheres ( $\varepsilon_{intra} = 0.5 V_{sph}$ ). Consequently, at observation times  $\Delta < d_p^2/8D_{intra}$  we observe a stagnant, i.e., diffusion-limited fluid fraction in  $P_{av}(\mathbf{R},\Delta)$  very close to zero net displacement (Fig. 4.35).

It contains molecules that have remained only inside the particles over time  $\Delta$  (diffusive ensemble) while those molecules leaving or entering the sphere gain a net displacement due to interparticle flow. By contrast,  $P_{av}(\mathbf{R},\Delta)$  for the random packing of nonporous spheres does not reveal any diffusion-limited fluid, i.e., molecules which temporarily experience the no-slip condition at the solid-liquid interface exchange rapidly with downstream velocities in the interparticle channels of only a few micrometers in dimension. Thus, boundary layer mass transfer is already in a steady-state (achieved by diffusion normal to the interface) at the shortest observation time realized in our study ( $\Delta = 15$  ms). Intraparticle motion of tracer molecules is computed via Eqs. 4.79 and 4.80 with zero velocity field and by using the experimental  $D_{intra} = 7.3 \times 10^{-6} \text{ cm}^2\text{s}^{-1}$  for water inside these particles [135] instead of  $D_m$  to represent tortuosity-limited effective diffusion. When comparing simulated bimodal propagator distributions obtained for porous particles with the results of our PFG-NMR measurements we observe a reasonable agreement regarding the reproduction and scaling with time of interparticle convective-diffusive and intraparticle stagnant fluid (cf. Fig. 4.36).



**Figure 4.35.** Simulated displacement probability distributions for pressure-driven flow of water through a random packing of spheres. The system size is  $40D \times 10D \times 10D$  with  $D = 20$  lattice points. a)  $\Delta = 25$  ms, b)  $\Delta = 90$  ms.



**Figure 4.36.** Comparison of the simulated and measured displacement probability distributions for liquid flow through a bed of porous particles ( $d_p = 50 \mu\text{m}$ ,  $\varepsilon_T = 0.68$ ).  $Pe = u_{av}d_p/D_m = 274$ ,  $Re = v_{av}d_p/\nu = 0.66$ , kinematic viscosity:  $\nu = 8.9 \times 10^{-3} \text{ cm}^2\text{s}^{-1}$  at  $25^\circ\text{C}$ . a)  $\Delta = 45 \text{ ms}$ , b)  $\Delta = 90 \text{ ms}$ .

*(d) Transient and asymptotic longitudinal dispersion*

Natural and industrial materials such as soil, rock, filter cakes, or catalyst pellets often contain low-permeability zones with respect to hydraulic flow of liquid through the medium or even stagnant regions which then remain purely diffusive. The relevance of stagnant zones stems from their influence on dispersion: Fluid molecules entrained in the deep diffusive pools cause a substantial holdup contribution and thereby affect the time scale of transient dispersion, as well as the value of the asymptotic dispersion coefficient (if the asymptotic long-time limit can be reached at all) [129, 132, 136]. Consequently, the associated kinetics of mass transfer between fluid percolating through the medium and stagnant fluid becomes rate limiting in a number of dynamic processes, including the separation and reaction efficiency of chromatographic columns and reactors.

In this respect, transport phenomena observed in model systems such as random packings of spheres may help to characterize materials with a higher disorder [120]. Compared to nonporous (impermeable) spheres a fixed bed of porous (permeable) particles contains an additional contribution to the dispersion which arises from liquid holdup (diffusion-limited mass transfer) in the particles. Both our PFG-NMR measurements and numerical simulations characterizing diffusion and convection on a timescale short enough to capture the disequilibrium of intraparticle fluid transport indicate in an encouraging agreement that liquid holdup strongly affects longitudinal dispersion. Thus, the hierarchical simulation approach presented and validated above in our work enables us to study in more detail the associated (diffusion-limited) mass transfer kinetics and influence of stagnant zones on both transient and asymptotic longitudinal and transverse dispersion. This, in turn, will allow us to discriminate directly between dispersion mechanisms that originate in flowing and stagnant regions of the medium and helps to determine whether an inequality of the macroscopic flow pattern or mobile phase stagnation contributes most persistently to transient dispersion at a given Peclet and Reynolds number.

Despite numerous theoretical, experimental, and numerical studies (e.g., [102, 118, 120, 123, 128, 133]), the transient and asymptotic behavior of dispersion in porous media is not completely understood [131]. In particular, the influence of stagnant zones with respect to the actual mesoscopic and macroscopic flow field heterogeneity of the medium has found little attention in theory and experiment, and furthermore, the additional length and time scale associated with transport in stagnant regions complicates numerical simulations. Therefore it leaves the controversy about the dominating contribution to dispersion and the origin of long-time tails in residence-time distributions unresolved [120, 132], let alone the question whether

hydrodynamic dispersion coefficients exist at all [131]. Below, we are able to resolve this issue experimentally and numerically for a macroscopically homogeneous medium by considering transient and asymptotic dispersion in a random packing of porous spheres, i.e., in a medium with bimodal porosity and associated length scales that differ by orders of magnitude. The results are contrasted to the behavior observed in packed beds of nonporous spheres.

In the experiments we used pulsed field gradient nuclear magnetic resonance (PFG-NMR) [143] to measure over discrete temporal and spatial domains longitudinal nuclear spin (hence, molecular) displacement probability distributions of the fluid molecules in single-phase incompressible flow through beds of porous particles with average diameter ( $d_p$ ) of 50 and 34  $\mu\text{m}$  and average pore size ( $d_{\text{pore}}$ ) of 12 nm packed into a 4.6 mm internal diameter ( $d_c$ ) cylindrical column. The abovementioned hierarchical approach was used for the numerical simulations: A lattice-Boltzmann algorithm was implemented for computing the flow field in the interparticle pore space, and a particle tracking method was then used to record tracer dispersion in the total interconnected pore network (between and inside particles).

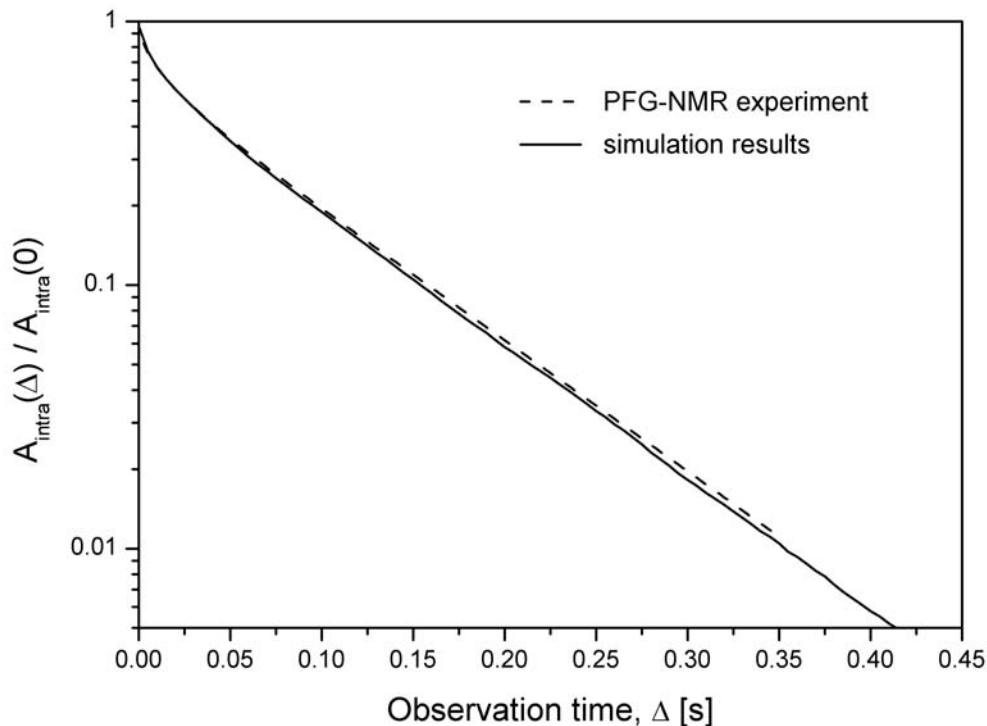


**Figure 4.37.** Intraparticle stagnant mobile phase mass transfer kinetics ( $d_p = 50 \mu\text{m}$ ,  $Pe = 274$ ).

By recording the amount of stagnant fluid molecules at the increasing observation time  $\Delta$  that remain unexchanged with the interparticle velocities,  $A_{\text{intra}}(\Delta)$ , we can monitor a (fictitious) emptying of the spherical particles characterized by the classical mass transfer rate constant  $B_{\text{intra}} = 4\pi^2 D_{\text{intra}} / d_p^2$  [135]

$$\frac{A_{\text{intra}}(\Delta)}{A_{\text{intra}}(0)} = \frac{6}{\pi^2} \sum_{n=1}^{\text{inf}} \frac{1}{n^2} \exp(-n^2 B_{\text{intra}} \Delta) \quad (4.84)$$

Figure 4.37 demonstrates that the experimental and simulated intraparticle mass transfer kinetics match satisfactory (within 3%) using  $D_{\text{intra}} = 7.3 \times 10^{-6} \text{ cm}^2 \text{ s}^{-1}$  and  $d_p = 5.0 \times 10^{-5} \text{ m}$  in both cases. As mentioned, this value for  $D_{\text{intra}}$  is obtained from the experimental data ( $B_{\text{intra}} = 11.52 \text{ s}^{-1}$ ) [135] and is then used in the simulations to reconstruct diffusion-limited mass transfer. The results in Fig. 4.37 demonstrate that the semiempirical simulation procedure followed in this section works well, as does Eq. 4.84 in describing both data sets.

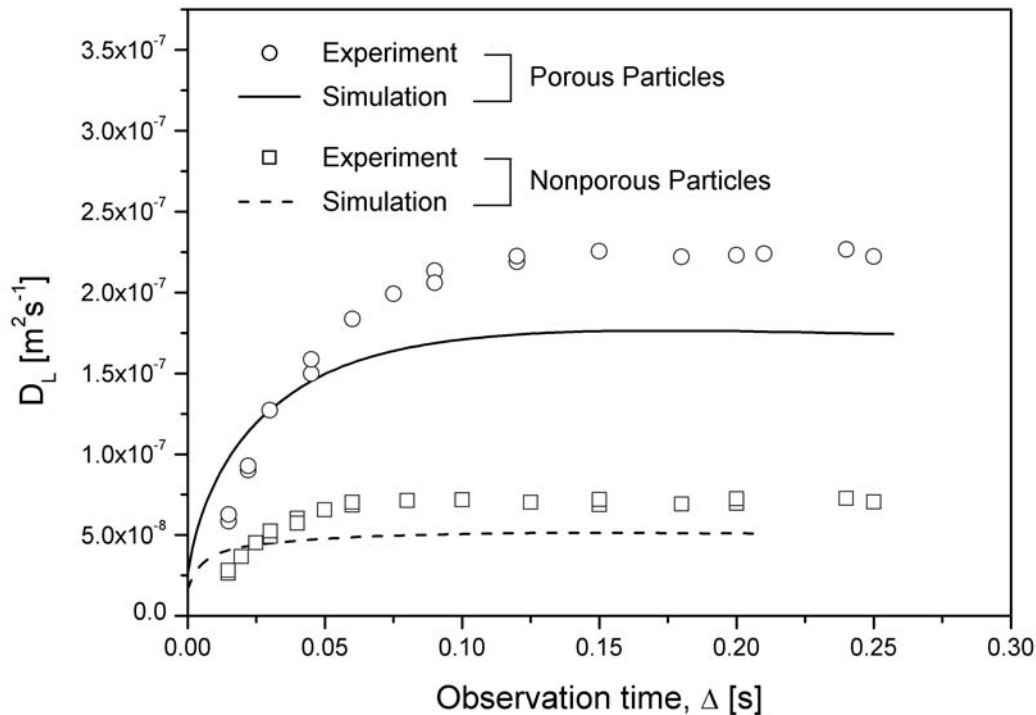


**Figure 4.38.** Time-dependent longitudinal dispersion for flow through random packings of porous and nonporous spheres. In both cases  $d_p = 34 \mu\text{m}$ ,  $\varepsilon_{\text{inter}} = 0.37$ ,  $Pe = 54$  and  $Re = 0.13$ .



Thus, mass transfer in these spatially discrete stagnant zones (uniform spheres) has been adequately accounted for and allows us to focus now on its influence on longitudinal dispersion which we analyze by [133]

$$D_L(t) = \int_0^t C_L(t') dt', \quad (4.85)$$

where  $C_L$  is defined by Eq. 4.83. Figure 4.38 compares transient behavior at constant  $Pe$  ( $d_p = 50 \mu\text{m}$ ,  $d_c = 4.6 \text{ mm}$ ). In both experiment and simulation  $D_L(t)$  for the nonporous particles reaches its asymptotic value ( $D_L^*$ ) in a much shorter time (after approximately 50 ms) than with the porous particles (ca. 160 ms). While we observe a good agreement between simulation and experiment concerning this time scale,  $D_L^*$  itself is underestimated by the simulation in either case (by up to 25%). This effect seems to be systematic as it appears for packings of porous and non-porous particles and is probably caused by inaccuracies in the LB

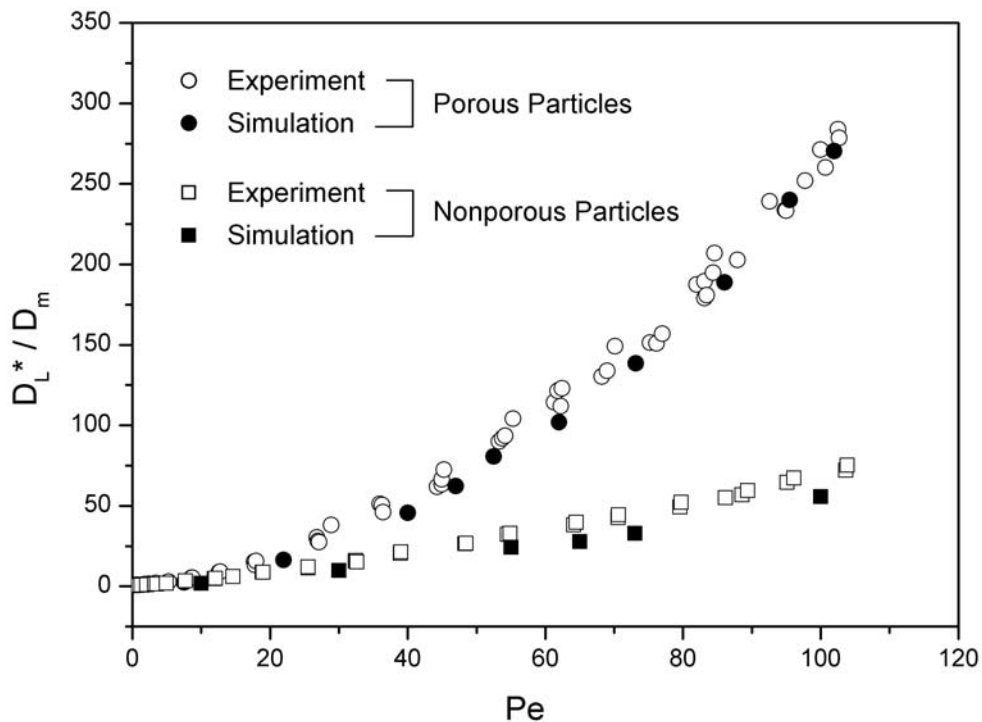


**Figure 4.39.** Dependence of asymptotic longitudinal dispersion on Peclet number in fixed beds of porous and nonporous particles ( $d_p = 34 \text{ mm}$ ,  $d_c = 4.6 \text{ mm}$ ). Liquid phase: water. The experimental data in Figs. 4.38 and 4.39 were obtained with an accuracy of better than 5%.

flow field (notice that the relative error in the hydraulic permeability, a measure of the flow resistance by the solid phase, is around 11%). Other possible explanations are related to the influence of the column wall confining the sphere packing [44], bead particles not being perfectly monodisperse (as evident from Fig. 2, cf. [135]), and the fact that the nonporous particles actually have small (micro)pores at the surface which contribute to a finite but small particle holdup. With the independently measured  $D_{\text{intra}}$  and known  $d_p$ , intraparticle diffusion can be identified as the most persistent contribution to transient dispersion in the random packing of porous spheres, i.e., the holdup dispersion mechanism reaches its long-time behavior after  $t_h = d_p^2 / 8D_{\text{intra}}$  [135]. For nonporous particles, on the other hand, we find a qualitative agreement between the corresponding time scale (about 50 ms, Fig. 4.38) and characteristic time for boundary-layer dispersion ( $t_b = 40$  ms) based on the nonlocal dispersion theory of Koch and Brady [129]. This transient behavior may be also due to mechanical dispersion [34, 123]. Further work is needed to resolve these contributions in macroscopically homogeneous beds of nonporous particles.

Figure 4.39 compares the velocity dependence of asymptotic dispersion coefficients for random packings of porous and nonporous spheres in the range  $0.1 < Pe < 100$ . When analyzing the dependence of  $D_L^*$  on  $Pe$  we have to account for longitudinal diffusion, mechanical dispersion ( $\Theta_m$ ), the boundary layer mass transfer ( $\Theta_b$ ) and, of course, the intraparticle holdup ( $\Theta_h$ ) [120, 128]

$$\frac{D_L^*}{D_m} = \Upsilon + \Theta_m Pe + \Theta_b Pe \ln(Pe) + \Theta_h Pe^2. \quad (4.86)$$

For  $Pe \rightarrow 0$   $D_L^*/D_m$  approaches the packed beds tortuosity factor  $\Upsilon$  which represents the long-time diffusion coefficient in the interconnected pore space. This value has been measured independently by PFG-NMR (without flow) and is subsequently used in the analysis. We then fitted the experimental data,  $D_L$  vs  $Pe$  (Fig. 4.39), to Eq. 4.86 and the values of the parameters ( $\Upsilon$ ,  $\Theta_m$ ,  $\Theta_b$ ,  $\Theta_h$ ) thus obtained are  $(0.51, 0.153 \pm 9 \times 10^{-3}, 0.080 \pm 5 \times 10^{-3}, 1.65 \times 10^{-3} \pm 2 \times 10^{-4})$  and  $(0.74, 0.144 \pm 0.016, 0.101 \pm 0.011, 0.020 \pm 6 \times 10^{-4})$  for the packings of nonporous and porous spheres, respectively. The most striking feature of this analysis is the substantial difference in  $\Theta_h$  characterizing holdup dispersion by more than one decade. Further, mechanical dispersion is very similar in both columns which were packed and consolidated by the same procedure. Values for  $\Theta_m$  (0.153 and 0.144) are actually of the same order as  $\Theta_m = 0.25$  reported by Maier et al. [123] for their simulation of dispersion in random

packings of nonporous spheres, in the range  $1 < Pe < 5000$  and with  $\varepsilon_{\text{inter}} = 0.44$ . As has already been pointed out by these authors, values for  $\Theta_b$  found in our work (0.08 and 0.101), together with their own value (0.03) suggest that boundary layer dispersion is much lower than predicted by the theory of Koch and Brady [128]. A possible explanation for this discrepancy may be found in the significantly different porosities considered in that theory, on one hand, and the simulations and experiment on the other. Even the relatively small difference in particle volume fractions of the systems used by Maier et al. [123] ( $\varepsilon_{\text{inter}} = 0.44$ ) and in this work ( $\varepsilon_{\text{inter}} = 0.37$ ) may contribute significantly to the observed differences in  $\Theta_m$  and  $\Theta_b$ .

To conclude, the present work combines experimental and numerical elements to differentiate between dispersion mechanisms that originate in stagnant and flowing regions of a macroscopically homogeneous porous medium. The numerical simulations employ a semiempirical hierarchical model with a single free parameter to cope with the large variety of temporal and spatial scales. The results are in good agreement with our experimental data and clearly demonstrate the dominating contribution of liquid holdup to transient (Fig. 4.38) and asymptotic (Fig. 4.39) longitudinal dispersion in a random packing of porous spheres with column-to-particle diameter ratio above 100. Persistent effects due to flow field nonuniformities were not identified which suggests that characteristic times for mechanical dispersion are short compared to the diffusive time of this nonmechanical contribution. These findings also suggest that holdup dispersion in porous media may be more important than assumed in many cases [120, 131, 132]. One of the remaining challenges is to characterize the relative importance of mechanical and nonmechanical dispersion mechanisms when the heterogeneity length scale is increased, e.g., in a confined random sphere packing with smaller column-to-particle diameter ratio. Then, the macroscopic flow profile may start to dominate dispersion and prevent an observation of Gaussian residence-time distributions [44].

#### *4.4.3. Numerical simulation of electroosmotic flow in porous media*

##### *Theoretical approaches*

Capillary electrochromatography (CEC) is a high-performance liquid chromatographic (HPLC) separation technique that employs packed capillary columns and an applied electric field to drive the mobile phase by electroosmotic flow. The use of high electric fields instead of the high column inlet pressure utilized traditionally in HPLC allows to realize capillary columns packed with very small particles and flow rates that would require a prohibitively high pressure drop in HPLC. In order to exploit this advantage of CEC, control and

optimisation of electrochromatographic conditions are of great importance. As it has been mentioned above, even an incomplete theoretical description of the EOF and the accompanying mass transport requires the solution for the coupled Navier-Stokes, Nernst-Planck, and Poisson equations, a daunting task for porous media with their tangled pore networks. Therefore, in the majority of cases the original problem of the EOF through porous media is replaced by a simplified one, where the fluid flow is assumed to be generated by the network compounded of “primary pores”, i.e., microchannels with a geometry that allows to get an analytical solution for the EOF through the pore space. As such a “primary pore” a flat solid-liquid interface or tubular channel is most frequently employed (see, e.g. [158-160], although other geometries were also investigated [161].

Let us consider a random-close packing of spherical-shaped, solid and dielectric (i.e., impermeable and nonconducting) particles with a uniform distribution of the  $\zeta$ -potential at their external surface and an EDL thickness  $\lambda_D$  much smaller than the particle diameter  $d_p$ . In this thin EDL limit ( $d_p/\lambda_D \gg 1$ ) the average EOF velocity through a column of volume  $V$  is obtained by integration over the interparticle bed volume  $V_v$  [162]

$$\langle \mathbf{v}_{eo} \rangle = \frac{1}{V} \int_{V_v} \mathbf{v}_{eo} dV = -\frac{\varepsilon_0 \varepsilon_r \zeta}{\eta V} \int_{V_v} \mathbf{E}_{ext} dV, \quad (4.87)$$

where  $\mathbf{v}_{eo}$  is the local slip velocity along the particles surface just outside the thin EDL which results from the lines of force (in the EDL) due to interaction of the electrical field of local strength  $\mathbf{E}_{ext} = -\nabla\Phi$  with a locally charged fluid and defined by the Helmholtz-Smoluchowski equation (Eq. 4.36). Because the incompressible flows of electricity and fluid are parallel and proportional to each other at the solid-liquid interface, Eq. 4.87 is supposed to hold also throughout the whole liquid phase [163]. For the macroscopic electrical current density we have

$$\langle \mathbf{i}_{el} \rangle = \sigma^* \langle \mathbf{E}_{ext} \rangle = \frac{\sigma^\infty}{V} \int_{V_v} \mathbf{E}_{ext} dV = \frac{\sigma^\infty}{V_c} \int_{V_v} \frac{\mathbf{i}_{el}}{\sigma^\infty} dV, \quad (4.88)$$

where  $\sigma^\infty$  is the conductivity of the equilibrium electrolyte beyond the EDL and  $\sigma^*$  stands for the conductivity of the packed column. By combining Eqs. 4.87 and 4.88 we obtain

$$\langle \mathbf{v}_{eo} \rangle = -\frac{\varepsilon_0 \varepsilon_r \zeta \langle \mathbf{i}_{el} \rangle}{\eta \sigma^\infty} = -\frac{\varepsilon_0 \varepsilon_r \zeta \langle \mathbf{E}_{ext} \rangle}{\eta} \left( \frac{\sigma^*}{\sigma^\infty} \right). \quad (4.89)$$

Thus, the EOF velocity averaged over the column cross-section can be expressed by means of the conductivity ratio  $\sigma^*/\sigma^\infty$  which becomes accessible experimentally via conductivities of a packed column and an identical, but open tube saturated with the same electrolyte solution. The above model (Overbeek's model) is valid for beds of nonporous (and porous) particles with arbitrary shape and size distribution.

Though the aforementioned approach is valid for beds of nonporous (and porous) particles with arbitrary shape and size distribution, may involve a pore diameter distribution and provides a sufficiently accurate approximation for the averaged velocity of the EOF, it does not provide any information on velocity profiles or velocity distributions which is of the utmost importance for an evaluation of hydrodynamic dispersion in porous media.

### Numerical approaches

As it was mentioned above, the analytical resolution for the electroosmotic flow and associated transport phenomena in porous media, in particular concerning packed chromatographic columns, is impossible, except for a simplified formulation of this problem under an extensive set of assumptions. Therefore, up to date the numerical solution or numerical simulation of electroosmotic flow in porous media is frequently the only way to obtain detailed *a priori* information on relevant phenomena. However, numerical simulations of the EOF and associated transport phenomena in actual porous structures are often very extensive concerning computational time. This fact is mainly caused by the difference in the length scales based on the EDL thickness and characteristic length of actual porous media. For an illustration, consider a typical chromatographic column of 150  $\mu\text{m}$  i.d. filled with a 1 mM aqueous electrolyte solution. The corresponding EDL thickness  $\lambda_D$  is approximately 10 nm which provides an aspect ratio  $d_c/\lambda_D \approx 15000$ . Then, the use of a uniform computational grid based on the lattice space  $\Delta x = \lambda_D$  (which cannot generally guarantee high numerical accuracy) requires a numerical treatment of about  $2 \times 10^8$  grid points only for two transversal dimensions (relative to the mean EOF direction). Since frequently the asymptotic behaviour of the dispersion is of interest, the longitudinal dimension of the simulated domain will be determined by the mean displacement due to the EOF,  $\Delta l = \langle \mathbf{v}_{eo} \rangle \Delta t$  during time  $\Delta t$  which corresponds to a mean diffusion displacement across the whole column,  $\Delta l_{diff} =$

$\sqrt{2D_m\Delta t}$ , where  $D_m$  is the diffusion coefficient. Assuming  $D_m = 2.25 \times 10^{-9} \text{ m}^2/\text{s}$ ,  $\langle v_{eo} \rangle = 0.2 \text{ mm/s}$  and  $\Delta l_{\text{diff}} = 150 \text{ }\mu\text{m}$ , the simple calculation results in  $\Delta l = 1.0 \text{ mm}$  or (in terms of the computational grid)  $10^6$  points. It is obvious, that a numerical solution of the problem with a computational grid consisting of  $10^{14}$  points is unrealistic even for high-performance computers. The use of nonuniform computational grids with finer resolution in the EDL, where large gradients in physical quantities exist, and coarser resolution in bulk fluid regions, where those quantities vary much more slowly, can reduce the total computational expenses. However, the efficiency of this approach distinctly decreases for porous media with ramified morphology and relatively large surface-to-volume ratio. Therefore, modern numerical simulations of the EOF through porous media are still confronted with the following dilemma: whether to restrict the simulated domain, but obtain a more detailed and accurate solution; or to sacrifice accuracy, but resolve the problem at both bigger spatial and temporal domains. The former approach is usually applied to steady-state simulations, while the latter is more applicable to simulation of the transient behaviour in evolving systems.

One of the ways to reduce the total computational expenses is to eliminate from the simulation the length scale associated with the EDL thickness. This can be carried out by dividing the flow field into two regions, the “inner” region comprising flow within the EDL adjacent to the solid-liquid interface and the “outer” region beyond the EDL [20]. It can be shown by an order of magnitude analysis [20, 85] that under the assumptions of a thin double layer and uniform  $\zeta$ -potential, the EOF in arbitrary shaped microchannels can be presented by the flow in an “outer” region and by the slip boundary conditions at the shear plane expressed by the “local” Helmholtz-Smoluchowski equation (Eq. 4.36). This approach assumes the “inner” region be locally flat, with the dominating viscous drag force and electrostatic body force associated with electrical charges at the solid surface. In the same time, the “outer” region is characterized by a domination of inertial and pressure forces. This allows to decouple completely the electrostatic and hydrodynamic problems for the “outer” region, except for the slip velocity at the shear plane. It is obvious, that the accuracy of the above approach is determined by the validity of the flow division into two regions and depends on the aspect ratios between different length scales. It can be shown that in the two-dimensional channel with hydraulic diameter  $d$  the following approximate conditions provide an accuracy of the slip velocity model for the EOF within 2% [20]:  $d/\lambda_D > 10^3$ ;  $\text{Re}_d$  (the Reynolds number based on  $d$ )  $< 10$ ;  $\Delta x > 4\lambda_D$ .

The aforementioned approach was realized for numerical simulations of EOF in porous media. In particular, below we present the results of simulations concerned with EOF in random packings of spherical particles confined by a cylindrical container.

Computer simulation of EOF through confined random packings

Three random packings of uniform spheres of dimensionless diameter  $d_p = 1$  with the same average porosity  $\varepsilon = 0.40$  and identical geometrical dimensions,  $d_c = 10d_p$  and height  $H = 5d_p$ , were generated by the algorithm described above (see Section 4.4.1) using three different configurations of the start points. The periodic boundary condition along the axial direction was imposed. In Figure 4.40 the top views (i.e. the views directed along the container axis) of all packings are shown.

The structures of the packings were analysed by the corresponding radial porosity distribution functions (Fig. 4.41). It should be pointed out that Packing 3 possesses a more ordered structure near the wall than the others two, but this fact can be explained exclusively with the random nature of the generating algorithm. The generated packings were discretised by a three-dimensional uniform grid with a resolution of  $\beta = d_p/\Delta x = 40$ . Then, it was supposed that the interparticle space is filled with the electrolyte solution. In order to satisfy the thin double layer assumption, the aspect ratio  $d_p/\lambda_D$  was chosen to be 1000, with  $\lambda_D = 10$  nm ( $c = 1$  mM),  $d_p = 10$   $\mu$ m and  $d_c = 100$   $\mu$ m. Further, for each spatial matrix the Laplace

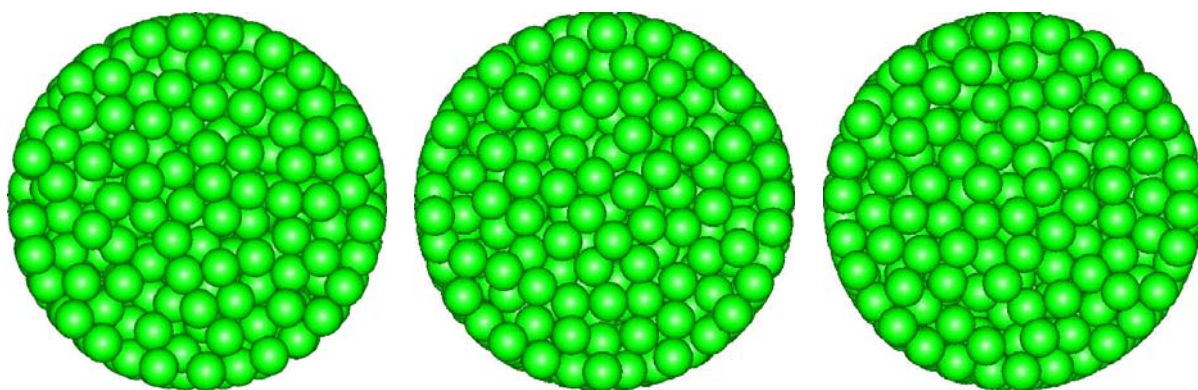


**Figure 4.40.** Top views of the generated cylindrical random packings (from left to right: Packing 1, Packing 2, and Packing 3). The interparticle porosity of packings is 0.40, height  $H = 5d_p$  and diameter  $d_c = 10d_p$ , where  $d_p$  is the diameter of particles consisting the packings.

equation was solved subject to the following boundary conditions: a perfectly insulating solid-liquid interface (including the container wall) and the periodic condition along the axial direction

$$[[\Phi]] = E_{\text{ext}} H ,$$

where  $[[\Phi]]$  denotes the potential difference between two opposite points lying at the “top” and “bottom” boundaries. The calculated distribution of the electrical potential was used to determine the local electric field and slip velocity at the solid-liquid interface by Eq. 4.36. Finally, the slip velocity distribution was incorporated into the solution for the Navier-Stokes equation as boundary condition. The complete simulation of the EOF was repeated for each packing for four values of the electric field,  $E_{\text{ext}} = 10, 25, 50,$  and  $100$  kV/m, which was applied along the axial direction. The  $\zeta$ -potential is assumed to be uniformly distributed at the particles surface. The dielectric constant, viscosity and temperature of the liquid phase, were  $80, 8.9 \times 10^{-7}$  m<sup>2</sup>/s and  $297$  K, respectively.

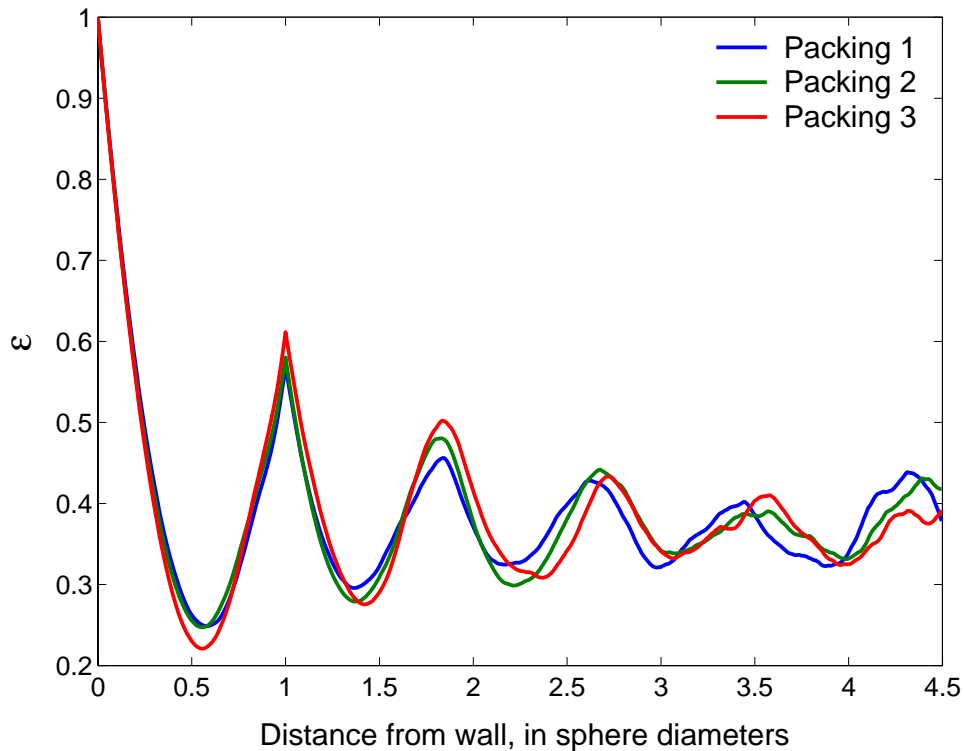


**Figure 4.41.** Radial porosity distribution functions for the three random packings of spheres presented in Figure 4.37.



In Figure 4.42 the dependence of the average axial EOF velocity  $\langle v_{eo} \rangle$  on the applied electric field is shown for all packings and  $\zeta = 50$  mV. All three structures demonstrate a similar, linear dependence of the mean EOF velocity on the electric field strength. This agrees with Overbeek's model (Eq. 4.89) that implies the following proportionality coefficient relating the mean EOF velocity and electric field

$$\mu_{eo} = \frac{\langle v_{eo} \rangle}{E_{ext}} = -\frac{\varepsilon_0 \varepsilon_r \zeta}{\eta} \left( \frac{\sigma^*}{\sigma^\infty} \right), \quad (4.90)$$

The conductivity ratio ( $\sigma^*/\sigma^\infty$ ) for packed chromatographic columns it is approximately 0.3 [164], whence Eq. 4.90 results in  $\mu_{eo} = 1.195 \times 10^{-5} \text{ m}^2/\text{Vs}$ . The simulated EOF data give  $\mu_{eo} = 1.333 \times 10^{-5}$ ,  $1.289 \times 10^{-5}$ , and  $1.135 \times 10^{-5} \text{ m}^2/\text{Vs}$  for Packing 1, 2, and 3, respectively, demonstrating good agreement with the theoretical approach. The difference in  $\mu_{eo}$  obtained for different packings can be explained by their statistical nature. It should be pointed out that

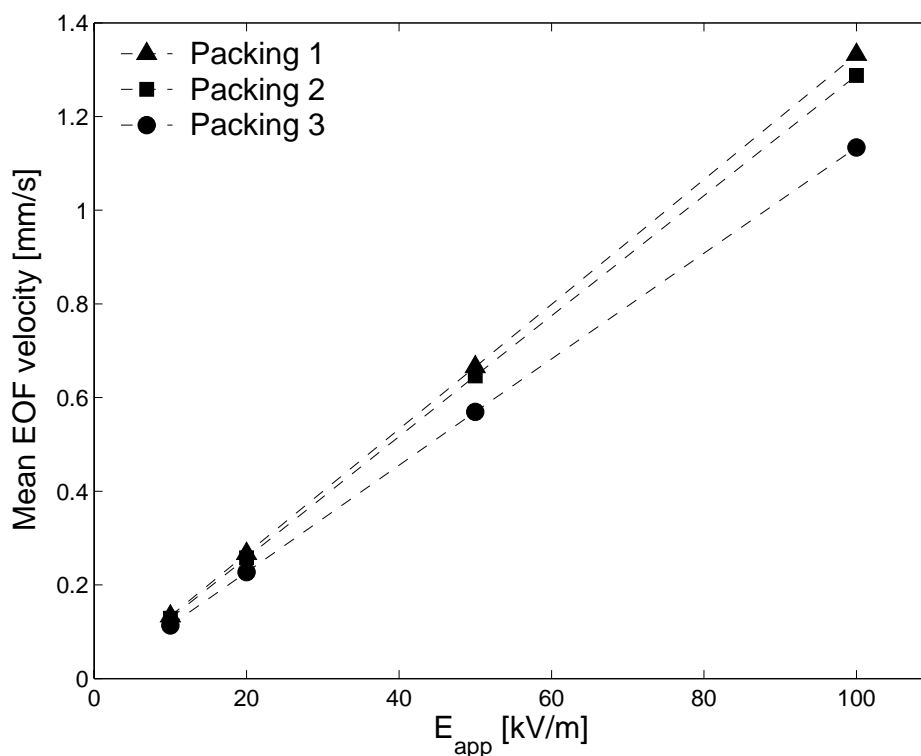
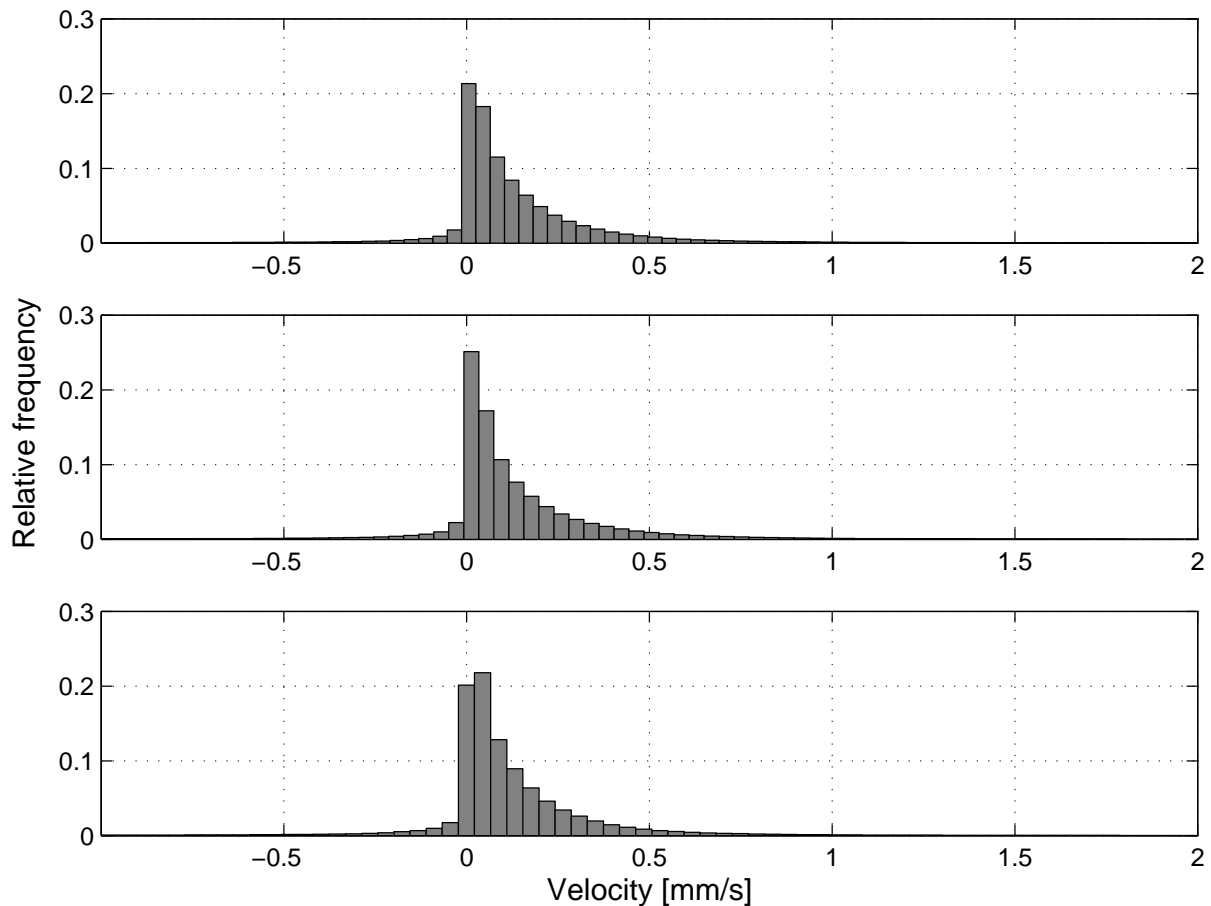


**Figure 4.42.** The average axial EOF velocity for Packings 1, 2, and 3 as a function of the applied electric field.  $\zeta = 50$  mV,  $\varepsilon_r = 80$ ,  $\eta = 8.9 \times 10^{-7} \text{ m}^2/\text{s}$  and  $T = 297$  K.

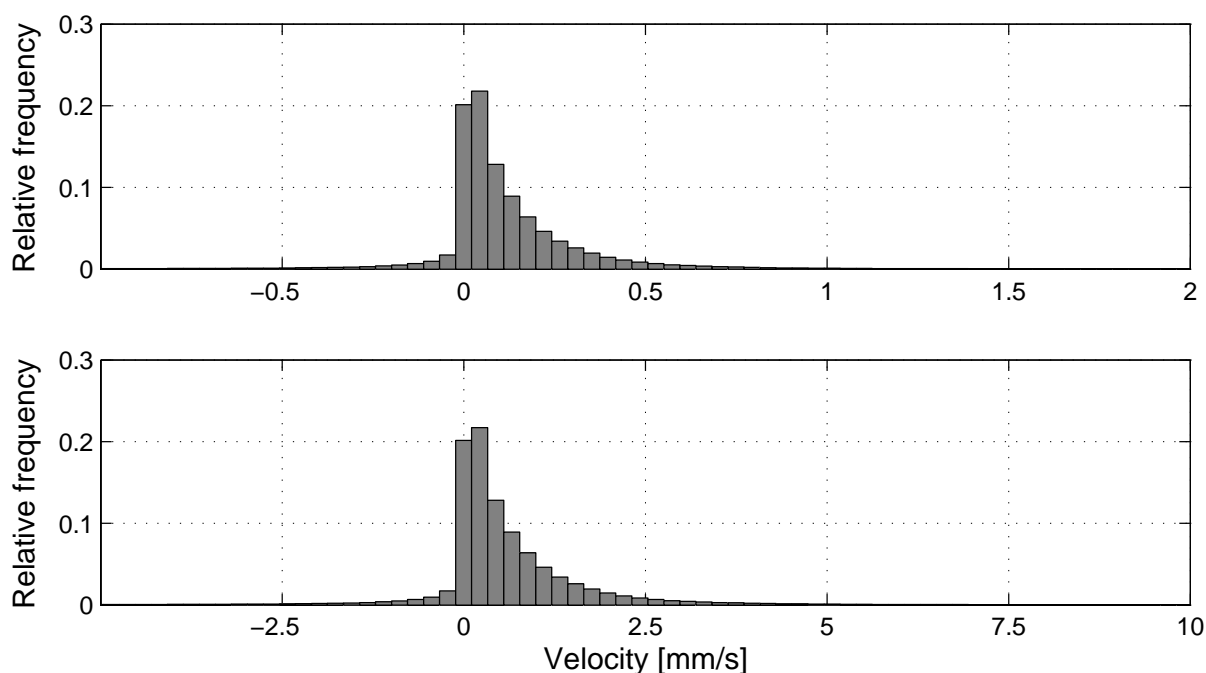
Packing 3 which is characterized as the most ordered structure (see Fig. 4.41) provides the smallest mean velocity.

Figure 4.43 shows histograms for the axial velocity distributions in the three packings. Though all of the structures generate similar velocity distributions (unimodal, with sharp left edges in direction toward negative values and gradual damping toward positive values), Packing 3 can be again distinguished by its specificity in the velocity distribution near zero. While for both Packing 1 and 2 the most probable value of the velocity is very close to zero, the mode of the velocity distribution for Packing 3 is shifted toward higher velocity. It should be noted that in all three packings the negative velocities represent a noticeable fraction in the general distributions.

A linear dependence of the *mean* velocity on the applied electric field is also preserved for all values of the *local* velocity. Figure 4.44 demonstrates that the shape of the velocity distribution histogram does not vary with changes in the electric field strength from 10 to 50 kV/m which results only in a corresponding rescaling of the velocity axis (in this case, by factor of 5).



**Figure 4.43.** Axial velocity distribution histograms for Packing 1 (top), Packing 2 (middle), and Packing 3 (bottom).



**Figure 4.44.** Velocity distribution histograms for Packing 3 with an electric field,  $E_{\text{ext}}$  of 10 (top) and 50 (bottom) kV/m.

It should be noted that all of the aforementioned differences in the velocity fields corresponding to the different packings (especially with respect to Packing 3) have a stochastic character related to the random nature of the packings. The possible increase of the axial dimension of the random packings will reduce variations in their mean characteristics due to more satisfactory averaging. In contrast, the local inhomogeneity is an inherent property of random packings which does not disappear with an increasing size of the porous medium. As it has been mentioned above, the presented numerical approach gives the possibility to obtain complete information concerning the velocity distribution. This capability is illustrated by Figure 4.45 which shows a colour map of the velocity profile for a slice located in the middle (with respect to the height) of Packing 1. It is interesting to note the small dark region in the upper-left quarter of the map that corresponds to negative velocity in the interfacial void formed by three particles. This fact indicates that, in contrast to the electric field, the velocity field in a porous medium can show a non-zero vorticity. The vorticity can originate in the morphological complexity of porous media. It is evident that, although the overall velocity distribution is nonuniform, regions near the wall are characterized, in general, by higher velocity (light-yellow colours) than the bulk region (dark-red colours). This fact is directly related to the local porosity distribution, which indicates a locally more permeable structure of random packings in proximity to the confining wall

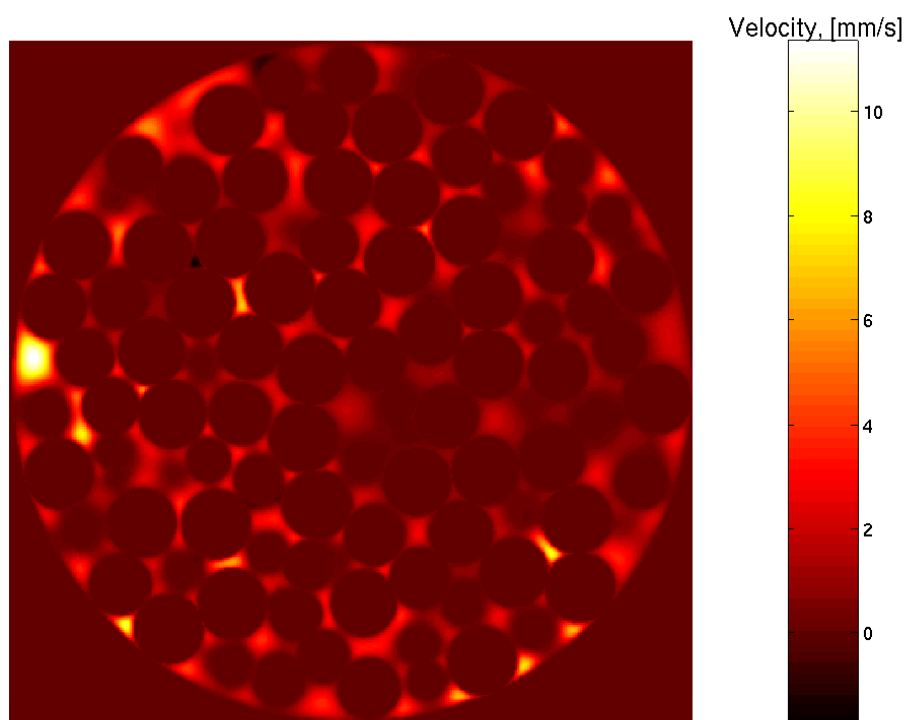


**Figure 4.45.** Colour map of the axial velocity profile for the half-height slice of Packing 1.  
 $E_{\text{ext}} = 100 \text{ kV/m}$ .

(Fig. 4.41). The increased permeability of this region results in a local decrease of its hydrodynamic resistance and an increase of the axial component of the local electric field. Both effects lead to a local velocity augmentation.

Our simulation results obtained with the presented approach confirm the general opinion that in confined random packings an additional source of fluid dispersion can arise due to fluctuations in packing density and permeability caused, in particular, by the structural inhomogeneity of regions close to the wall. This phenomenon can significantly reduce the separation efficiency achievable with packed chromatographic columns due to the engendered additional dispersion. One of the possible ways to attenuate this undesirable effect is the use of packed columns of particles with nonuniform size distributions, when smaller particles better fill the voids between larger ones, thereby reducing the amplitudes of local density fluctuations across whole column cross-sectional area.

## **References**

1. H.A. Stone and S. Kim, *AIChE J.* **47**, 1250 (2001).
2. K.F. Jensen, *Chem. Eng. Sci.* **56**, 293 (2001).
3. N. Giordano and J.T. Cheng, *J. Phys. Condens. Matter* **13**, R271 (2001).
4. G. M. Whitesides and A.D. Stroock, *Phys. Today* **54**, 42 (2001).
5. T. Chovan and A. Guttman, *Trends Biotechnol.* **20**, 116 (2002).
6. V. Hessel and H. Löwe, *Chem. Ing. Tech.* **74**, 185 (2002).
7. D.R. Reyes, D. Iossifidis, P.A. Auroux, and A. Manz, *Anal. Chem.* **74**, 2623 (2002).
8. R.F. Probstein. *Physicochemical Hydrodynamics*; John Wiley & Sons, New York, 1994.
9. R.J. Hunter. *Foundations of Colloid Science*; Oxford University Press, Oxford, 2001.
10. C.L. Rice and R. Whitehead, *J. Phys. Chem.* **69**, 4017 (1965).
11. P.H. Paul, M.G. Garguilo, and D.J. Rakestraw, *Anal. Chem.* **70**, 2459 (1998).
12. U. Tallarek, E. Rapp, T. Scheenen, E. Bayer, and H.V. As, *Anal. Chem.* **72**, 2292 (2000).
13. C. Yang, D. Li, and J.H. Masliyah, *Int. J. Heat Mass Transfer* **41**, 4229 (1998).
14. N. A. Patankar, H.H. Hu, *Anal. Chem.* **70**, 1870 (1998).
15. S.V. Ermakov, S.C. Jacobson, and J.M. Ramsey, *Anal. Chem.* **70**, 4494 (1998).
16. S. K. Griffiths, R.H. Nilson, *Anal. Chem.* **71**, 5522 (1999).
17. F. Bianchi, R. Ferrigno, and H.H. Girault, *Anal. Chem.* **72**, 1987 (2000).
18. E.B. Cummings, S.K. Griffiths, R.H. Nilson, and P.H. Paul, *Anal. Chem.* **72**, 2526 (2000).
19. S. Arulanandam and D. Li, *Colloids Surf. A* **161**, 89 (2000).
20. J.G. Santiago, *Anal. Chem.* **73**, 2353 (2001).
21. P. Dutta and A. Beskok, *Anal. Chem.* **73**, 5097 (2001).
22. R.J. Yang, L.M. Fu, and Y.C. Lin, *J. Colloid Interface Sci.* **239**, 98 (2001).
23. H.J. Keh and H.C. Tseng, *J. Colloid Interface Sci.* **242**, 450 (2001).
24. P. Dutta, A. Beskok, and T.C. Warburton, *J. Microelectromech. Syst.* **11**, 36 (2002).
25. L.M. Fu, R.J. Yang, and G.B. Lee, *Electrophoresis* **23**, 602 (2002).
26. Y.J. Kang, C. Yang, and X.Y. Huang, *J. Colloid Interface Sci.* **253**, 285 (2002).
27. D. Erickson and D. Li, *Langmuir* **18**, 1883 (2002).
28. A.T. Conlisk, J. McFerran, Z. Zheng, and D. Hansford, *Anal. Chem.* **74**, 2139 (2002).
29. U. Frisch, D. d'Humieres, B. Hasslacher, P. Lallemand, Y. Pomeau, and J.P. Rivet, *Complex Syst.* **1**, 649 (1987).
30. G. McNamara and G. Zanetti G, *Phys. Rev. Lett.* **61**, 2332 (1988).
31. F.J. Higuera and J. Jiménez, *Europhys. Lett.* **9**, 663 (1989).
32. S. Succi, R. Benzi, and F. Higuera, *Physica D* **47**, 219 (1991).
33. R. Benzi, S. Succi, and M. Vergassola, *Phys. Rep.* **222**, 145 (1992).
34. S. Chen and G.D. Doolen, *Annu. Rev. Fluid Mech.* **30**, 329 (1998).
35. M.A.A. Spaid and F.R. Phelan Jr, *Phys. Fluids* **9**, 2468 (1997).
36. R.S. Maier, D.M. Kroll Y.E. Kutsovsky, H.T. Davis, and R.S. Bernard, *Phys. Fluids* **10**, 60 (1998).
37. B. Manz, L.F. Gladden, and P.B. Warren, *AIChE J.* **45**, 1845 (1999).
38. R.S. Maier, D.M. Kroll, H.T. Davis, and R.S. Bernard, *J. Colloid Interface Sci.* **217**, 341 (1999).

39. J. Bernsdorf, G. Brenner, and F. Durst, *Comput. Phys. Commun.* **129**, 247 (2000).
40. D.S. Clague, B.D. Kandhai, R. Zhang, P.M.A. Slood, *Phys. Rev. E* **61**, 616 (2000).
41. R.J. Hill, D.L. Koch, and A.J.C. Ladd, *J. Fluid Mech.* **448**, 243 (2001).
42. S. Békri, O. Vizika, J.F. Thovert, and P.M. Adler, *Int. J. Multiphase Flow* **27**, 477 (2001).
43. G. Drazer and J. Koplik, *Phys. Rev. E* **63**, art. no. 056104 (2001).
44. R.S. Maier, D.M. Kroll, R.S. Bernard, S.E. Howington, J.F. Peters, and H.T. Davis, *Philos. Trans. Roy. Soc. Lond. A* **360**, 497 (2002).
45. M. Yoshino and T. Inamuro, *Int. J. Numer. Meth. Fluids.* **43**, 183 (2003).
46. D. Kandhai, D. Hlushkou, A.G. Hoekstra, P.M.A. Slood, H. Van As, and U. Tallarek, *Phys. Rev. Lett.* **88**, art. no. 234501 (2002).
47. M.R. Schure, R.S. Maier, D.M. Kroll, and H.T. Davis, *Anal. Chem.* **74**, 6006 (2002).
48. Q.H. Kang, D.X. Zhang, and S.Y. Chen, *Phys. Rev. E* **66**, art. no. 056307 (2002).
49. T. Zeiser, M. Steven, H. Freund, P. Lammers, G. Brenner, F. Durst, and J. Bernsdorf, *Philos. Trans. Roy. Soc. Lond. A* **360**, 507 (2002).
50. S. Békri, S. J. Howard, J. Muller, and P.M. Adler, *Transp. Porous Media* **51**, 41 (2003).
51. P. Bhatnagar, E. Gross, and M. Krook, *Phys. Rev.* **94**, 511 (1954).
52. S. Chen, H. Chen, D. Martinez, and W.H. Matthaeus, *Phys. Rev. Lett.* **67**, 3776 (1991).
53. Y.H. Qian, D. d'Humieres, and P. Lallemand, *Europhys. Lett.* **17**, 479 (1992).
54. B. Li and D.Y. Kwok, *Langmuir* **19**, 3041 (2003).
55. L. Ren, W. Qu, and D. Li, *Int. J. Heat Mass Transfer* **44**, 3125 (2001).
56. X. Nie, G.D. Doolen, and S. Chen, *J. Stat. Phys.* **107**, 279 (2002).
57. P.B. Warren, *Int. J. Mod. Phys. C* **8**, 889 (1997).
58. R.J. Gross and J.F. Osterle, *J. Chem. Phys.* **49**, 228 (1968).
59. A.S. Rathore, *Electrophoresis* **23**, 3827 (2002).
60. U. Tallarek, E. Rapp, A. Seidel-Morgenstern, and H.V. As, *J. Phys. Chem. B* **106**, 12709 (2002).
61. L. Ren and D. Li, *J. Colloid Interface Sci.* **243**, 255 (2001).
62. D. Coelho, M. Shapiro, J.F. Thovert, and P.M. Adler, *J. Colloid Interface Sci.* **181**, 169 (1996).
63. D. Kandhai, A. Koponen, A.G. Hoekstra, M. Kataja, J. Timonen, and P.M.A. Slood, *J. Comput. Phys.* **150**, 482 (1999).
64. Z. Guo, C. Zheng, and B. Shi, *Phys. Rev. E* **65**, art. no. 046308 (2002).
65. P.C. Hiemenz and R. Rajagopalan. *Principles of Colloid and Surface Chemistry*; Marcel Dekker, New York, 1997.
66. A.V. Delgado and F.J. Arroyo. Electrokinetic Phenomena and Their Experimental Determination, an Overview. In *Interfacial Electrokinetics and Electrophoresis*; A.V. Delgado (ed.), Marcel Dekker, New York, 2002.
67. J.L. Anderson and W.K. Idol, *Chem. Eng. Commun.* **38**, 93 (1985).
68. B. Potoček, B. Gaš, E. Kenndler, and M. Štědrý, *J. Chromatogr. A* **709**, 51 (1995).
69. P. Weidenhammer and H.J. Jacobasch, *J. Colloid Interface Sci.* **180**, 232 (1996).
70. R.A. Hayes, *Colloids Surf. A* **146**, 89 (1999).
71. A.E. Herr, J.L. Molho, J.G. Santiago, M.G. Mungal, T.W. Kenny, and M.G. Garguilo, *Anal. Chem.* **72**, 1053 (2000).
72. S. Ghosal, *J. Fluid Mech.* **459**, 103 (2002).
73. M. Pačes, J. Kosek, M. Marek, U. Tallarek, and A. Seidel-Morgenstern, *Electrophoresis* **24**, 380 (2003).

74. D. Long, H.A. Stone, and A. Ajdari, *J. Colloid Interface Sci.* **212**, 338 (1999).
75. F.E. Regnier and D. Wu. Chemical Derivatization of Fused Silica Capillaries. In *Capillary Electrophoresis Technology*; N.A. Guzman (ed.), Marcel Dekker, New York, 1993.
76. A.D. Stroock, M. Weck, D.T. Chiu, W.T.S. Huck, P.J.A. Kenis, R.F. Ismagilov, and G.M. Whitesides, *Phys. Rev. Lett.* **84**, 3314 (2000).
77. A. Ajdari, *Phys. Rev. E* **53**, 4996 (1996).
78. J.P. Gleeson, *J. Colloid Interface Sci.* **249**, 217 (2002).
79. F. Bianchi, F. Wagner, P. Hoffmann, and H.H. Girault, *Anal. Chem.* **73**, 829 (2001).
80. C.L. Rice and R. Whitehead, *J. Phys. Chem.* **69**, 4017 (1965).
81. C. Yang, C.B. Ng, and V. Chan, *J. Colloid Interface Sci.* **248**, 524 (2002).
82. J.-P. Hsu, C.-Y. Kao, S. Tseng, and C.J. Chen, *J. Colloid Interface Sci.* **248**, 176 (2002).
83. D. Li, *Colloids Surf. A* **195**, 35 (2001).
84. H.K. Tsao, *J. Colloid Interface Sci.* **225**, 247 (2000).
85. J.M. MacInnes, *Chem. Eng. Sci.* **57**, 4539 (2002).
86. L.-M. Fu, J.-Y. Lin, and R.-J. Yang, *J. Colloid Interface Sci.* **258**, 266 (2003).
87. P. J. Scales, F. Grieser, Th.W. Healy, L.R. White, and D.Y.C. Chan, *Langmuir* **8**, 965 (1992).
88. N. Churaev, V. Sobolev, A. Somov, *J. Colloid Interface Sci.* **97**, 574 (1984).
89. R. Pit, H. Hervet, and L. Leger, *Phys. Rev. Lett.* **85**, 980 (2000).
90. T. Hiemstra, J.C.M. de Wit, W.H. Van Riemsdijk, *J. Colloid Interface Sci.* **133**, 105 (1989).
91. L.T. Zhuravlev, *Colloids Surf. A* **173**, 1 (2000).
92. J. Sonnefeld, M. Löbbus, and W. Vogelsberger, *Colloids Surf. A* **195**, 215 (2001).
93. C.L.A. Berli, M.V. Piaggio, and J.A. Deiber, *Electrophoresis* **24**, 1587 (2003).
94. S. Weber and P. Carr. The Theory of the Dynamics of Liquid Chromatography. In *High Performance Liquid Chromatography*; P.R. Brown and R. A. Hartwick (eds.), New York, NY, 1989.
95. A.L. Loeb, J.Th.G. Overbeek, and P.H. Wiersema. *The Electrical Double Layer Around a Spherical Colloid Particle*, Massachusetts, MIT Press, 1961.
96. C.H. Bennett, *J. Appl. Phys.* **43**, 2727 (1972).
97. A.J. Matheson, *J. Phys. C* **7**, 2569 (1974).
98. R. Jullien, A. Pavlovitch, and P. Meakin, *J. Phys. A* **25**, 4103 (1992).
99. P.L. Spedding and R.M. Spencer, *Comput. Chem. Eng.* **22**, 247 (1995).
100. N. Martys, S. Torquato, and D. Bentz, *Phys. Rev. E* **50**, 403 (1994).
101. M. Allen and D. Tildesley. *Computer Simulation of Liquids*, Clarendon Press, Oxford, 1992.
102. L. Lebon, L. Oger, J. Leblond, J.P. Hulin, N.S. Martys, and L.M. Schwartz, *Phys. Fluids* **8**, 293 (1996).
103. B.D. Lubachevsky and F.H. Stillinger, *J. Stat. Phys.* **60**, 561 (1990).
104. W.S. Jodrey and E.M. Tory, *Phys. Rev. A* **32**, 2347 (1985).
105. J.H. Knox, G.R. Laird, and P.A. Raven. *J. Chromatogr.* **122**, 129 (1976).
106. M. Oda and T. Sudoo. In *Powders and Grains*. J. Biarez and R. Gourves (eds.); Balkema, Rotterdam, 1989.
107. S.F. Edwards and D.V. Grinev, *Phys. Rev. Lett.* **82**, 5397 (1999).
108. S.F. Edwards and D.V. Grinev, *Chem. Eng. Sci.* **56**, 5451 (2001).
109. J.L. Finney. Local Structure of Disordered Hard Sphere Packings. In *Disorder and Granular Media*, D. Bideau and A. Hansen (eds.); Elsevier, Amsterdam, 1993.
110. N. Rivier. Order and Disorder in Packings and Froths. In *Disorder and Granular Media*, D. Bideau and A. Hansen (eds.); Elsevier, Amsterdam, 1993.

111. J. Lemaitre, A. Gervois, J. Troadec, et al., *Philos. Mag. B*, **67**, 347 (1993).
112. L. Oger, A. Gervois, and J. Troadec, *Philos. Mag. B*, **74**, 177 (1996).
113. S. Torquato, *Phys. Rev. Lett.* **74**, 2156 (1995).
114. J. Quintanilla and S. Torquato, *Phys. Rev. E* **55**, 1558 (1997).
115. E. Tsotsas. *Über die Wärme- und Stoffübertragung in durchströmten Festbetten*, VDI - Fortschrittsberichte Reihe **3/223**, VDI-Verlag, Düsseldorf, 1990, p.19.
116. K. Schnitzlein, *Chem. Eng. Sci.* **56**, 579 (2001).
117. O. Bey and G. Eigenberger, *Chem. Eng. Sci.* **52**, 1365 (1997).
118. J. Bear. *Dynamics of Fluids in Porous Media*; New York, Dover Publications, 1988.
119. F.A.L. Dullien. *Porous Media: Fluid Transport and Pore Structure*, New York, Academic Press, 1992.
120. M. Sahimi. *Flow and Transport in Porous Media and Fractured Rock*; Weinheim, VCH, 1995.
121. D.H. Rothman and S. Zaleski. *Lattice-Gas Cellular Automata*; Cambridge University Press, 1997.
122. B. Chopard and M. Droz. *Cellular Automata Modelling of Physical System*; Cambridge University Press, 1998.
123. R.S. Maier, D.M. Kroll, R.S. Bernard, S.E. Howington, J.F. Peters and H.T. Davis, *Phys. Fluids* **12**, 2065 (2000).
124. A. Koponen, D. Kandhai, E. Hellén, M. Alava, A. Hoekstra, M. Kataja, K. Niskanen, P.M.A. Slood and J. Timonen, *Phys. Rev. Lett.* **80**, 716 (1998).
125. B. Ferréol and D.H. Rothman, *Transp. Porous Media* **20**, 3 (1995).
126. D.J. Gunn and C. Price, *Trans. Inst. Chem. Eng.* **47**, T341 (1969).
127. N.-W. Han, J. Bhakta and R.G. Carbonell, *AIChE J.* **31**, 277 (1985).
128. D.L. Koch and J.F. Brady, *J. Fluid Mech.* **154**, 399 (1985).
129. D.L. Koch and J.F. Brady, *Chem. Eng. Sci.* **42**, 1377 (1987).
130. D.J. Gunn, *Chem. Eng. Sci.* **42**, 363 (1987).
131. C.P. Lowe and D. Frenkel, *Phys. Rev. Lett.* **77**, 4552 (1996).
132. J. Salles, J.-F. Thovert, R. Delannay, L. Prevors, J.-L. Auriault, and P.M. Adler, *Phys. Fluids A* **5**, 2348 (1993).
133. S. Stapf, K.J. Packer, R.G. Graham, J.-F. Thovert, and P.M. Adler, *Phys. Rev. E* **58**, 6206 (1998).
134. U. Tallarek, E. Bayer, D. van Dusschoten, T. Scheenen, H. Van As, G. Guiochon, and U.D. Neue, *AIChE J.* **44**, 1962 (1998).
135. U. Tallarek, F.V. Vergeldt, and H. Van As, *J. Phys. Chem. B* **103**, 7654 (1999).
136. J.P. Hulin, *Adv. Colloid Interface Sci.* **49**, 47 (1994).
137. U.D. Neue. *HPLC Columns: Theory, Technology, and Practice*; Wiley-VCH, New York, 1997.
138. B.J. Stanley, C.R. Foster, and G. Guiochon, *J. Chromatogr. A* **761**, 41 (1997).
139. B.J. Stanley, M. Sarker, and G. Guiochon, *J. Chromatogr. A* **741**, 175 (1996).
140. E.O. Stejskal and J.E. Tanner, *J. Chem. Phys.* **42**, 288 (1965).
141. E.O. Stejskal, *J. Chem. Phys.* **43**, 3597 (1965).
142. J. Kärgner and W. Heink, *J. Magn. Reson.* **51**, 1 (1983).
143. P.T. Callaghan. *Principles of Nuclear Magnetic Resonance Microscopy*; Oxford University Press, 1993.
144. P.T. Callaghan, A. Coy, D. MacGowan, K.J. Packer, and F.O. Zelaya, *Nature* **351**, 467 (1991).
145. R. M. Cotts. Diffusion and diffraction, *Nature* **351**, 443 (1991).
146. U. Tallarek, D. van Dusschoten, H. Van As, E. Bayer, and G. Guiochon, *J. Phys. Chem. B* **102**, 3486 (1998).



147. J. Kärger, H. Pfeifer and W. Heink, *Adv. Magn. Reson.* **12**, 1 (1988).
148. M. Giese, K. Rottschäfer, and D. Vortmeyer, *AIChE J.* **44**, 484 (1998).
149. T.C. Hsiang and H.W. Haynes Jr., *Chem. Eng. Sci.* **32**, 678 (1977).
150. H. Martin, *Chem. Eng. Sci.* **33**, 913 (1978).
151. R.G. Carbonell, *Chem. Eng. Sci.* **35**, 1347 (1980).
152. B.-J. Ahn, A. Zoulalian, and J.M. Smith, *AIChE J.* **32**, 170 (1986).
153. J. Tobochnik and E.M. Chapin, *J. Chem. Phys.* **88**, 5824 (1988).
154. S. Torquato, T.M. Truskett, and P.G. Debenedetti, *Phys. Rev. Lett.* **84**, 2064 (2000).
155. W.M. Visscher and M. Bolsterli, *Nature* **239**, 504 (1972).
156. N.E. Gusak. *The Physics of Structurally Disordered Matter*; Adam Hilger, Bristol, 1987.
157. D. Kandhai, A. Koponen, A. Hoekstra, M. Kataja, J. Timonen and P.M.A. Sloot, *Comp. Phys. Commun.* **111**, 14 (1998).
158. J.J. Meyers and A.I. Liapis, *J. Chromatogr. A* **852**, 3 (1999).
159. R. Stol, H. Poppe, and W.Th. Kok, *J. Chromatogr. A* **887**, 199 (2000).
160. P.T. Vallano and V.T. Remcho, *Anal. Chem.* **72**, 4255 (2000).
161. R.C. Wu and K.D. Papadopoulos, *Colloids Surf. A* **161**, 469 (2000).
162. A. S. Rathore, Cs. Horváth, *J. Chromatogr. A* **781**, 185 (1997).
163. J.T.G. Overbeek. In *Colloid Science*; H.R. Kruyt (ed.), Elsevier, New York, 1952, p. 152.
164. G. Choudhary, C. Horváth, *J. Chromatogr. A* **781**, 161 (1997).
165. R.F. Benenati and C.B. Brosilow, *AIChE J.* **8**, 359 (1962).
166. M. Giese, *Untersuchung der Strömung in porösen Medien unter Berücksichtigung effektiver Viskositäten*, Dissertation, TU München, 1997.
167. V.P. Andreev, S.G. Dubrovsky, and Y.V. Stepanov, *J. Microcolumn Sep.* **9**, 443 (1997).
168. A.S. Rathore, E. Wen, and C. Horváth, *Anal. Chem.* **71**, 2633 (1999).



## Chapter 5

# Summary and conclusion

In this work, the great potential of numerical simulations for the study of mass transport in electrochromatographic systems has been demonstrated. The problem of the electroosmotic flow and associated transport is a very complicated one from the mathematical point of view. Its complexity originates, first of all, in the interdependence of various phenomena of different nature which define jointly temporal and spatial variations in electrokinetic systems. In addition, actual chromatographic columns possess a very intricate morphology, that is engendered by the porous structure of the adsorbent materials, such as a packing of (porous) particles or monolithic porous media. These circumstances frequently mean that the problem of mass transport in an electrokinetic system cannot, in principle, be solved analytically and numerical solution is the only way to obtain information on the system without direct experimental measurements.

The numerical approach presented in this Ph.D. thesis combines the coupled numerical treatment of the Poisson and Nernst-Planck problems by traditional finite-difference techniques, as well as the Navier-Stokes problem by the relatively novel lattice-Boltzmann equation (LBE) method. The latter presents an alternative, yet promising method in the computational fluid dynamics (CFD). It has emerged with the promise to become a superior modelling approach, both computationally and conceptually as compared to the existing arsenal of continuum-based CFD methods. The lattice-Boltzmann equation method has been used successfully to simulate various problems including multiphase and turbulent flow, colloidal suspensions, magnetohydrodynamics, etc. Among the principal advantages of this method are the possibility to easily treat geometrically complex boundaries and its inherent parallelism, which allows to implement the codes at modern (high-performance) parallel computers.

In this thesis the development and use of the LBE method for microfluidic electrohydrodynamics is presented. The electromotive forces originating in interactions of the external electric field with ions in a liquid are incorporated in the hydrodynamic problem and determine the flow velocity field. Since the charge distribution in a liquid depends, in turn, on

the fluid flow, the problem was solved through a numerical iterative procedure which, in general, includes the solution for the Poisson, Nernst-Planck, and Navier-Stokes equations. The developed approach has been applied to the original simulation of various electrokinetic problems taking place in actual electrochromatographic and microfluidic systems. In this thesis the results of the following problem simulations are presented and discussed:

- EOF in a straight open capillary with nonuniform distribution of the  $\zeta$ -potential;
- EOF in slit microchannels with nonuniform surface charge density which depends on the local chemical environment;
- EOF through a simple cubic array of spherical particles;
- Hydrodynamic dispersion in random-close packings of porous particles;
- EOF through confined random packings of spherical nonporous particles.

In each case, the primary simulated data for a simplified or approximated problem were, first and foremost, compared to the published one and good agreement has been found. Then, the presented approach has been applied to the simulation of more complex problems. The obtained results help to get a detailed insight into hydrodynamic processes taking place during the electrochromatographic separation, as well as to control existing processes and to improve the design of electrochromatographic systems.

One question may occur to the reader: “Why did not you simulate EOF and dispersion in a confined random packing of particles with the nonuniform  $\zeta$ -potential or surface charge density that both depend on the local chemical environment? It is the most general case.” Yes, it is true. However, there is no ideal computational method and each approach has advantages and limitations for a certain class of problems. Actual electrokinetic systems are characterized by different time and length scales of relevant phenomena. The distribution of the electrical charge and potential within the EDL occurs over a distance of the order of 10 nm from the solid surface, while the typical axial displacement due to fluid flow requiring to reach the asymptotic dispersion is of the order of 1 mm. These large differences in length scales involving the simulation makes unrealistic the implementation of a numerical model even with modern high-performance computers. Therefore, in each particular case and problem the following dilemma was considered: whether to choose a fine computational resolution and obtain good accuracy at the small length scale associated with the EDL thickness, or to carry out the simulation with a coarser computational grid, with larger inaccuracy, but to be able to cover a larger region of the investigated system.

The development of the presented approach in a direction toward the combination of high computational accuracy and the ability to perform large-scale simulations is one of the keys to improve the approach. Another development direction is the incorporation of the solution for the Nernst-Planck equation into the LBE algorithm to reduce the computational time expenses. Finally, the presented numerical model can be improved for the transition to nanoscale microfluidic simulations, when the continuum approach is not valid any longer. Such length scale seems to become typical for a number of porous media employed in modern electrochromatographic systems using fixed particulate or monolithic beds, as well as open-channel structures or chip devices.

In summary, the application of numerical methods to investigate the hydrodynamic aspects and transport phenomena in (electro)chromatographic systems was proved very successful. The electroosmotic flow and associated mass transport in various microfluidic systems were studied and a number of relevant results were obtained. The work in immediate future will be focused on several topics that were not treated in this thesis. In particular, the analysis of the velocity distribution will be carried out for EOF through confined random packings with various particle size distributions and the effects on resulting hydrodynamic dispersion be evaluated.



# Resume

The main goal of this Ph.D. thesis was the development of an advanced numerical approach to simulate mass transport in microfluidic electrokinetic systems. Understanding of the electrokinetic aspects of mass transport in microfluidic systems has a great importance for a relatively new technique in separation science: capillary and microchip electrochromatography. This technique combines the advantages of high-performance liquid chromatography and capillary electrophoresis. Capillary electrochromatography uses the electroosmotic flow generated by a high, external voltage applied to drive the liquid phase through a porous medium. The general mathematical formulation of the problem of the electroosmotic flow includes the description of various phenomena of different nature: hydrodynamics, electrostatics, ion transport, adsorption and dissociation. In addition, actual microfluidic systems employed in electrochromatography demonstrate frequently the extremely intricate morphology associated with their porous structure impeding the numerical treatment.

In this work, the electroosmotic flow is modelled by the iterative numerical solution of the coupled Poisson, Nernst-Planck, and Navier-Stokes equations. In order to realize a computational time required for large-scale simulations of mass transport in actual electrochromatographic systems, the developed numerical model was implemented at a parallel high-performance computer and then used to simulate various electrokinetic problems.

Chapter 2 contains a brief general theoretical description of mass transport problems in polar liquids, which are typical for applications in electrochromatographic analysis. The behaviour of such liquids can drastically change when an external electric field is applied due to the presence of the electrical double layer at the solid-liquid interface.

Chapter 3 describes mainly the lattice-Boltzmann formalism, an alternative approach in computational fluid dynamics, which allows easily to treat geometrically complex boundaries and which is inherently parallel. In this approach the fluid is modelled by particles moving on a regular lattice. At each time step the particles propagate to neighbouring lattice points and re-distribute their velocities in a local collision phase. This method is extended to electrohydrodynamic problems by incorporating in the model the Lorentz force arising from the interaction of electrical charges in the liquid with the applied electric field.

In Chapter 4 the results of a number of simulations concerning various aspects of microfluidic electrokinetics are presented and discussed. They follow the description of the algorithm employed for the computer generation of confined random packings of spherical particles. That algorithm is based on an improved Jodrey-Tory procedure and allows to generate fixed beds of spheres with an arbitrary size distribution confined by an arbitrary container, as well as with periodic boundaries. The random sphere packings are further used as a model of particulate packed chromatographic columns.

The presented numerical approach allows to obtain complete information concerning the spatial distribution in a modelled system of the flow velocity, electrical potential and species concentrations. In particular, the developed approach permits to evaluate the error related to the application of the apparent slip velocity boundary conditions to quantify differences between velocity fields obtained under different approximations concerning electrical boundary conditions, to study the effect of local variations in the chemical environment (caused by convection) on the surface charge density and final flow velocity field, to investigate the relation between the electroosmotic flow velocity and parameters of an electrokinetic system, such as the  $\zeta$ -potential, solution concentration and applied electric field. In addition, the presented approach can be used to investigate the transient behaviour of simulated systems, such as the transient hydrodynamic dispersion in packed beds.



# Zusammenfassung

Das Hauptanliegen der Dissertation bestand in der Entwicklung und Implementierung eines sehr leistungsfähigen Ansatzes zur numerischen Simulation der Fluidodynamik und des Massentransports in komplexen porösen Materialien wie partikulären Festbetten oder (Chip-) Kanalstrukturen, mit besonderem Augenmerk auf der Elektrokinetik in mikrofluidischen Systemen. Lokal und makroskopisch wirkende elektrische Felder sind für eine ganze Reihe von heutzutage wichtigen Transportprozessen in porösen Materialien (etwa beim Ionenaustausch, der Elektrophorese, Sedimentation, Filtration/Pressung, Rheologie konzentrierter Suspensionen oder Elektroosmose) von sehr großer, wenn nicht gar essentieller Bedeutung. Sei es, daß interne elektrische Potentialverläufe in Festbetten aus porösen Partikeln die Permselectivität und Retention von geladenen Analyten beeinflussen (z.B. in der Nanofiltration genutzt), oder aber extern angelegte elektrische Felder gezielt eingesetzt werden, um effizienten Transport von flüssiger Phase und Analyten durch sehr feine Poren (z.B. in den Mikrofluidik-Strukturen oder wenig permeablen konsolidierten natürlichen Materialien) zu bewirken: Das unter Umständen nicht-lineare, dynamische Wechselspiel aus Adsorption geladener Analyten an geladenen Grenzflächen im internen und ggfs. überlagerten, externen elektrischen Potentialgradienten mit lokal resultierendem und veränderlichem Transport gestaltet sich äußerst komplex und ist noch nicht ausreichend verstanden, um auf der Basis momentanen Wissens die entkoppelte Optimierung der einzelnen Parameter (wie Diffusion, Konvektion, Adsorption oder Elektrokinetik) systematisch zu betreiben. Insbesondere ist eine Entflechtung der Transportphänomene und selektive Untersuchung von einzelnen Beiträgen bei kostspieligen präparativen Verfahren im downstream-processing oder bei auf Effizienz angewiesenen Analysen von Geringstmengen in der Bioanalytik erforderlich.

Das Verständnis elektrostatischer und elektrokinetischer Aspekte des Stofftransports in mikrofluidischen Strukturen und Festbetten hat besonders große Bedeutung für eine relativ junge analytische Trenntechnik, die Kapillarelektrochromatographie (KEC). Sie vereinigt die Vorteile der Hochleistungsflüssigkeitschromatographie und Kapillarelektrophorese. Anfang der 90'er Jahre sind zahlreiche Publikationen zur KEC erschienen, die diesem Hybrid zwischen Kapillarelektrophorese und mikro-HPLC außerordentliche und, verglichen mit der klassischen HPLC, stark verbesserte Trennleistungen bescheinigten. In der KEC wird der

Eluent (eine Pufferlösung) durch das Anlegen hoher elektrischer Felder (bis 100 kV/m) durch Kapillarsäulen (Innendurchmesser: 75-250  $\mu\text{m}$ ) bewegt, die mit kleinen, porösen Teilchen (Durchmesser 3-10  $\mu\text{m}$ ) gepackt sind. Ein für Trennungen attraktives Merkmal des erzeugten elektroosmotischen Flusses (EOF) ist die Tatsache, daß die Geschwindigkeiten im Zwischenkornvolumen, in Anlehnung an die Charakteristik des EOFs in ungepackten zylindrischen Kapillaren, weitgehend konstant sind (plug-flow-Verhalten, kaum Eddy-Diffusion). Es bietet sich an, diesen Vorteil in Verbindung mit der Retentionsvielfalt der für die HPLC entwickelten und bereits ausgiebig charakterisierten stationären Phasen zu nutzen. Die allgemeine mathematische Formulierung des Transports durch den EOF schließt die Beschreibung von Phänomenen unterschiedlicher Natur ein wie Hydrodynamik, Elektrostatik, Ionen-transport, Adsorption und Stofftrennung, etc. Außerdem kommt für eine realitätsnahe Beschreibung der Elektrokinetik in porösen Materialien die oft äußerst komplexe Morphologie dieser Systeme als erschwerender Faktor hinzu.

In dieser Arbeit wird der elektroosmotische Fluss in einfachen Kanalstrukturen und Festbetten aus sphärischen Partikeln durch die numerische Lösung der gekoppelten Poisson-, Nernst-Planck- und Navier-Stokes-Gleichungen modelliert. Um zu vertretbaren Rechenzeiten für die großangelegte Simulation des Massentransports in realen elektrochromatographischen Systemen zu gelangen, wurde das entwickelte numerische Modell an einem parallelen Hochleistungsrechner implementiert und dann verwendet, um gezielt ausgewählte elektrokinetische Probleme von großer Reichweite zu bearbeiten.

Kapitel 2 enthält eine kurze, allgemein gehaltene theoretische Beschreibung des Massentransports in polaren Flüssigkeiten, die für die weitere Betrachtung von elektrochromatographischen Systemen notwendig ist. Das hydrodynamische Verhalten derartiger Flüssigkeit kann sich wesentlich ändern, wenn ein externes elektrisches Feld auf die lösungsseitige Region der elektrischen Doppelschicht an der fest-flüssig Phasengrenze einwirkt und dadurch dann elektrokinetischen Fluß in dem System induziert. Die Hydrodynamik hängt stark ab von den physiko-chemischen Eigenschaften der Oberfläche und Elektrolytlösung.

Kapitel 3 beschreibt hauptsächlich den lattice-Boltzmann Formalismus, der eine vielversprechende Alternative (basierend auf einem von Natur aus parallelen Algorithmus) für die Modellierung von rechenintensiver Hydrodynamik, insbesondere in sehr komplexen Geometrien, darstellt. Beim lattice-Boltzmann Verfahren wird die Flüssigkeit durch diskrete Partikel modelliert, die sich (im mesoskopischen Sinne) auf einem regelmäßigen Gitter befinden. Sie bewegen sich schrittweise auf benachbarte Gitterpunkte zu und verteilen Impuls

und ihre Geschwindigkeiten in einer lokalen Kollisionsphase neu, um damit auf makroskopischer Ebene den Navier-Stokes-Gleichungen zu gehorchen. Die Methode wird durch Berücksichtigung der Lorentzkraft, welche die Wechselwirkung von elektrischer Raumladung in der Flüssigkeit mit dem externen elektrischen Feld beschreibt, auf elektrohydrodynamische Probleme erweitert.

Im Kapitel 4 werden die Ergebnisse mehrerer Simulationen bezüglich verschiedener Aspekte einer mikrofluidischen Elektrokinetik präsentiert und analysiert. Für die betrachteten Festbetten basieren die Ergebnisse auf einem Algorithmus, der es erlaubt, statistisch dichte Packungen von kugelförmigen Partikeln zu erzeugen. Er beruht auf dem verbesserten Jodrey-Tory Algorithmus und erlaubt, diese Packungen in beliebig geformten Behältern für beliebige Säulen/Partikel-Durchmesserhältnisse zu generieren. Die zufälligen Packungen von kugelförmigen Partikeln werden als Modell für reale Festbetten z.B. in chromatographischen Säulen betrachtet. In diesen Geometrien werden dann transiente und stationäre Dispersion simuliert und analysiert, wobei die Porosität der Kugeln selbst im Vordergrund steht, sowie der Unterschied zwischen hydraulischem und elektroosmotischem Fluß.

Der entwickelte numerische Ansatz erlaubt es, quantitative Information bezüglich der räumlichen Verteilung des elektrischen Potentials, Fließgeschwindigkeit und Konzentrationen der Elektrolyten zu erhalten. Insbesondere ermöglicht das präsentierte Modell, den mit der Annahme von Slip-Geschwindigkeiten verbundenen Fehler und Unterschiede in den Geschwindigkeitsfeldern zu quantifizieren, die auf verschiedenen Annahmen elektrischer Randbedingungen beruhen, sowie die Wirkung lokaler Variation in physiko-chemischen Eigenschaften der Oberfläche (z.B. durch Konvektion verursacht) auf die Oberflächenladungsdichte und das resultierende Geschwindigkeitsfeld (inklusive dispersiver Effekte) zu analysieren, oder aber die Beziehung zwischen (lokalem und volumetrischem) EOF und elektrokinetischen Systemparametern wie zeta-Potential, Elektrolytkonzentration und dem angelegten elektrischen Feld systematisch zu herauszuarbeiten. Außerdem ist der in dieser Arbeit vorgestellte numerische Ansatz sehr geeignet für die Untersuchung des transienten Verhaltens (z.B. einzelner Dispersionsbeiträge) in mikrofluidischen Kanal- und Festbettstrukturen, gerade im Zusammenhang mit einer elektrischen Doppelschicht unter nicht-Gleichgewichtsbedingungen.



# LEBENS LAUF

von

Dzmitry Hlushkou, geboren am 14. Dezember 1969  
in Minsk, Weißrussland

## Schulbildung

Sept. 1977 – Mai 1985      Grund- und Sekundar-Schule in Minsk, Weißrussland

## Studium

Sept. 1985 – Juni 1989      Studiengang Radiotechnik an der Ingenieurschule in Minsk

Sept. 1992 – Juni 1997      Studiengang Radio-Physik (Diplom) an der Weißrussischen  
Staatsuniversität in Minsk

## Wehrdienst

Okt. 1989 – Okt.1991      Wehrdienst (Grenzschutz in Turkmenistan, UdSSR)

## Dissertation

Nov.1997      Beginn der Doktorarbeit unter Leitung von Prof. Vladimir  
Apanasovich (Department of Systems Analysis, Belarusian State  
University, Minsk, Weißrussland) mit dem Thema:  
*Computer Simulation of Diffusion in Biosystems*

Feb. – März 1999 und      Visiting Scientist bei Dr. Henk Van As am Departament of  
März – Aug. 2000      Molecular Physics und Wageningen NMR Centre, Wageningen  
Agricultural University, Wageningen (Niederlande)

ab Mai 2001      Forschungsprojekt “Kapillarelektrochromatographie” unterstützt  
von der Max-Planck-Gesellschaft mit dem Ziel der Erstellung  
einer Dissertation.